ANALYSIS OF THE DYNAMICS OF THE LINEAR-AND-ROTARY-MOTION ENERGY-CONVERSION SYSTEMS WITH ACTIVE DC EXCITATION

A Dissertation
Presented to
The Academic Faculty

by

LIJUN HE

In Partial Fulfillment
Of the Requirements for the Degree
Doctor of Philosophy in the
School of Electrical and Computer Engineering

Georgia Institute of Technology
December 2015

ANALYSIS OF THE DYNAMICS OF THE LINEAR-AND-ROTARY-MOTION ENERGY-CONVERSION SYSTEMS WITH ACTIVE DC EXCITATION

Approved by:

Dr. Ronald G. Harley, Advisor
School of ECE
Georgia Institute of Technology

Dr. Thomas G. Habeter, Co-Advisor
School of ECE
Georgia Institute of Technology

Dr. J. Rhett Mayor
School of ME
Georgia Institute of Technology

Dr. Maryam Saeedifard
School of ECE
Georgia Institute of Technology

Dr. David G. Taylor
School of ECE
Georgia Institute of Technology

Dr. Lei Zhu
School of ME
Georgia Institute of Technology

Date Approved: [November 9, 2015]

To

my father, Futang He, and

my mother, Fanyi Ji,

for their love and support.

献给我亲爱的父亲母亲

ACKNOWLEDGEMENTS

First and foremost, I would like to express my most sincere thanks to Prof. Ronald. G. Harley. Prof. Harley has been a wise advisor to me. I am much honored to be one of his graduate students. His profound knowledge in electric-magnetic analysis, serious attitudes towards research, and great personality help me gain a deeper understanding of engineering, make significant progress in my research, and improve my problem-solving skills as a professional researcher. Without his inspiration, encouragement, and guidance, I would not have completed much of my research work. I always greatly and deeply appreciate his support.

I would also like to give my special thanks to my co-advisor, Prof. Thomas G. Habetler. His great personality and trust in my abilities allow me to explore the research ideas freely. In addition, I am grateful for the valuable suggestions and guidance from Prof. J. Rhett Mayor; I benefited a lot from his interdisciplinary perspective in structural and vibrational aspects of various energy-conversion devices.

I would like to thank Professor Jose A. Restrepo from Universidad Simón Bolívar and Dr. Siwei Cheng. I benefited a lot from the detailed technical discussions with them in motor condition monitoring and control of power electronics. Also, I'm indebted to them for their help and assistance to my experimental work. The hands-on experience I obtained through this process is invaluable.

I would also like to thank Prof. Maryam Saeedifard, Prof. David Taylor, and Dr. Lei Zhu for serving as my PhD thesis committee members and their insightful questions and suggestions.

I was very fortunate to have worked with so many exceptional and talented fellow students at Georgia Tech. Among them, I wish to especially thank Yi Du, Dr. Liang Du, Howard Liles, Guangcong Zhang and Yi Deng for the helpful discussions and pleasant collaborations in my research work.

I would also like to thank Dr. Andrew Paquette, Bai Cui, Dr. Bin Lu, Chen Jiang, Dawei He, Dr. Diogenes Molina, Dr. Dongbo Zhao, Dr. Dustin Howard, Hao Chen, Dr. Jiaqi Liang, Dr. Jie Dang, Dr. Jing Dai, John Seuss, Liangyi Sun, Morteza Rezaee, Nan Liu, Dr. Pinjia Zhang, Qin Sun, Raeey Regassa, Dr. Renke Huang, Rui Fan, Shen Zhang, Dr. Stefan Grubic, Sufei Li, Dr. Tongge Zhu, Wenlu Fu, Yang Hui, Dr. Yao Duan, Dr. Ye Tao, Dr. Yi Yang, Yi Wang, Yu Liu, Yun Zhang, Yuqian Dong, Dr. Zhaoyu Wang, Zhenkai Wu, and Zhenyu Tan for their friendship and support during my four years at Georgia Tech. There are numerous names of faculty, family, and friends that I should mention here. I want to express my gratitude to all of the people I know.

Most of all, I owe the greatest debt of gratitude to my family. My parents have always been the source of love, understanding, encouragement, and support throughout my entire life. I wish them good health and happy living.

The financial supports from the following institutions/organizations are gratefully acknowledged:

(1) National Electric Energy Testing Research and Applications Center (NEETRAC)

(2) National Science Foundation (NSF)

TABLE OF CONTENTS

Page

LIST OF TABLES

Page

LIST OF FIGURES

Page

SUMMARY

The objective of the dissertation is to develop simplified analytical models for typical linear-motion and rotary-motion energy-conversion systems under active DC excitation without tedious numerical-simulation effort, and provide practical implementation of the models in optimal-design and thermal-protection aspects.

The model of a vacuum automatic circuit recloser (a typical linear-motion system under DC excitation) is first developed in the form of a non-linear discontinuous eighth-order dynamic system. The model is then used to simulate the transient mechanical and electromagnetic performance during the opening and closing movements of the recloser. Such a model is not found in the literature.

Although the model is based on certain simplifying assumptions, the result is validated by high-speed-camera measurements. In addition, the impact of key design variables is explored, based on which an improved recloser design is proposed, and helps to optimize capital and production costs without degrading performance.

Further analytical investigation is carried out in modeling an inverter-fed induction motor (IM) (a typical rotary-motion system) with active DC injection. The IM is closed-loop controlled via two popular motor-control algorithms, namely, the direct-torque-control (DTC) algorithm and field-oriented-control (FOC) algorithm. Quantitative relationships between the changes of various machine variables during the active DC excitation are provided in the theoretical analysis. The developed DC-injection model is further simplified for practical implementation.

The developed IM model under DC injection results in practical ways to excite a proper amount of DC current directly or indirectly into IM stator windings via different

closed-loop motor-control algorithms. In a DTC motor-drive system, the modeling work makes it possible to excite the DC current indirectly inside the motor by superimposing a stator-flux-linkage-bias command in the flux-control loop or a torque-ripple command in the torque-control loop. The proposed flux-linkage-injection and torque-injection methods are the first novel efforts to implement the DC-signal-injection method in a DTC motor-drive system. In addition, the analysis carried out in a standard FOC drive system brings about an improved DC-current-injection approach: the torque ripple in this method is significantly mitigated compared to all existing DC-injection methods in FOC systems.

The proposed DC-injection methods, either in a DTC or an FOC system, lead to a simple, low-cost, accurate, and non-invasive thermal-monitoring scheme for closed-loop-controlled IMs, where the stator temperature is indirectly estimated from stator resistance.

Furthermore, considering inverter non-idealities, there is a challenge for a typical inverter drive to accurately estimate the DC component of motor terminal voltages. The existing methods are extended to provide a complete study of the real-time signal-processing technique for both DTC and FOC algorithms, and are finally implemented in a custom-built programmable motor-drive system. The experimental results demonstrate that the proposed technique gives accurate and robust stator-temperature estimation, regardless of the operating conditions and cooling modes.

The analytical modeling method for the linear-motion and rotary-motion energy-conversion systems can be further extended to other power devices with similar mechanisms, and implemented in optimal design, control, and thermal-protection areas.

CHAPTER 1 INTRODUCTION AND OBJECTIVE OF THE RESEARCH

1.1 BACKGROUND

Advanced computing resources have brought researchers' attention to the implementation of numerical-simulation techniques in the electromagnetic, thermal, and structural analysis of typical power-energy devices, such as electric machines, transformers, transmission lines, power switches, and protection relays. One of the most popular numerical-simulation methods is the finite-element-analysis (FEA) method.

However, from the industry point of view, commercial FEA software is usually too expensive. The numerical simulation is complicated and time-consuming, which requires a lot of computational effort, especially when the device model is integrated in a large-scale power system. In addition, the numerical-simulation result will be a lot more convincing, if it is validated by a theoretical analysis or a hardware test. Considering the expense of setting up a test rig and the limit access to the measurement data, it is, therefore, preferable and more practical to provide an analytical explanation at the first stage, with acceptable tolerance and simplification.

The objective of this PhD dissertation is to develop simplified analytical models for typical linear-motion and rotary-motion energy-conversion systems under active DC excitation without tedious numerical-simulation effort, and provide practical implementation of the models in optimal-design and thermal-protection aspects.

In particular, the selected linear-motion device with DC excitation is a vacuum automatic circuit recloser, directly energized from DC capacitors. The selected rotary-

motion system with DC excitation is a closed-loop-controlled induction motor (IM) under active DC-signal injection.

1.2 A VACUUM AUTOMATIC CIRCUIT RECLOSER WITH ACTIVE DC EXCITATION

According to IEEE standard C37.104-2012 [1], an automatic circuit recloser is defined as a self-controlled device for automatically interrupting and reclosing an alternating-current (AC) circuit, with a predetermined sequence of opening and reclosing followed by resetting, hold-closed, or lock-out operation.

Because of the automatic-reclosing feature, reclosers are widely implemented in distribution power systems, since more than 80 % of faults in distribution networks are temporary [1, 2]. The recloser ensures that the protection scheme is applied properly to yield the greatest possible reduction in the number and extent of power outages, and minimize the impact on residential and industrial customers [3, 4].

For widely-used microprocessor-controlled reclosers, design engineers can specify all settings digitally according to IEEE standards, without the knowledge of the complicated physical mechanism of an actual device. On the other hand, computer-aided recloser technology has led to a reduction in published literature on the physical modeling and analysis of these devices.

However, if a recloser-modeling tool is developed, the opening-and-closing dynamic response can be calculated before any performance tests. Sensitivity analyses and trade-off studies will be used to evaluate the impact of individual variables on the final performance. The further study and analysis can result in an improved design including optimizing capital and production costs without degrading performance.

This detailed dynamic model can also be integrated with other power-system simulation tools to examine and limit any deleterious interaction effects of recloser operation on the rest of the power system. The modeling work will assist the coordination of the recloser with other protection devices.

1.3 A CLOSED-LOOP-CONTROLLED INDUCTION MOTOR UNDER ACTIVE DC INJECTION

Closed-loop-controlled induction motors (a typical rotatory-motion energy conversion system) are often connected to important types of loads and used in high-performance motion control and traction system, such as cranes and hoists, elevators, hybrid and electric vehicles, modern railway system, and diesel-electric ships.

Among the various type of closed-loop controlled system, the field-oriented-control (FOC) scheme [5-8] and direct-torque-control (DTC) scheme [9-13] are most popular and widely commercialized in industry.

Although DC-signal injection techniques have been widely implemented in grid-connected IMs and open-loop-controlled IMs since 1980s, a limited amount of research has been carried out on closed-loop control systems. So far, the DC-injection method has only been applied to field-oriented-controlled (FOC) IMs.

Therefore, it is much desired to extend the DC-injection method from FOC to direct-torque-control (DTC) scheme, which provides direct, accurate and fast-dynamic control especially for the motor's electromagnetic torque and flux linkages [14], and is able to compete with the well-known field-oriented control (FOC).

In addition, conventionally, the implementation of this DC-injection method causes some amount of low-frequency torque ripple, which is undesired especially for high-

performance motor applications. For an FOC system, further improvement is needed to reduce the fundamental-frequency ripple caused by the DC-signal injection.

The various DC-signal-injection methods on IMs are often used to estimate motor stator-winding resistance. This contributes to an enhanced thermal-monitoring and protection scheme, and is also beneficial for improving motor-control performances. DC-injection-based estimation is independent of all other motor parameters and inherent motor asymmetry, and is a most reliable approach for obtaining an accurate estimate of stator resistance and winding temperature under various operating conditions and cooling modes [15].

1.4 PROBLEM STATEMENT

The objective of this dissertation is to develop simplified analytical models for typical linear-motion and rotary-motion energy-conversion systems under active DC excitation without tedious numerical-simulation effort, and provide practical implementation of the models in optimal-design and thermal-protection aspects.

The selected linear-motion device with DC excitation is a vacuum automatic circuit recloser, directly energized from DC capacitors. The selected rotary-motion system with DC excitation is a closed-loop-controlled induction motor (IM) under active DC-signal injection.

The developed modeling work for the linear-motion recloser system will help to describe the transient mechanical and electromagnetic performance during the opening and closing movements of the recloser system. Such a model is not found in the literature. Although the parameterized model is based on certain simplifying assumptions, the result

will be validated by high-speed-camera measurements, and can further be used to optimize capital and production costs without degrading performance.

The modeling work carried out for the rotary-motion closed-loop controlled IM system will result in practical ways to excite a proper amount of DC current directly or indirectly into IM stator windings via DTC and FOC closed-loop motor-control algorithms. In a DTC motor-drive system, the modeling work will make it possible to excite the DC current indirectly inside the motor by superimposing a stator-flux-linkage-bias command in the flux-control loop or a torque-ripple command in the torque-control loop. The proposed flux-linkage-injection and torque-injection methods are the first novel efforts to implement the DC-signal-injection method in a DTC motor-drive system. In addition, the analysis carried out for a standard FOC drive system will bring about an improved DC-current-injection approach: the torque ripple in this method is significantly reduced compared to all existing DC-injection methods in FOC systems.

The proposed DC-injection methods, either in a DTC or an FOC system, will lead to a simple, low-cost, accurate, and non-invasive thermal-monitoring scheme for closed-loop-controlled IMs.

Furthermore, considering inverter non-idealities, there is a challenge for a typical inverter drive to accurately estimate the DC component of motor terminal voltages. The existing methods will be extended to provide a complete study of the real-time signal-processing technique for both DTC and FOC algorithms, and are finally implemented in a custom-built programmable motor-drive system.

1.5 DISSERTATION OUTLINE

Chapter 2 reviews the definition, basic operating principles, and implementation of a typical recloser device in distributed power system.

Chapter 3 presents the-state-of-the-art of the active DC-signal-injection method applied to grid-connected IMs, open-loop-controlled IMs, and closed-loop-controlled IMs in detail. In addition, various thermal monitoring techniques are summarized in this chapter. Among all the existing technique, the DC-model-based estimation is independent of all other motor parameters and inherent motor asymmetry, and is proved to be a most reliable approach for obtaining an accurate estimate of stator resistance under various operating conditions and cooling modes.

Chapter 4 and Chapter 5 introduce the detailed analysis of the typical linear-motion energy-conversion system with active DC excitation: a vacuum automatic-recloser system energized from a DC capacitor. Although the model is based on certain simplifying assumptions, the modeling effort is validated by high-speed camera test, and this parameterized model can be implemented to provide an improved design approach, where the system production cost is reduced without degrading the performance.

In Chapter 6 and Chapter 7 , further analytical investigations are carried out in modeling a DTC or FOC induction motor (IM) (a typical rotary-motion system) with active DC injection. Quantitative relationships between the changes of various machine variables during the active DC excitation are provided in the theoretical analysis. The developed DC-injection model is further simplified, which results in practical ways to excite a proper amount of DC current directly or indirectly into IM stator windings via DTC and FOC algorithms.

Chapter 8 describes the application of the proposed DC-injection methods on closed-loop-controlled motor systems in thermal monitoring and protection aspects. The proposed DC-injection methods lead to a simple, low-cost, accurate, and non-invasive thermal-monitoring scheme for closed-loop-controlled IMs. In addition, the real-time signal-processing techniques considering inverter non-idealities are discussed. Finally, the monitoring results are validated by hardware tests under various operating conditions and cooling modes.

Chapter 9 summarizes the main contributions and lists outcomes of this dissertation.

CHAPTER 2 LITERATURE REVIEW OF AUTOMATIC CIRCUIT RECLOSERS

2.1 INTRODUCTION

This chapter presents a literature review about the modeling and implementation effort for an automatic circuit recloser system.

Section 2.2 explains the definition and basic operation of a recloser device. Due to the automatic-reclosing feature, the device is widely implemented in distribution power systems, since more than 80 % of faults in distribution networks are temporary, and it contributes to minimizing the impact on residential and industrial customers.

Section 2.3 reviews the previous work on the physical modeling effort for recloser devices, and indicates the importance to develop a recloser-modeling tool for design applications and large-scale power system simulations.

Section 2.4 summarizes the chapter.

2.2 DEFINITION AND IMPLEMENTATION

According to IEEE standard C37.104-2012 [1], an automatic circuit recloser is defined as a self-controlled device for automatically interrupting and reclosing an alternating-current (AC) circuit, with a predetermined sequence of opening and reclosing followed by resetting, hold-closed, or lock-out operation. The figure below presents some widely-used recloser devices in industry, either singled-phase devices or three-phase devices.

(a) Cooper VXE Recloser

(b) TripSaver® II Cutout-Mounted Recloser

(c) Viper-S@Solid Dielectric Recloser

(d) Southern California Edison Recloser

Figure 2.1 Typical commercialized recloser devices.

Basically, a recloser opens when an overcurrent fault is detected, and automatically recloses after a set period of time to re-energize the power line after an interruption. This process is repeated for a limited number of times if the fault persists, and eventually falls into the open state (lock-out) for a permanent fault [1]. Hence, it introduces an

economical means of repetitively interrupting faulted distribution circuits to clear transient faults and isolate permanent faults.

Because of the automatic-reclosing feature, reclosers are widely implemented in distribution power systems, since more than 80 % of faults in distribution networks are temporary [1, 2]. The recloser ensures that the protection scheme is applied properly to yield the greatest possible reduction in the number and extent of power outages, and minimize the impact on residential and industrial customers [3, 4].

2.3 PREVIOUS WORK

For widely-used microprocessor-controlled reclosers [16], design engineers can specify all settings digitally according to IEEE standards, without the knowledge of the complicated physical mechanism of an actual device. The number of reclosing events, the reclosing-interval delays, instantaneous curves, and time-delay curves are specified to coordinate with fuses, sectionalizers, and other automatic reclosers [2, 17-21].

The figure [17] below presents an example for recloser settings, where there are two ‘fast operation’ and two ‘time-delay operation’ reclosing events before it reaches the lockout condition. The detected fault-current level will affect the recloser operating time according to the specification in the instantaneous and time-delay trip curves.

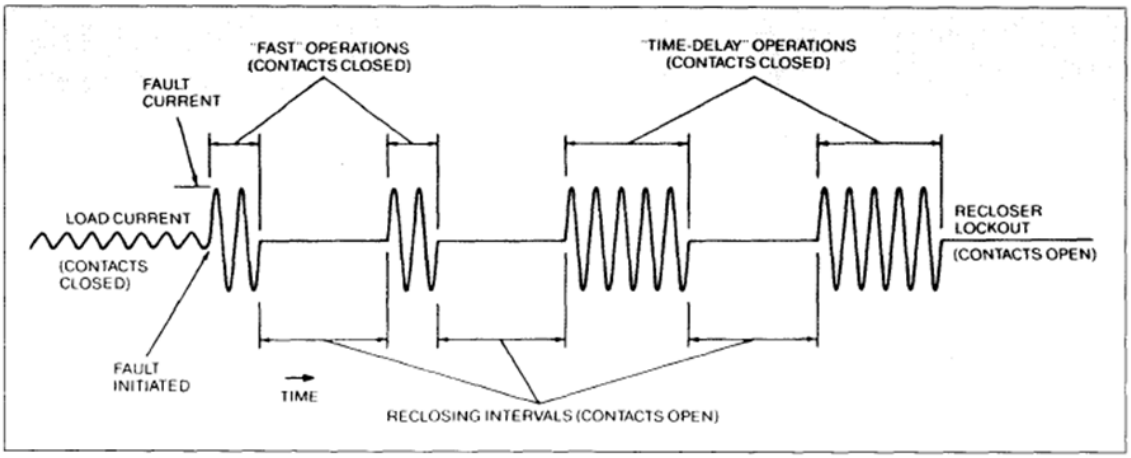

Figure 2.2 A typical reclosing setting [17].

In [18, 22], the authors focus on the different protection-coordination schemes for radial-distribution feeders. A typical redial distribution system is shown in Figure 2.3.

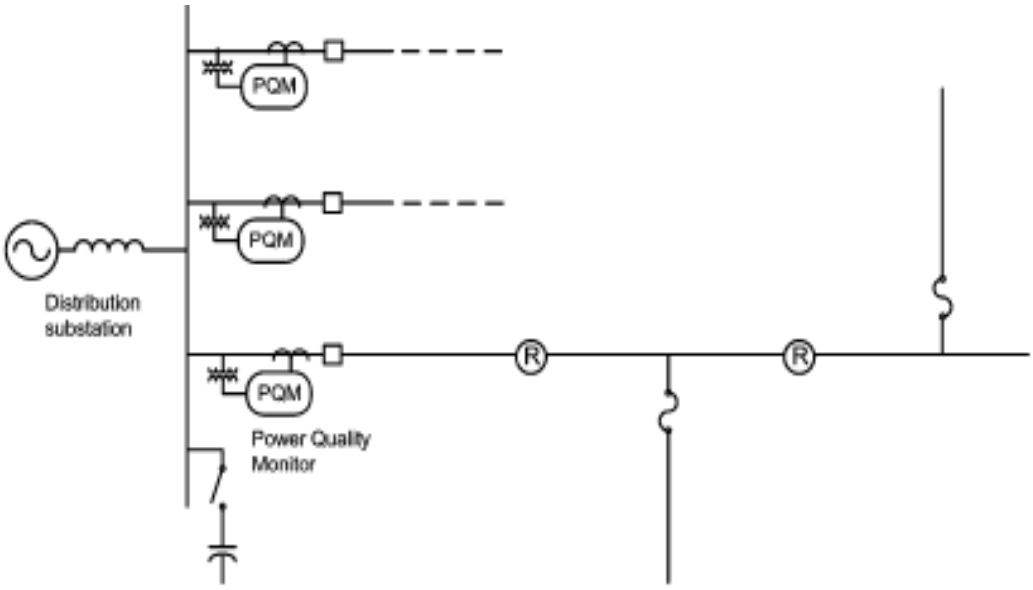

Figure 2.3 A typical radial distribution system [18].

If a distributed generator (DG), like a wind generator for example, is added, the distribution system becomes non-radial. Therefore, the settings and coordination have to be modified [23], and the allocation of DGs and protection devices has to be optimized [23, 24].

On the other hand, computer-aided recloser technology has led to a reduction in published literature on the physical modeling and analysis of these devices. Even those publications that describe some design considerations for different types of recloser, like oil reclosers[3, 25-29], vacuum reclosers [30], and SF6 reclosers [31], only show a general diagram of the operating mechanism; the recloser performance is then evaluated by tests under different scenarios.

However, if a recloser-modeling tool is developed, the opening-and-closing dynamic response can be calculated before any performance tests. The impact of design variables, such as the ratings and dimensions of different components, can be explored. Sensitivity analyses and trade-off studies will be used to evaluate the impact of individual variables on the final performance. The further study and analysis can result in an improved design including optimizing capital and production costs without degrading performance.

This detailed dynamic model can also be integrated with other power-system simulation tools to examine and limit any deleterious interaction effects of recloser operation on the rest of the power system. The modeling work can assist the coordination of the recloser with other protection devices.

2.4 CHAPTER SUMMARY

This chapter presents the definition, basic operating principles, and implementation of a typical recloser device in distributed power system. It is also pointed out that the

computer-aided recloser technology has led to a reduction in published literature on the physical modeling and analysis of these devices.

If a detailed parameterized reloser analytical model can be developed, it helps to understand the dynamic response of the recloser device during the opening and closing processes, and also contribute to the improved recloser designs, large-scale power system simulation, as well as the protection-device coordination. Therefore, Chapter 4 and Chapter 5 are focusing on the analysis and modeling results of a typical vacuum automatic-recloser system energized from a DC capacitor, as well as the applications of the developed recloser simulation tool.

CHAPTER 3 LITERATURE REVIEW OF INDUCTION MOTORS WITH ACTIVE DC INJECTION

3.1 INTRODUCTION

DC-signal-injection methods can be used to estimate motor stator-winding resistance. An accurate knowledge of stator resistance contributes to an enhanced thermal-monitoring and protection scheme, and is also beneficial for improving motor-control performances.

Although an accurate estimate is only guaranteed at steady state, the DC-model-based estimation is independent of all other motor parameters and inherent motor asymmetry, and is a most reliable approach for obtaining an accurate estimate of stator resistance under various operating conditions and cooling modes [15]. This injection method is especially applied to motors under normal-speed operating conditions, where the stator and winding reluctance is much more significant compared to the winding resistance:$X_s \gg R_s$.

Sections 3.2 –3.4 review and discuss the-state-of-the-art of the active DC-signal-injection method applied to IMs. This technique has been implemented in grid-connected IMs, open-loop-controlled IMs, and closed-loop-controlled IMs with various motor-control strategies.

Section 3.5 focuses on the applications of the DC-injection method for thermal-monitoring implementation purposes, where the stator DC resistance is obtained from the injected voltages and currents and used as a direct indicator for the average stator winding temperature. Various types of thermal-monitoring technique are discussed and

compared, and it is concluded that the DC-injection-based method has significant benefits over the other methods for stator-winding thermal-monitoring purposes.

Section 3.6 summarizes the chapter.

3.2 DC-SIGNAL-INJECTION METHODS FOR GRID-CONNECTED IMS

It was first described by D. Paice in the year of 1980 to identify the stator resistance using DC-injection methods for a grid-connected IM [32]. A small DC current is successfully excited in the stator winding of an IM using anti-parallel diodes in one of the motor phase windings, such as the one circled in red in Figure 3.1.

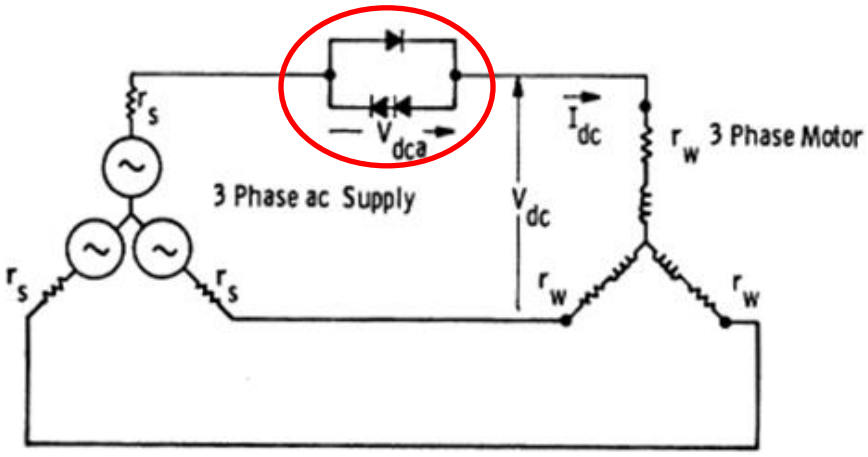

Figure 3.1 The DC-injection IMs via power diodes [32].

However, this method is highly intrusive, because extra circuitry, including anti-parallel diodes and measurement analog circuits, are required to excite and extract the desired DC components. In addition, the amount of DC injection cannot be controlled, which means that this method continuously induces an uncontrollable torque pulsation and extra heat dissipation in power diodes and the motor.

An improved method is reported in [33] and shown in Figure 3.2, where the diodes are replaced by an n-channel enhancement-type power metal-oxide-semiconductor field-effect transistor (MOSFET), and an external resistor R_{ext} is connected in parallel.

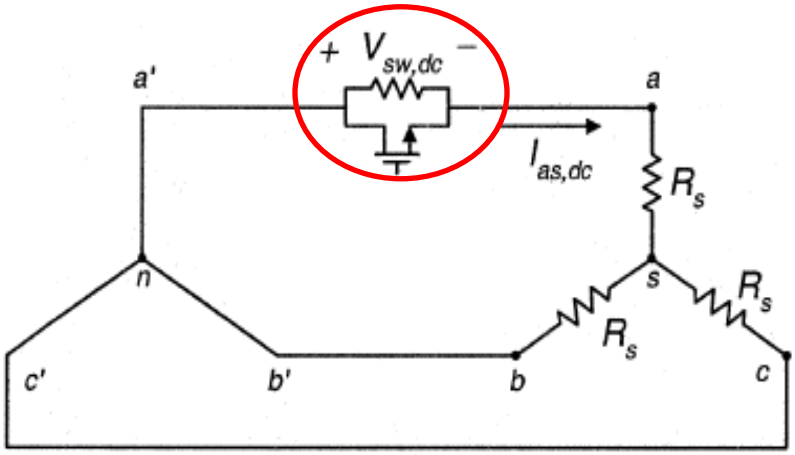

Figure 3.2 The DC-injection IMs via a power MOSFET [33].

To inject a DC bias into a motor, the MOFSFET is turned off when phase-*a* current $i_{as} > 0$, and turned on when $i_{as} < 0$. R_{ext} is adjusted according to the nominal stator resistance and load current, so that the resultant torque distortion and power dissipation are within an acceptable level.

In addition, considering that the thermal behavior changes much slower than the motor dynamics, it is feasible to inject the DC component in the motor intermittently, which also helps to reduce the effects of torque ripple and power loss.

However, for this method, extra circuitry is still required for the DC excitation; therefore, this method remains intrusive. Furthermore, the value of the parallel resistance

R_{ext} has to be pre-adjusted offline for any given motor; and the actual amount of DC injection is varied when there is a load change.

The DC-signal-injection method can also be implemented in a soft-starter-connected IM [15, 34, 35]. As shown in Figure 3.3, during the injection period, a short delay is introduced to the gate signal of one thyristor, say V_{G1}, after phase-*a* current passes a zero-crossing. Therefore, some level of DC current is intermittently injected into the motor winding. The delay angle for phase *a* is indicated in Figure 3.4, and is usually small to limit the torque pulsation and extra power loss within an acceptable level.

In this case, there is no additional hardware required for this DC-injection method, and this method is therefore non-invasive, simple, low cost, and accurate.

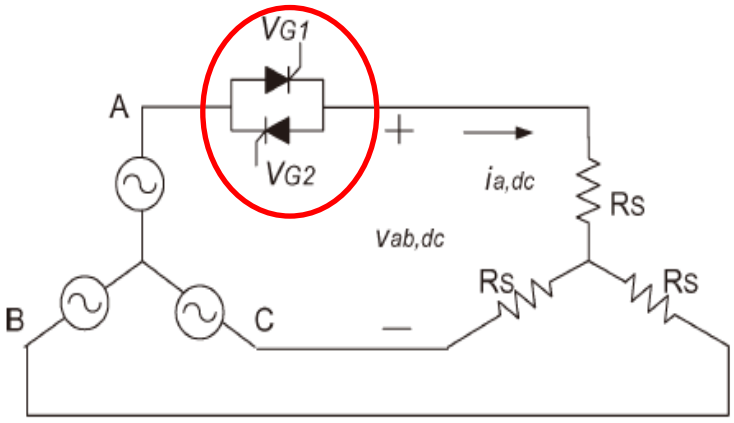

Figure 3.3 DC equivalent circuit of motor, source, and the soft starter [15].

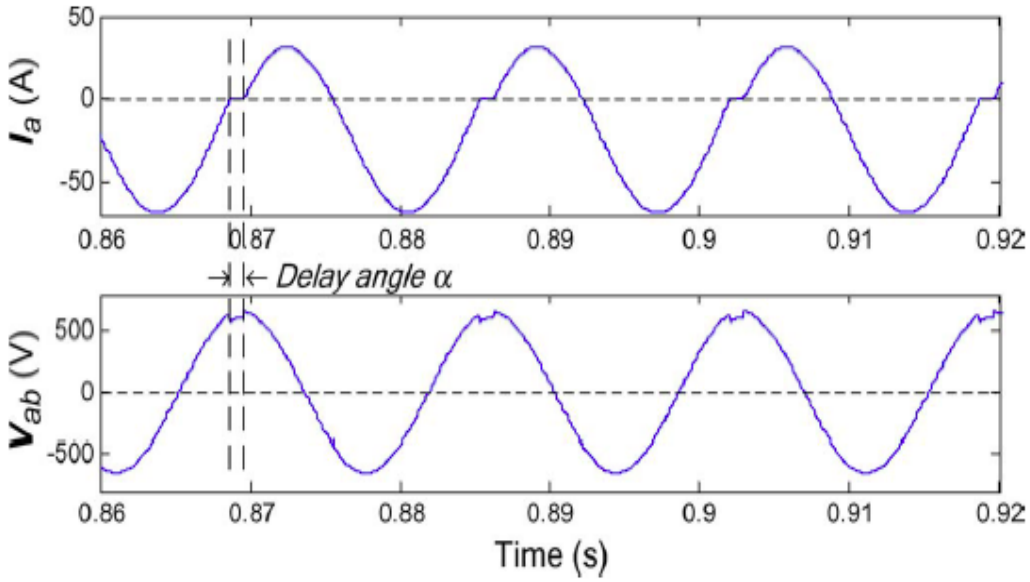

Figure 3.4 Waveforms for DC-injection method in a soft-started IM [15].

3.3 DC-SIGNAL-INJECTION METHODS FOR OPEN-LOOP-CONNECTED IMS

Figure 3.5 below presents a general control block diagram for an open-loop-controlled IM, where the space vector PWM (SVPWM) method is used to generate three-phase terminal voltage commands for any given speed reference ω^* via the widely known '*constant volts/Hz*' method.

The 'constant volts/Hz' control is aimed at controlling the induction machine at quasi-steady state, by varying the amplitude of the fundamental supply voltage and its frequency [36]. The amplitude of the fundamental voltage is computed from the stator pulsation by adopting an empirical function that compensates for the stator resistive drop, and keeps the magnitude of the flux approximately constant [36].

This open-loop control method is simple and low cost, but this procedure is not valid during transient conditions, so the crucial variables (torque and flux linkage) cannot be adequately regulated in this situation and presents poor dynamic response [36, 37]. Besides, the absence of regulation results in the open-loop control performances highly affected by the load profile [36].

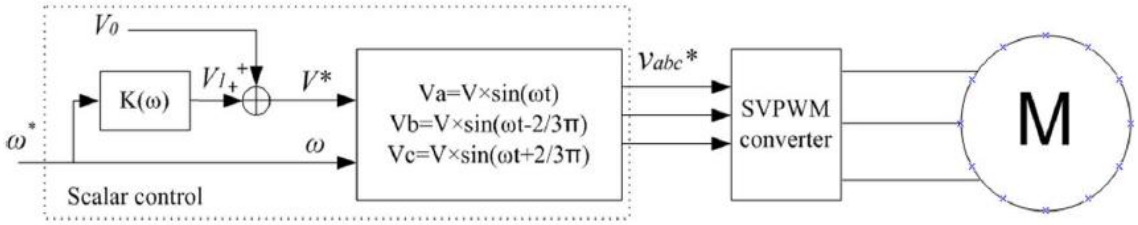

Figure 3.5 Open-loop-controlled IMs with SVPWM method [38].

For an open-loop-controlled inverter-fed IM, a practical way to excite a DC bias is to directly modifying the inverter control [38, 39] by superimposing a DC-voltage command on the original voltage command. Thus, for this example with SVPWM method in Figure 3.5, an easy way to excite an additional DC bias in the motor winding is to shift the voltage command locus directly [38].

As shown in Figure 3.6 [38], the locus for the modified voltage command vector is indicated by the red dotted curves. Since the DC voltage offset is added in the *d*-axis only, it can be observed directly that the command locus is purely shifted in the horizontal axis as we might anticipated.

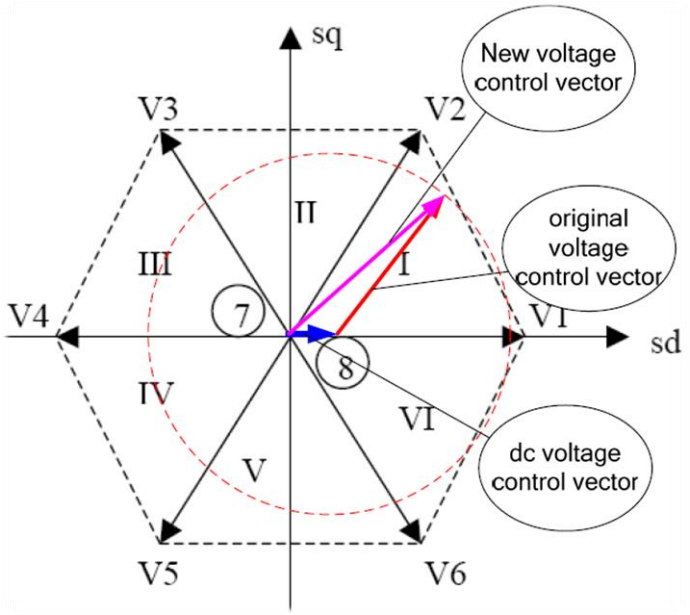

Figure 3.6 SVPWM voltage command locus with added DC bias [38].

Note that a typical IM-drive system only contains phase-current sensors and DC-link-voltage sensors; motor terminal voltages are rarely measured. If voltage commands are used for terminal-voltage estimation, inverter non-idealities will cause significant errors for the extraction of the DC voltage; thus, an accurate stator-resistance estimate cannot be guaranteed.

To solve this problem, a look-up table can be used to store the dependency of the DC-voltage offset on the AC-load-current magnitude under the same voltage command in [39]; the estimated DC-voltage values will then be corrected or modified, allowing for a high precision of the stator-resistance estimation. Similarly, a look-up table in [38] is constructed to compensate the motor-drive errors. However, for the look-up-table-based methods, reliable estimation cannot be guaranteed at all load levels and speed levels other

than the pre-calibrated ones; in addition, the complete calibration is cumbersome and time-consuming.

3.4 DC-SIGNAL-INJECTION METHODS FOR CLOSED-LOOP-CONNECTED IMS

There are two popular closed-loop motor-control algorithms used in the industry: the field-oriented-control (FOC) method and the direct-torque-control (DTC) method. In this section, it will first explain the basics of the each of the two closed-loop feedback control schemes, and then present the literature review of the DC-signal injection method developed for these two control methods.

3.4.1 DC-signal-injection methods for field-oriented-controlled IMs

In 1971, F. Blaschke [40, 41] presented the first paper on field-oriented control (FOC) for induction machines. Since then, this technique has been completely developed and widely commercialized in industry applications [42, 43].

The FOC scheme is carried out in a *dq* reference frame rotating at the stator frequency. In particular, the *d*-axis is aligned with the rotor flux linkage; thus, the rotor flux and torque can be separately controlled by the stator current *dq* components: the rotor flux linkage is a function of the *d*-axis stator current i_{sd}^{e}, while the developed torque is controlled by the *q*-axis current i_{sq}^{e} [14]. The desired torque profile is either provided by the customer, or directly obtained from the regulator in the outer speed loop with a command $\omega_{m,ref}$. Note that the decoupling between flux linkage and torque control is achieved only if the rotor flux position is accurately obtained [14].

There are generally two types of FOC scheme: direct FOC scheme and indirect FOC scheme. Most of literature adopts the following definition [44]: direct FOC refers to the

case where flux vector position is measured or estimated, while indirect FOC refers to an implementation where the flux vector position is calculated from the reference values (feedforward control) and mechanical speed or position measurements.

To implementing DC injection method on an FOC motor drive system, in [45], a DC current is forced into a standstill IM through *dq*-current loops of a typical FOC scheme: the *q*-axis stator-current command is a positive DC value, and the *d*-axis stator-current command is zero. The same test with a different level of DC current is performed again to eliminate inverter non-linear effects.

However, this method is only applied to IMs at standstill for motor-parameter identification; there is no AC-power fed into the motor, and the motor is effectively not generating any output electromagnetic torque.

The DC-signal-injection method in [46, 47] is implemented in a closed-loop-controlled IM with an FOC scheme at normal operation of an AC-drive system. However, the control loops are disconnected during the injection period, so that a DC offset is excited by directly modifying the voltage commands like an open-loop system in section 3.3, and will not be cancelled out by the high-bandwidth *dq* current loops. However, since this injection method disconnects the feedback control intermittently, the overall system control performance is highly degraded. Furthermore, additional voltage sensors are required to obtain an accurate estimate of DC voltage, which are not available in a standard drive system.

So far, the injection method in [48, 49] is proved to be simple, non-invasive, and most practical to implement in a standard or typical FOC motor-drive system. The accuracy is proved to be guaranteed under various operating conditions and cooling modes.

In this method [48, 49], three-phase DC-current offsets are intermittently superimposed on fundamental currents by commanding additional sine-wave current ripples varying at synchronous speed in the synchronous *dq* frame, as shown in Figure 3.7 and equation (3.1).

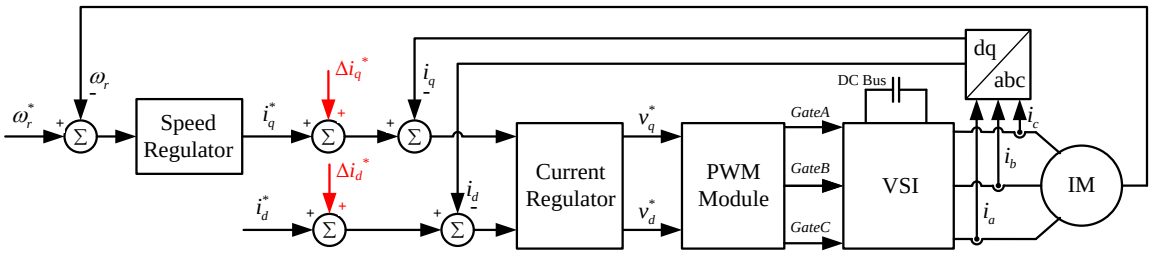

Figure 3.7 DC-current injection in an FOC IM-drive system [48, 49].

$$\left.\begin{aligned} \Delta i_d^* &= I_{dc}\cos(\theta) \\ \Delta i_q^* &= -I_{dc}\sin(\theta) \end{aligned}\right\} \tag{3.1}$$

An improved terminal-voltage estimation method is also proposed by the same authors [48, 49], where inverter non-idealities, including dead-time effects, voltage drop of the switching devices, and turn-on/turn-off time delay of the drive system, are well taken into account.

This proposed signal-processing technique requires no extra memory to store a look-up table compared to the methods in [38, 39], and can be universally applied to machines especially considering the wide-speed range and load level of variable-frequency drives (VFDs), and unexpected abnormal cooling situations [15, 48-53].

However, it should be pointed that although the resultant torque pulsation is limited, this method is not taking full advantage of the flexibility of the FOC scheme, and the

fundamental-speed torque ripple induced by the DC injection is not mitigated or reduced to the lowest level.

3.4.2 DC-signal-injection methods for direct-torque-controlled IMs

DTC algorithm was first proposed by Isao Nakahashi and Toshikiko Noguchi in the middle of 1980's [54].

This approach provides direct, accurate and fast-dynamic control for the motor electromagnetic torque and flux linkages [14]. This revolutionary concept is able to compete with the well-known field-oriented control (FOC), and also widely used in industrialized variable-frequency drives (VFD) nowadays.

The control block diagram for a typical DTC IM is shown in Figure 3.8 [54], where DTC scheme is implemented in the stationary *dq* reference frame (superscript *s* indicates the analysis is carried out in the stationary *dq* frame).

Conventionally, the stator flux linkages $\left(\psi_{sd}^{s}, \psi_{sq}^{s}\right)^{T}$ is estimated from the stator voltages $\left(u_{sd}^{s}, u_{sq}^{s}\right)^{T}$ and stator currents $\left(i_{sd}^{s}, i_{sq}^{s}\right)^{T}$; while the electromagnetic torque T_{em} is obtained from the already estimated $\left(\psi_{sd}^{s}, \psi_{sq}^{s}\right)^{T}$ and directly-measured currents $\left(i_{sd}^{s}, i_{sq}^{s}\right)^{T}$ [54].

With the predetermined electromagnetic-torque reference $T_{em,ref}$ (or obtained from the regulator in the outer speed loop with a command $\omega_{m,ref}$) and stator-flux-linkage magnitude reference $\Psi_{s,mag,ref}$, a DTC switching table is utilized to generate the duty ratio commands to the three-phase two-level power inverter system, so as to regulate the flux linkages and electromagnetic torque.

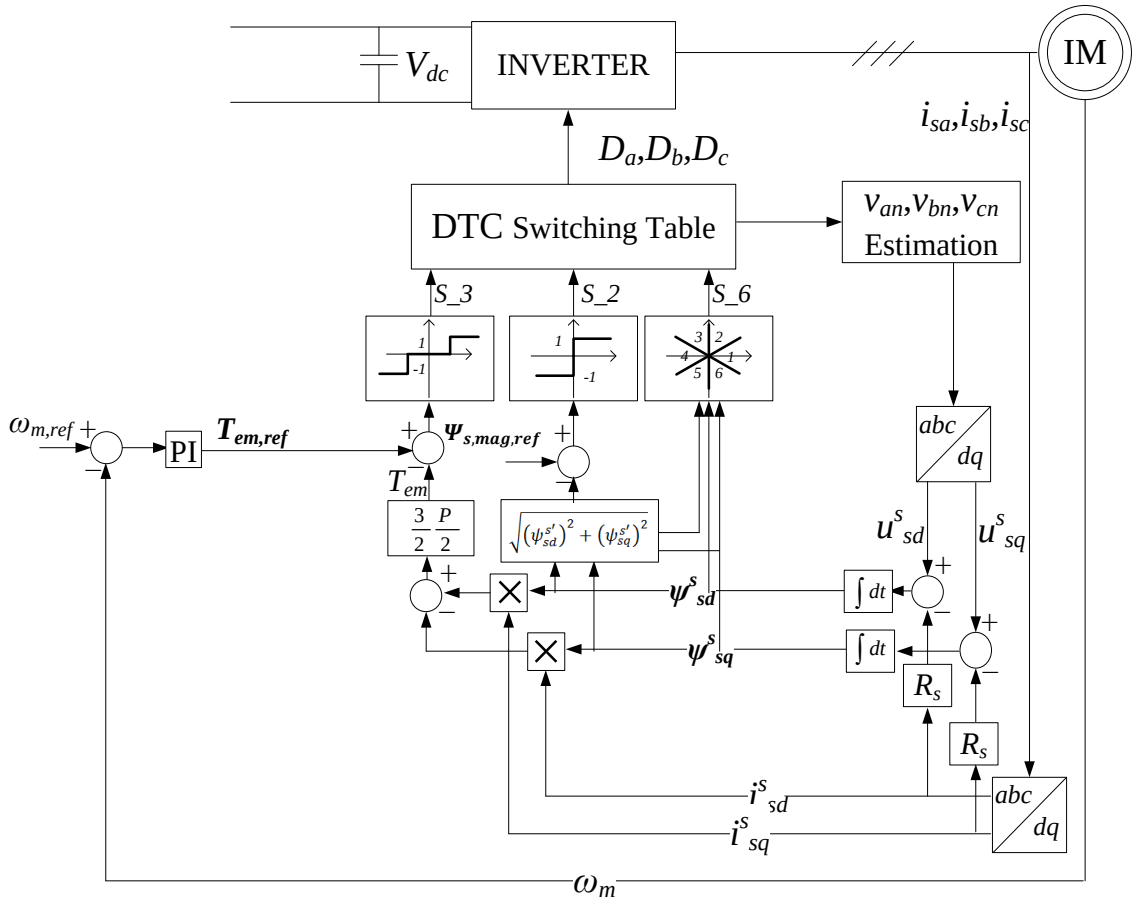

Figure 3.8 Block diagram for DTC scheme.

It is observed in literature that although the DTC scheme is preferred for high-dynamic applications, and has been commercialized and widely used in the industry, there is a lack of research implementing the DC-injection technique in a inverter-fed motor-drive system with a DTC motor-control scheme.

3.5 IMPLEMENTATION OF DC INJECTION IN THERMAL-MONITORING AREAS

Thermal monitoring of motor stator winding is of significant importance for the prevention of overheating, insulation breakdown, malfunction, and lifetime reduction for electric machines [55-57]. As pointed out by [15, 39], the motor's life is reduced by roughly 50% for every 10 ℃ increase above its stator winding temperature design limit. In addition, accurate thermal monitoring also contributes to the efficiency evaluation, the improvement of the machine's utilization, and the enhancement of the overall system's performance.

Among all the thermal monitoring techniques, the installation of embedded temperature sensors is the most accurate, but it only measures the temperature in a specific point of the winding or the stator lamination [58]; and it is not cost-effective for many low-to-medium horse power machines [33, 48, 49].

Aside from the direct temperature measurement, there are two major techniques for the stator-winding temperature estimation: thermal-model-based approaches and parameter-based approaches.

The thermal-model based approaches estimate the temperature from an equivalent thermal circuit [59-63]. The most well-known method is the lumped-parameter thermal network proposed by Mellor and Turner [59]. This detailed system is an 8^{th} order dynamic model, with a large number of thermal resistances and capacitances, either derived analytically from the machine's dimensions and material thermal properties, or directly obtained from various offline tests. With some acceptable sacrifices of accuracy, a few simplified thermal models have been proposed [60-62]; the computation is less complicated, but there are still a significant amount of model parameters to be identified

from the motor specification and offline experiments. To summarize, this method is complex; it cannot be universally implemented for different types of electric machines [59]; and the accuracy cannot be guaranteed under various cooling conditions [15, 33, 34, 48, 49].

On the other hand, the parameter-based approach uses the stator-winding resistance as a direct indicator of stator-winding temperature. The approach is universal and has significant advantages over the thermal-model-based approach: its accuracy is not affected by the machine's specification, operating condition and cooling mode [48, 49]. Theoretically, the stator winding resistance may be estimated from the machines' electric equivalent model [53]; however, since the stator resistance is much smaller than the stator reactance [48, 49], the estimation performance is too sensitive to motor inductance variations [15], and not accurate enough particularly during high-speed operation. As mentioned in [33], a more reliable way to identify the stator winding resistance is through the injection of a DC bias signal. This is especially applied to motors under normal-speed operating conditions, where the stator and rotor (referred to the stator side) winding reluctance is much more significant compared to the winding resistance: $X_r \gg R_r$ and $X_s \gg R_s$.

As already reviewed in sections 3.2 - 3.4, DC-injection methods have been widely developed for the grid-connected IMs, open-loop-controlled IMs, and also the closed-loop-controlled FOC IMs.

Once the DC signal is successfully excited in the motor winding, the winding resistance R_s can be directly obtained from the injected DC voltage and current offsets at steady state; thus the stator winding temperature can also be estimated using equation

(3.2) according to IEEE standard [64], where R_b is the resistance at known temperature t_b, R_t is the resistance during the test, t_t is the estimated test temperature, and k_1 is a constant based on the winding material. As presented in International Annealed Copper Standard (IACS), k_1 is 234.5 for 100% IACS conductivity copper, or 225 for aluminum, based on a volume conductivity of 62%.

$$t_t = \left(\frac{R_t}{R_b}(t_b + k_1)\right) - k_1 \tag{3.2}$$

To summarized, although an accurate estimate is only guaranteed at steady state, the DC-injection-based stator-winding temperature estimation technique is independent of all other motor parameters and inherent motor asymmetry, and is proved to be a most reliable approach for obtaining an accurate estimate of average stator resistance and winding temperature under various operating conditions and cooling modes [[15]].

3.6 CHAPTER SUMMARY

This chapter presents the-state-of-the-art of the active DC-signal-injection method applied to grid-connected IMs, open-loop-controlled IMs, and closed-loop-controlled IMs in detail.

The DC-injection methods lead to a simple, low-cost, accurate, and non-invasive thermal-monitoring scheme for IMs, where the stator-winding temperature is indirectly estimated from stator resistance during the normal speed operations.

In addition, this chapter identifies that further research need to be carried out in field-oriented-controlled (FOC) IMs to mitigate the fundamental-frequency ripple (caused by the DC injection) to a lower level by taking the advantage of the *dq* current control scheme. Also, it is desired to extend the DC-injection method to direct-torque-controlled

(DTC) motor drives, so that an injection-based thermal monitoring scheme can be developed for DTC drives as well. All the problems identified in this chapter will be carefully and thoroughly discussed in Chapter 6 , Chapter 7 , and Chapter 8 .

CHAPTER 4 MULTI-PHYSICS MODELING WORK OF A RECLOSER SYSTEM

4.1 INTRODUCTION

This chapter is about the analysis and modeling results of a typical linear-motion energy-conversion system with active DC excitation: a vacuum automatic-recloser system energized from a DC capacitor [65, 66].

Section 4.2 presents the detailed multi-physics modelling effort. First, it briefly explains the major components of the selected recloser system, how these components are connected, and how the system can operate in two-way linear motion. Then it presents a detailed mathematical model description of the recloser system, including the electromagnetic subsystem, the mechanical subsystem, and the complete multi-physics system. It is finally derived that the complete automatic recloser system can be mathematically described as a non-linear discontinuous eighth-order dynamic system.

Section 4.3 presents the simulation results of the developed parameterized recloser modelling tool, including the trajectories and the velocities of the two-way linear-motion of all different moving blocks of the recloser system. These results show that the proposed model can guarantee the automatic opening and closing processes of the recloser system with the given electromagnetic excitation. The detailed simulation results also present the moving sequence of all different moving components and the highly discontinuous feature of the motion. The above mentioned features will finally be validated by high-speed video camera measurement in Chapter 5 .

Section 4.4summarizes the chapter.

4.2 MODELING WORK

A simplified model for a vacuum automatic recloser is illustrated in Figure 4.1. As shown in Figure 4.1, it contains a vacuum interrupter, inside of which there is a moving contact and a stationary contact. The high power current will flow though the two contacts and conduct the power line.

There is also a solenoid case sitting outside of the interrupter, as in Figure 4.1. This auxiliary system contains two electromagnetic sources, a solenoid and a permanent-magnet (PM) disk, which are used to energize various moving components of the recloser and initiate the opening or closing motion of the moving contact to interrupt or reenergize the power line.

Aside from the moving contact, there are also other moving components to help transfer the electromagnetic energy stored in the solenoid and PM disk to the kinetic energy of the moving contact to trigger the roundtrip operations. All the moving components are summarized as follows:

(1) A moving contact inside the vacuum interrupter, denoted by m_1;

(2) A magnetic actuator block or plunger, sitting inside and through the center of the solenoid, denoted by m_3;

(3) A non-magnetic shaft connecting the moving contact and the actuator block, denoted by m_2.

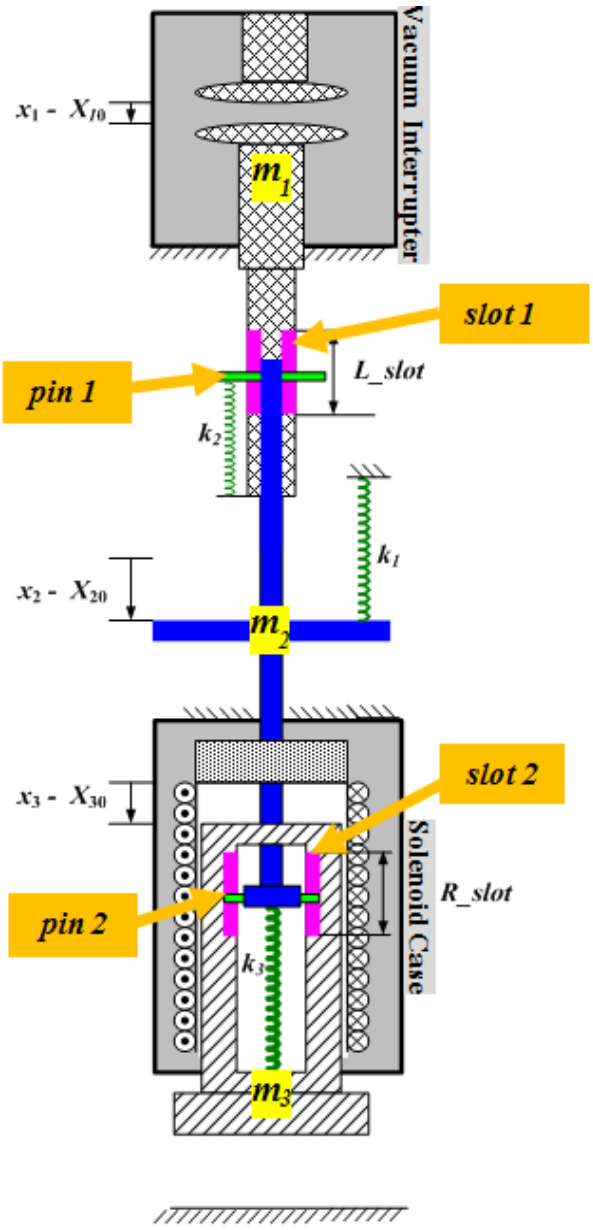

Figure 4.1 A simplified recloser model.

As shown in Figure 4.1, x_1, x_2, and x_3 are displacements for the three masses respectively, with X_{10}, X_{20}, and X_{30} as the initial conditions; *L_slot* and *R_slot* are the lengths of the two slots, *slot 1* and *slot 2*.

It is clearly illustrates in Figure 4.1 how the three assembled masses are connected by two compressed springs k_2 and k_3, while m_2 is compressed by an opening spring k_1. Thus, all three masses are soft-connected by springs in series.

Aside from these soft-spring connections, there are two slot-type connections: the first slot on m_1 is denoted as *slot 1*, and the second slot on m_3 is denoted as *slot 2*, shown in Figure 4.1. *pin 1* is rigidly attached to m_2 and can slide inside *slot 1* with restricted movement; similarly, *pin 2* is attached to m_2 and can only slide inside *slot 2*. Because of the spatial limit of the slots, the vacuum bottle, and the solenoid case, the three masses can only move within the limited space of the recloser.

Generally, the solenoid is energized from a DC capacitor via a MOSFET switch, and provides extra magnetic strength to aid (or oppose) the initial permanent-magnetic (PM) field. The extra strength causes the change of force balance and motion of the magnetic plunger m_3 only (the shaft m_2 is non-magnetic). The kinetic energy of m_3 is then transferred to m_2 and the moving contact m_1 inside the vacuum bottle, and finally creates either opening or closing motion.

The detailed mathematic model of the multi-physics dynamic system is divided into two subsystems: an electromagnetic subsystem and a mechanical subsystem, which are presented as follows.

4.2.1 The electromagnetic subsystem

As illustrated in the cross-sectional view of the solenoid case in Figure 4.2, there are two magnetic sources contribute to the magnetic force: a coil with N turns inside the solenoid case and a PM disk with a flux φ_r. The loop of the flux path is indicated by red arrows.

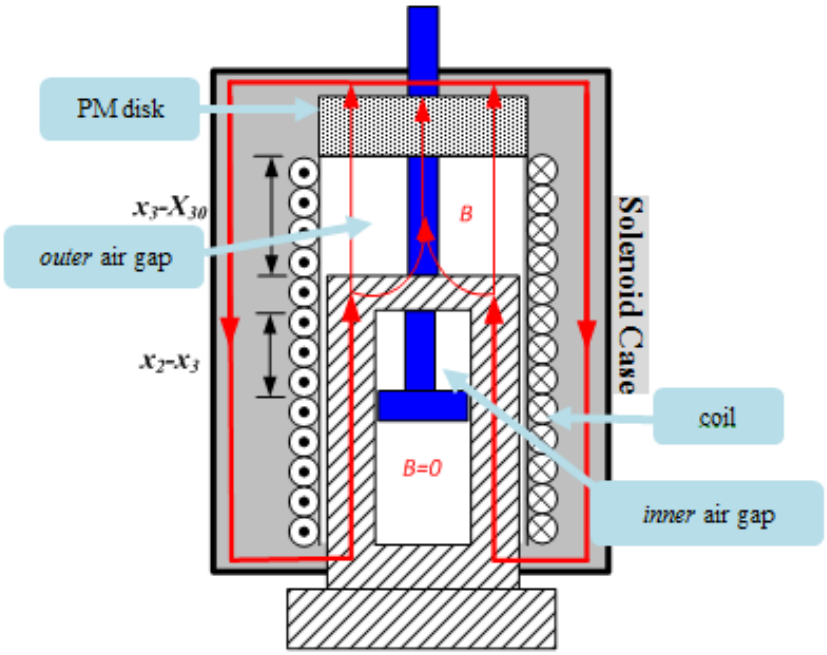

Figure 4.2 A simplified recloser electromagnetic model.

Due to the relative displacement, there are two air gaps inside the solenoid: the first is the air gap between the PM disk and the plunger (m_3), denoted as the *outer* air gap; the second is the air gap between the plunger m_3 and the shaft m_2, denoted as the *inner* air gap. Because the plunger (m_3) and the solenoid case are both made of magnetic steel, almost no flux flows through the *inner* air gap; therefore, the *inner* air gap has a negligible effect on the total reluctance of the flux path. In addition, because m_2 is non-magnetic, the flux density is uniform inside the *outer* air gap.

Magnetic circuits can be drawn and analyzed as equivalent electric circuits, in which flux is equivalent to current; MMF is equivalent to voltage; reluctance is equivalent to resistance.

In magnetic circuits with air gaps, it is often assumed that the relative permeability of the magnetic steel is extremely high (compared to the air gap) when unsaturated (this specific recloser uses soft steel with unsaturated relative permeability $\mu_{rsteel} \approx$ 600-1000 >> 1); that means that it is acceptable to simplify the magnetic circuit by assuming the reluctance of the steel is negligible with respect to the reluctance of the air gaps). For this recloser design, the *outer* air gap reluctance $R(t)$ and the PM reluctance R_m dominate the flux path, as denoted in the magnetic circuit in Figure 4.3, and expressed as follows, where r_3, r_2, r_1,r_s are the radii for the *outer* air gap, the bobbin top, the PM disk, and the shaft, respectively; l_1 is the width of PM disk; μ_{rPM} and μ_{rshaft} are the relative permeability of the PM disk and shaft.

The reluctance for the *outer* air gap is $R(t)$, is a function of $x_3(t)$ and given by

$$R(t) = \frac{x_3(t)-X_{30}}{\mu_0\pi(r_3^2-r_s^2)} \,||\, \frac{x_3(t)-X_{30}}{\mu_0\mu_{rshaft}\pi r_s^2}, \tag{4.1}$$

Similarly, the total reluctance for the PM disk, R_m, is made up of three parallel paths. It is constant and is given by

$$R_m = \frac{l_1}{\mu_0\pi(r_2^2-r_1^2)} \,||\, \frac{l_1}{\mu_0\mu_{rPM}\pi(r_1^2-r_s^2)} \,||\, \frac{l_1}{\mu_0\mu_{rshaft}\pi r_s^2}, \tag{4.2}$$

Since the shaft is non-magnetic and μ_{rPM} =1.042 $\approx$ 1, the two equations can be simplified as shown in equations (4.3) - (4.4):

$$R(t) \approx \frac{x_3(t)-X_{30}}{\mu_0\pi r_3^2}, \tag{4.3}$$

$$R_m \approx \frac{l_1}{\mu_0\pi r_2^2}. \tag{4.4}$$

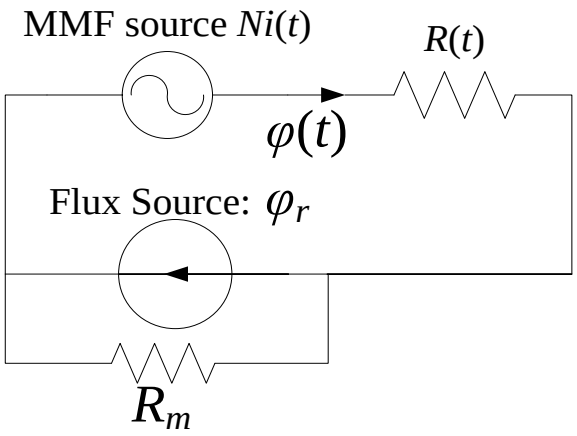

Figure 4.3 The magnetic circuit of the recloser.

Next, *superposition* is used to solve the linear magnetic circuit in Figure 4.3 to find the flux $\varphi(t)$ and the corresponding flux linkage $\lambda(t)$for the solenoid, shown as follows:

$$\varphi(t) = \frac{N \cdot i(t)}{R_m + R(t)} + \frac{R_m}{R_m + R(t)} \varphi_r, \tag{4.5}$$

$$\lambda(t) = N\varphi = \frac{N^2 \cdot i(t)}{R_m + R(t)} + \frac{N \cdot R_m}{R_m + R(t)} \varphi_r = L(t) i(t) + N\varphi_m(t), \tag{4.6}$$

where $L(t) = \frac{N^2}{R_m + R(t)}$ and $\varphi_m(t) = \frac{R_m}{R_m + R(t)} \varphi_r$.

Faraday's law is further implemented to derive the induced voltage $u(t)$ across the solenoid, and the voltage is expressed as :

$$u(t) = -e(t) = -\left[-\frac{d\lambda(t)}{dt}\right] = L(t)\frac{di(t)}{dt} - N\frac{Ni(t) + R_m\varphi_r}{(R_m + R(t))^2}\frac{dR(t)}{dt}, \tag{4.7}$$

where $u(t)$ is denoted in the electric circuit in Figure 4.4.

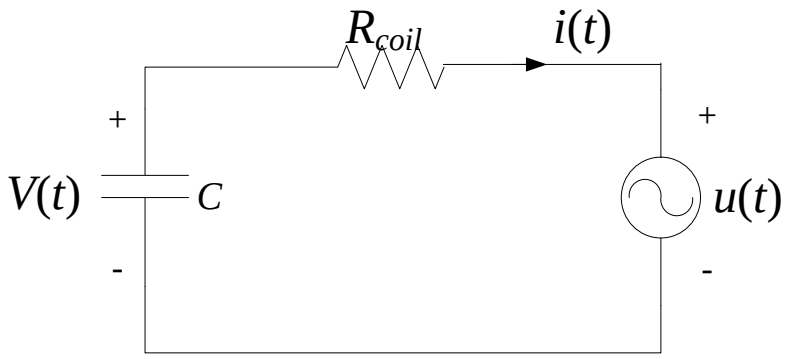

Figure 4.4 The equivalent recloser energizing electric circuit.

From here onwards, the prime (double prime) symbol on any given variable represents the corresponding first (second) time derivative.

Substituting equation (4.1) into equation (4.7) yields

$$u(t) = \frac{N^2}{R_m + \frac{x_3(t) - X_{30}}{\mu_0 \pi r_3^2}} i'(t) - N \frac{Ni(t) + R_m \varphi_r}{(R_m + \frac{x_3(t) - X_{30}}{\mu_0 \pi r_3^2})^2} \frac{1}{\mu_0 \pi r_3^2} x_3{}'(t). \tag{4.8}$$

A MOSFET is closed to apply a voltage *V* from a pre-charged DC capacitor C to the solenoid, so as to supply the current starting in one direction through the solenoid to open the recloser, or in the opposite direction to close the recloser. The voltage and current equations for the circuit in Figure 4.4 are given in equation set (4.9). The last row in equation set (4.10) enforces a directional-current-flow requirement for the opening (or closing) process.

$$\begin{cases} C \frac{dV(t)}{dt} = -i(t) \\ i(t) R_{coil} + u(t) = V(t) \\ u(t) = \frac{N^2}{R_m + \frac{x_3(t) - X_{30}}{\mu_0 \pi r_3^2}} i'(t) - N \frac{Ni(t) + R_m \varphi_r}{(R_m + \frac{x_3(t) - X_{30}}{\mu_0 \pi r_3^2})^2} \frac{1}{\mu_0 \pi r_3^2} x_3{}'(t) \\ \text{For opening: } i(t) < 0; \text{ for closing: } i(t) > 0 \end{cases}. \tag{4.9}$$

The initial condition for the above state model is listed as follows:

$$\begin{cases} V(t=0+) = -|V_{open}| \\ i(t=0+) = 0 \end{cases}, \tag{4.10}$$

where the negative sign of the capacitor voltage $V(t = 0+)$ is determined by the requirement $i(t) < 0$ for starting to open, which is explained later.

Since m_2 is non-magnetic material, the eletro-magnetic force is only imposed on m_3. This force is derived from considering the energy as follows.

The electromagnetic force on m_3, $F_{mag3}(t)$, is obtained by applying the *conservation of energy principle* to the coupled electromagnetic field for an arbitrary displacement $\Delta x_3(t)$ as follows:

$$F_{mag3}(t)\Delta x_3(t) = u(t)i(t)\Delta t + u(t)\frac{R_m\varphi_r}{N}\Delta t - \Delta W_{mag}(t), \tag{4.11}$$

where

$$W_{mag}(t) = \frac{1}{2}L(t)\cdot i(t)^2 + \frac{1}{2}(R(t)+R_m)\cdot\varphi_m(t)^2 + Ni(t)\varphi_m(t). \tag{4.12}$$

The reference direction is in the + x-axis. $W_{mag}(t)$ is the total energy stored in the magnetic field [67]. It is observed from equation (4.12) that the complete magnetic energy is made up of three components: the first one is the energy stored in the coil with variable self-inductance $L(t)$, the second one is the energy caused by the PM disk alone, and the third one is the energy due to the mutual effect of the coil and the magnet. Considering the mutual component, it is better not to separate the solenoid force from the PM force; therefore, $F_{mag3}(t)$ is the combined magnetic force exerted on the plunger (m_3) due to the coupled magnetic field.

It is shown in equation (4.11) that the first term on the right-hand side is the input electric energy from the coil during Δt. The second term is the equivalent input electric energy from the constant PM flux source φ_r, which is replaced by an equivalent MMF

source with an *N*-turn DC current coil $\frac{R_m\varphi_r}{N}$ using *Norton's equivalent theorem*. The last term represents the change of magnetic energy. This magnetic force is then derived from equation (4.11) as follows:

$$F_{mag3}(t) = \frac{u(t)i(t)dt+u(t)\frac{R_m\varphi_r}{N}dt-dW_m(t)}{dx_3(t)} = \frac{u(t)\left[i(t)+\frac{R_m\varphi_r}{N}\right]}{x_3{}'(t)} - \frac{\mathrm{d}W_m(t)}{dx_3(t)}. \tag{4.13}$$

Substituting equations (4.7) and (4.12) into equation (4.13) above yields the eletro-magnetic force on m_3, $F_{mag3}(t)$, as follows:

$$\begin{aligned} F_{mag3}(\mathrm{t}) &= \frac{\left[\frac{N^2}{R_m+R(t)}i'(t)-N\frac{Ni(t)+R_m\varphi_r}{(R_m+R(t))^2}R'(t)\right]\left[i(t)+\frac{R_m\varphi_r}{N}\right]}{x_3{}'(t)} - \left[N\frac{Ni(t)+R_m\varphi_r}{R_m+R(t)}\frac{i'(t)}{x_3{}'(t)} - \right. \\ &\quad \left. \frac{1}{2}\left(\frac{Ni(t)+R_m\varphi_r}{R_m+R(t)}\right)^2\frac{dR(t)}{dx_3(t)}\right] \\ &= -\frac{1}{2}\left(\frac{Ni(t)+R_m\varphi_r}{R_m+R(t)}\right)^2\frac{dR(t)}{dx_3(t)}. \end{aligned} \tag{4.14}$$

Finally, substituting equation (4.3) into equation (4.14) yields

$$F_{mag3}(t) = -\frac{1}{2\mu_0\pi r_3^2}\left(\frac{Ni(t)+R_m\varphi_r}{R_m+\frac{x_3(t)-X_{30}}{\mu_0\pi r_3^2}}\right)^2. \tag{4.15}$$

Because $F_{mag3}(t)$ is always negative, its reference direction is changed to a negative *x*-axis; thus the electromagnetic force is denoted as follows:

$$F_{mag3}(t) = \frac{1}{2\mu_0\pi r_3^2}\left(\frac{Ni(t)+R_m\varphi_r}{R_m+\frac{x_3(t)-X_{30}}{\mu_0\pi r_3^2}}\right)^2. \tag{4.16}$$

The expression above can be physically explained as follows:

The electromagnetic force $F_{mag3}(t)$ always tries to hold the magnetic plunger m_3 from opening; in order to open the contact, the input coil current $i(t) < 0$ is required for the solenoid field to oppose the PM field and reduce $F_{mag3}(t)$; in order to close the

contact, $i(t) > 0$ is necessary for the solenoid field to add to the PM field and increase $F_{mag3}(t)$.

There is also some unknown leakage flux, and therefore external leakage reluctance R_{ex}, which is difficult to quantify in terms of geometry and material except that it will cause R_m to be larger than the value defined in equation (4.4).

A correction is therefore made to R_m in equation (4.17), by introducing *a correction factor* k_c to represent the external reluctance R_{ex}. Thus, φ_r and R_m are replaced by φ_r^* and R_m^*, respectively, and derived as follows using *Norton's equivalent theorem*, where $\frac{R_{ex}}{R_m} = k_c$. The modified reluctance model is shown in Figure 4.5.

$$\begin{cases} R_m^* = R_m + R_{ex} = \left(1 + \frac{R_{ex}}{R_m}\right) R_m = (1 + k_c) R_m \\ \varphi_r^* = \frac{R_m}{R_m + R_{ex}} \varphi_r = \frac{R_m}{R_m^*} \varphi_r \end{cases} \tag{4.17}$$

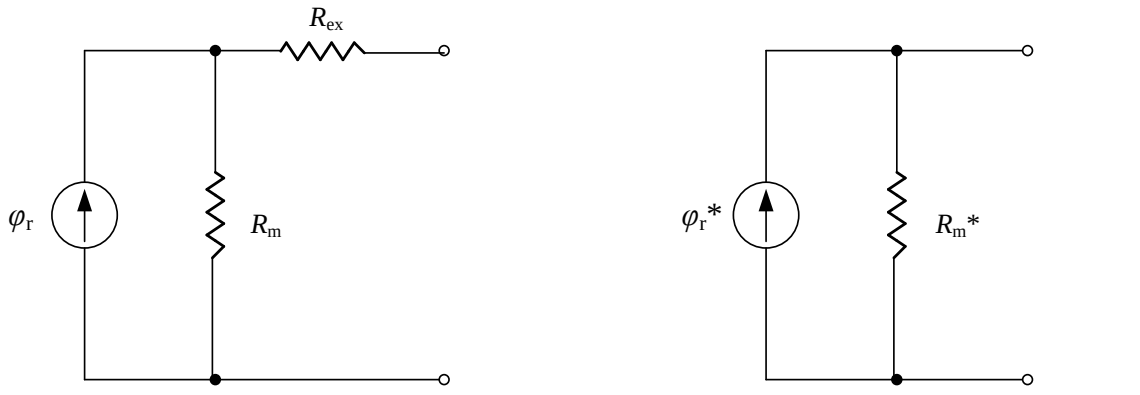

(a) Permanent magnetic sourse (b) Equivalent permanent magnetic sourse

Figure 4.5 Modified recloser PM source model, with k_c factor

4.2.2 The mechanical subsystem

Suppose all masses can move freely within one-dimensional (1-D) space, aside from the derived magnetic force $F_{mag3}(t)$, other forces contributing to the system's motion include spring forces $F_{s1}(t)$, $F_{s2}(t)$, and $F_{s3}(t)$, caused by springs k_1, k_2, and k_3, respectively; and air-pressure force F_{ap}, which is the result of the difference of the air pressure between the vacuum bottle and the open air.

The state equation for the mechanical system is expressed as follows:

$$\begin{cases} x_1''(t) = \frac{1}{m_1}\left[F_{s2}(t) - F_{ap}\right] \\ x_2''(t) = \frac{1}{m_2}\left[F_{s1}(t) - F_{s2}(t) - F_{s3}(t)\right], \\ x_3''(t) = \frac{1}{m_3}\left[F_{s3}(t) - F_{mag3}(t)\right] \end{cases} \tag{4.18}$$

where

$$\begin{cases} F_{s1}(t) = k_1 \cdot (\Delta X_{s10} - (x_2 - X_{20})) \\ F_{s2}(t) = k_2 \cdot (\Delta X_{s20} + (x_2 - X_{20}) - (x_1 - X_{10})) \\ F_{s3}(t) = k_3 \cdot (\Delta X_{s30} - (x_3 - X_{30}) + (x_2 - X_{20})) \\ F_{mag3}(t) = \frac{1}{2\mu_0 \pi r_3^2}\left(\frac{Ni(t) + R^*{}_m \varphi^*{}_r}{R^*{}_m + \frac{x_3(t) - X_{30}}{\mu_0 \pi r_3^2}}\right)^2 \\ F_{ap} = const \end{cases}. \tag{4.19}$$

In equation set (4.19), ΔX_{s10}, ΔX_{s20}, and ΔX_{s30} represent the initial compressions of the three springs.

However, when m_1, m_2, and m_3 are moving separately within the limited space of the recloser, collisions may happen, because of the spatial limits of the two slots, the vacuum bottle and the solenoid case, as shown in Figure 4.6.

In fact, only with these collisions will the electromagnetic energy be rapidly transferred from m_3 to m_2, and finally to m_1, to either open or close the contact, because the electromagnetic excitation only acts on m_3 directly.

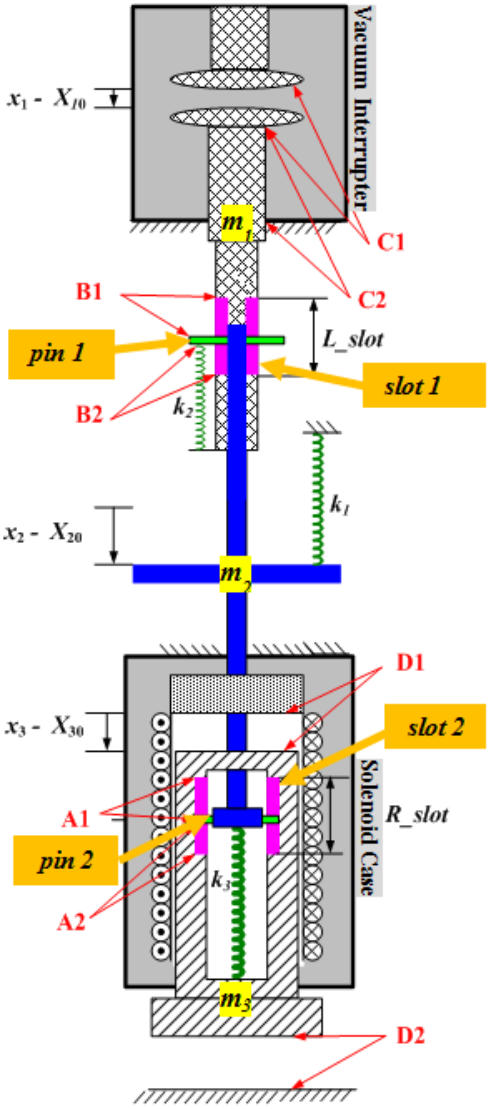

Figure 4.6 Collisions A, B, C, and D in the simplified recloser model.

In Figure 4.6, the movement of *pin 1* is restricted in the *slot 1*, with a width of *L_slot*, approximately 3-4 mm; the movement of *pin 2* is restricted in the *slot 2*, with a width of *R_slot*, about 3-4 mm. When m_1, m_2, and m_3 are all moving separately and their relative

displacements are changing, it is possible for collisions A (A1 or A2) and B (B1 or B2) to happen, denoted in Figure 4.6.

Furthermore, as x_1 is limited by the maximum stroke of the vacuum interrupter, there is another type of collision between m_1 and the vacuum bottle, denoted as C (C1 or C2) in Figure 4.6. Similarly, another collision between m_3 and the solenoid case may occur, denoted as D (D1 or D2). In all, there are four types of collisions.

The collisions bring about collision forces, and thus sudden speed changes in the moving parts, which are modeled as velocity enforcements. The constraints are based on a 1D inelastic-collision model [68], where some of the kinetic energy is transformed into heat and deformation. The model for the above mentioned four types of collision is governed by the following equations.

Assume any given critical condition happens at $t = t_*$, then:

Collision A: when $x_2(t_{*-}) = x_3(t_{*-})$ or $x_2(t_{*-}) = x_3(t_{*-}) + R\_slot$,

$$\begin{cases} x_2'(t_{*+}) = \frac{m_2 x_2'(t_{*-}) + m_3 x_3'(t_{*-}) + m_3 C_1\left(x_3'(t_{*-}) - x_2'(t_{*-})\right)}{m_2 + m_3} \\ x_3'(t_{*+}) = \frac{m_2 x_2'(t_{*-}) + m_3 x_3'(t_{*-}) + m_2 C_1\left(x_2'(t_{*-}) - x_3'(t_{*-})\right)}{m_2 + m_3} \end{cases}; \tag{4.20}$$

Collision B: when $x_2(t_{*-}) = x_1(t_{*-})$ or $x_2(t_{*-}) = x_1(t_{*-}) + L\_slot$,

$$\begin{cases} x_1'(t_{*+}) = \frac{m_1 x_1'(t_{*-}) + m_2 x_2'(t_{*-}) + m_2 C_2\left(x_2'(t_{*-}) - x_1'(t_{*-})\right)}{m_1 + m_2} \\ x_2'(t_{*+}) = \frac{m_1 x_1'(t_{*-}) + m_2 x_2'(t_{*-}) + m_1 C_2\left(x_1'(t_{*-}) - x_2'(t_{*-})\right)}{m_1 + m_2} \end{cases}; \tag{4.21}$$

Collision C: when $x_1(t_{*-}) = X_{10}$ or $x_1(t_{*-}) = X_{1m}$,

$$x_1'(t_{*+}) = -C_3 x_1'(t_{*-}); \tag{4.22}$$

Collision D: when $x_3(t_{*-}) = X_{30}$ or $x_3(t_{*-}) = X_{3m}$,

$$x_3'(t_{*+}) = -C_4 x_3'(t_{*-}). \tag{4.23}$$

The *Coefficient of Restitution* (COR) of any two colliding objects for each collision, C_i $(i = 1, 2, 3, 4)$, is used to describe whether there is energy loss during a collision and how much. It is a fractional value representing the ratio of speeds after and before an impact, and is used to classify the general collision type, as shown in the table below. For our study, COR is always less than one, since some of the kinetic energy is transformed into heat and deformation [68].

Furthermore, during the opening process, because of collision C, the speed of m_1 may decrease to zero first; only m_2 and m_3 will continue moving. Therefore, collision B is replaced by B'.

$$\begin{cases} x_1'(t_{*+}) = 0 \\ x_2'(t_{*+}) = -C_2 x_2'(t_{*-}) \end{cases} \tag{4.24}$$

Table 4.1 General collision type

Type	**Kinetic Energy**	**COR**
Perfectly Elastic	Conserved	$COR = 1$
Partially Elastic (Inelastic)	Not Conserved	$0 < COR < 1$
Perfectly Inelastic	Maximum Possible Loss	$COR = 0$
Hyperelastic	Energy Gained	$COR > 1$

4.2.3 The complete multi-physics system

As presented in Sections 4.2.1 and 4.2.2, the electromagnetic subsystem is mainly a continuous non-linear subsystem once the MOSFET switch is on, while the mechanical

subsystem is described by a continuous model in equation (4.18) and a discontinuous model governed by equations (4.20) - (4.24), when any of the collision (collision A, B (B'), C and D) criteria is satisfied at $t = t_*$.

To model the complete multi-physics system, it is recommended to calculate the system state variables via the continuous model first, and then update the results by checking the discontinuous criteria. The general flow chart appears in Figure 4.7.

The assembled non-linear eighth-order dynamic system for the continuous multi-physics recloser model appears as follows:

$$\begin{cases} x_1''(t) = \frac{1}{m_1}\left[F_{s2}(t) - F_{ap}(t)\right] \\ x_2''(t) = \frac{1}{m_2}\left[F_{s1}(t) - F_{s2}(t) - F_{s3}(t)\right] \\ x_3''(t) = \frac{1}{m_3}\left[F_{s3}(t) - F_{mag3}(t)\right] \\ V''(t) = \dfrac{\frac{CN^2V'(t) - NR^*_m\varphi^*_r}{\left(R^*m + \frac{x_3(t)-X_{30}}{\mu_0\pi r_3^2}\right)^2\mu_0\pi r_3^2}x_3'(t) - CR_{coil}V'(t) - V(t)}{\frac{CN^2}{R^*m + \frac{x_3(t)-X_{30}}{\mu_0\pi r_3^2}}} \end{cases}, \tag{4.25}$$

where $F_{s1}(t),\ F_{s2}(t),\ F_{s3}(t), F_{mag3}(t),$ and F_{ap} are expressed in equation set (4.19).

The first three equations in the complete continuous model above directly come from the mechanical model in equation set (4.18), while the last equation equivalently represents the electric-circuit model in equation set (4.9). The initial condition for the roundtrip from opening to closing is shown as follows:

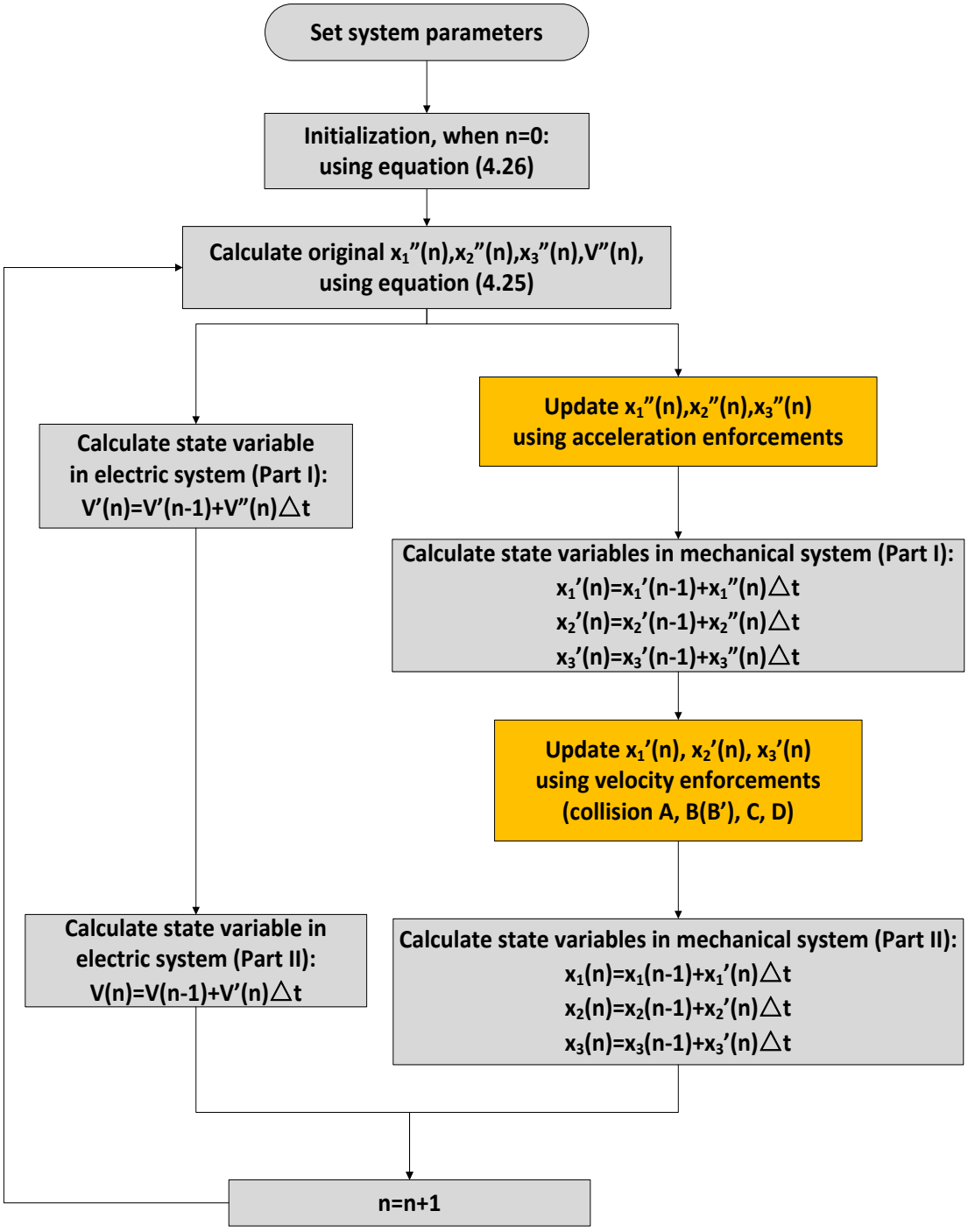

Figure 4.7 Flow chart for modeling the complete recloser system.

$$\begin{cases} V(t\ =\ 0+) = -|V_{open}| \\ V'(t\ =\ 0+) = 0 \\ x_1'(t\ =\ 0+) = 0 \\ x_2'(t\ =\ 0+) = 0 \\ x_3'(t\ =\ 0+) = 0 \\ x_1(t\ =\ 0+) = X_{10} \\ x_2(t\ =\ 0+) = X_{20} \\ x_3(t\ =\ 0+) = X_{30} \end{cases} . \tag{4.26}$$

The first two equations in equation set (4.26) correspond to the initial condition in the electric-circuit model, as shown in equation set (4.10). The other six equations simply indicate that the initial displacements of the three masses are the pre-tuned values X_{10}, X_{20}, and X_{30}; the corresponding initial velocities are all zero, because all of them remain in the closed steady-state position at the very beginning.

As shown in the general flow chart in Figure 4.7, at each time step, the second derivatives of all the state variables are firstly updated using the continuous model in equation set (4.25). Next, the process diverges into two paths to update the obtained continuous results using the discontinuous models. The left path calculates the electric variable *V'*(*n*) and *V*(*n*) using numerical integration (*V'*(*t*) is directly related to the coil current *i*(*t*), as observed in the first row in equation set (4.9)). The right path helps to output the actual mechanical velocities $x_1'(n)$, $x_2'(n)$ and $x_3'(n)$ by integrating the updated accelerations first, and then passing the data through the collision model governed by equation sets (4.20)-(4.24). The corresponding displacements $x_1(n)$, $x_2(n)$, and $x_3(n)$ are finally obtained from numerical integration of the updated velocities.

4.3 MODELING RESULTS

The simulation results for the complete opening-and-closing process of a recloser device appear in Figure 4.8 and Figure 4.9.

In all these figures, the opening trigger to the MOSFET is applied at 10 ms, and the closing trigger is applied at 110 ms along the time axis.

In Figure 4.8, the trajectories of three masses, x_1, x_2, and x_3, are represented by a blue solid curve, a green dotted curve, and a red dash-dotted curve, respectively. The velocities for the three masses, v_1, v_2, and v_3 are also presented in Figure 4.9.

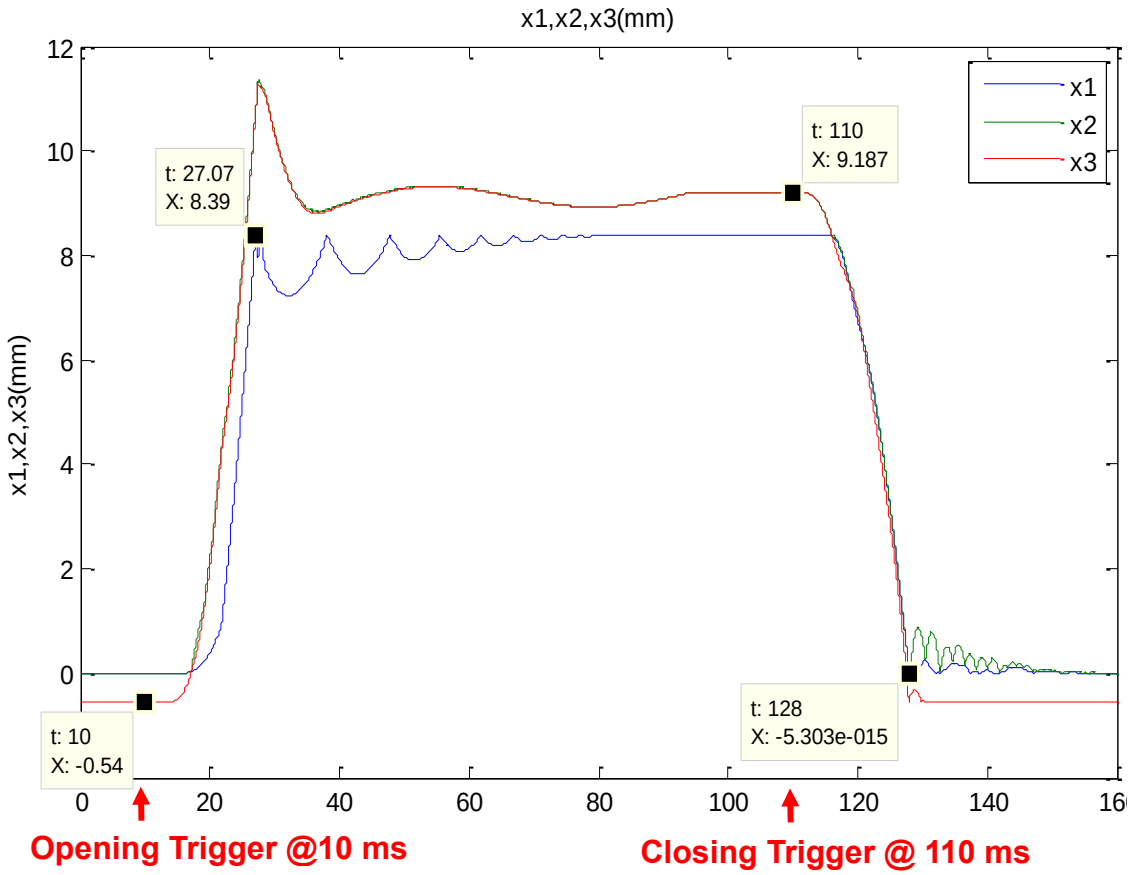

Figure 4.8 Recloser simulation results (the trajectories).

It is observed in Figure 4.8 and the third subplot of Figure 4.9 that since the current is increasing from zero, at the very beginning it is not large enough to balance the PM effect

on m_3 and reduce F_{mag3} substantially (as shown in equation (4.16)); thus, the plunger m_3 remains stationary until the time equals 14 ms.

It also shows in Figure 4.8 that right after 14 ms, the plunger m_3 is moving all by itself due to the significantly reduced electromagnetic force F_{mag3}, while the other two objects, the opening contact m_1 and the shaft m_2, almost remain at their initial positions. It is not until m_3 collides with m_2 at 17 ms, will m_1 and m_2 start to move individually.

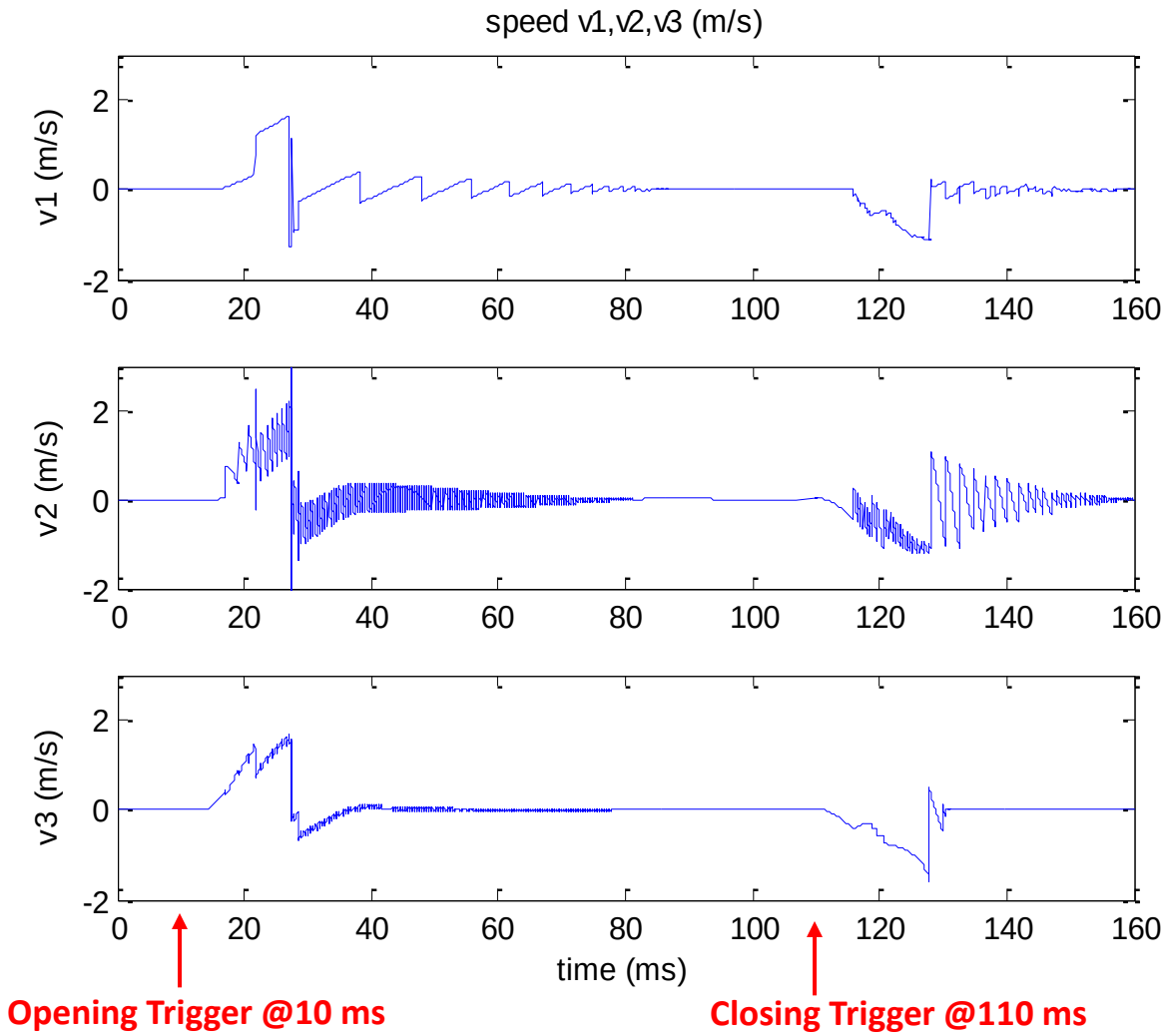

Figure 4.9 Recloser simulation results (the velocities).

Note that the plunger m_3 picks up the shaft m_2 fast but not m_1, and m_2 always follows and oscillates around m_3 during the whole process. This is because m_2 is a much smaller mass compared to m_1, and there are numerous collisions of type A (A1 and A2) between m_2 and m_3. Although m_1 is a relatively large mass, it moves slowly at first, after the shaft m_2 collides with m_1 for a few times, the kinetic energy transferred from m_3 to m_2, is eventually transferred to the opening m_1, due to collision B.

At 27.07 ms, m_1 hits the end plate and remains at the maximum stroke after several bounces, while m_2 and m_3 get closer and closer, and then start to move together oscillating around the steady-state open position at 9.187 mm. This oscillation eventually dampens out over time, due to the energy loss caused by the four types of inelastic collision, governed by equations (4.20) – (4.24).

The closing process proceeds in a similar manner.

In addition, Figure 4.9 more clearly demonstrates that the developed recloser simulation tool correctly models the discontinuous features of the moving components (governed by the collisions A, B (B'), C and D) very well, since the velocity curves for all three masses are highly-distorted waveforms with numerous sudden jumps and oscillations.

Furthermore, since the shaft m_2 is a much smaller mass compared to the opening contact m_1 and the plunger m_3, the speed oscillation for m_2 is much more significant than those of the opening contact m_1 and plunger m_3, as anticipated.

This figure also illustrates that since m_2 always follows and oscillates around m_3 as shown in Figure 4.8, the velocities for m_2 and m_3 agree with each other closely during the

entire opening and closing process, except that the m_2 curve has more high-frequency components.

4.4 CHAPTER SUMMARY

This chapter presents the detailed mathematical modeling work to describe the transient mechanical and electromagnetic performances of the vacuum automatic recloser system (a typical linear-motion energy conversion device with active DC excitation) during the opening and closing movements. A non-linear discontinuous eighth-order dynamic system is derived and a parameterized recloser modelling tool is developed using Matlab/Simulink.

The detailed simulation results will be compared to and validate by high-speed video camera measurement in the next chapter. This proposed modeling work can be used to improve the design scheme and optimize the capital and production cost without degrading the dynamic performance. It can also be integrated with other power-system simulation tools and assist the coordination of the recloser with other protection devices.

CHAPTER 5 VALIDATION AND IMPLEMENTATION OF RECLOSER-MODELING WORK

5.1 INTRODUCTION

The previous chapter introduces the detailed modeling work to describe the dynamic response of the vacuum automatic recloser during the opening and closing processes. In this chapter, the modeling work is fully validated by a full-size recloser test rig, and an example of design applications is further presented to demonstrate how the developed simulation modelling tool can be used to optimize capital and production costs without degrading performance [65, 66].

In section 5.2, the setup of the recloser test rig is explained in details. A high-speed video camera is used to record the two-way motion of the recloser, and an automated-image-tracking technique is implemented to generate data plots of the positions of the various recloser moving components over time, the opening contact (m_1), the shaft (m_2) and the plunger (m_3).

Section 5.3 presents the detailed comparison results and explanation between the model simulation data and the hardware test data for both the steady-state response and transient response of all the moving components, so as to validate the developed recloser simulation model.

Section 5.4 demonstrates how the verified parameterized analytical modelling tool can be used to provide an improved recloser design and reduce production costs.

Section 5.5 summarizes the chapter.

5.2 EXPERIMENTAL SETUP

The modeling effort for the complete electromagnetic-mechanical recloser system is validated by comparing the simulated results with measurements on a full-size recloser test rig in a laboratory setting. The general block diagram of the test setup appears in Figure 5.1.

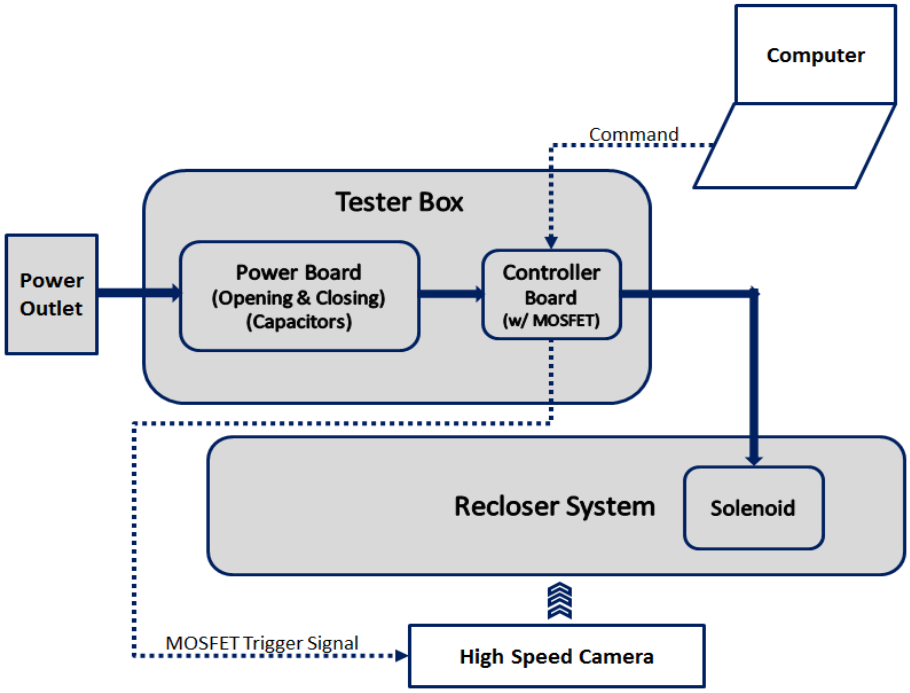

Figure 5.1 Recloser test rig setup.

The tester box is plugged into a 120-V power outlet. It contains a power storage unit (opening and closing capacitors), a controller board (with a MOSFET switch), and is eventually connected to the solenoid inside the solenoid case, as shown in Figure 5.1.

The opening and closing commands are provided by the computer via serial communication to the controller board in the tester box.

The two-way motion of the opening contact (m_1), shaft (m_2) and plunger (m_3) are recorded using a Phantom V73 high-speed video camera, which is synchronized with the MOSFET trigger signal. This video camera is capable of a frame rate of 6600 pictures/second, and the maximum resolution is 600X800 pixels/frame.

The video data is then processed by a self-developed automated image tracking software which uses a normalized pixel to pixel difference algorithm in Matlab to generate data plots of the positions of the recloser moving components (m_1, m_2 and m_3.) over time.

A sequence of tests is recorded using a wide field of view, capable of recording all three masses simultaneously. This sequence is then repeated by a series of tests recorded using a very narrow or zoomed field of view, centered around one end of the opening contact m_1 to maximize the available pixel resolution.

The pictures with a wide field of view are taken with pixel dither 0.265 mm, while the pictures with a narrow field (zoomed) of view are taken with pixel dither reduced to 0.1182 mm. With the reduced pixel dither, the trajectory of the opening contact, m_1, is more accurate, and thus the zoomed tests are used to scale the *pixel to mm conversion ratio* for the wide field of view tests to obtain more accurate trajectories of the other two masses, the shaft m_2 and the plunger m_3.

5.3 COMPARISON AND VALIDATION

The final scaled experimental results are shown in Figure 5.2. The trajectories of m_1, m_2 and m_3 are illustrated with the blue, green and red curves respectively. Since the

camera recording is synchronized with the trigger signal, the time t = 0 ms is exactly when the MOSFET is triggered by the microcontroller. The recording time for each video is 45 ms.

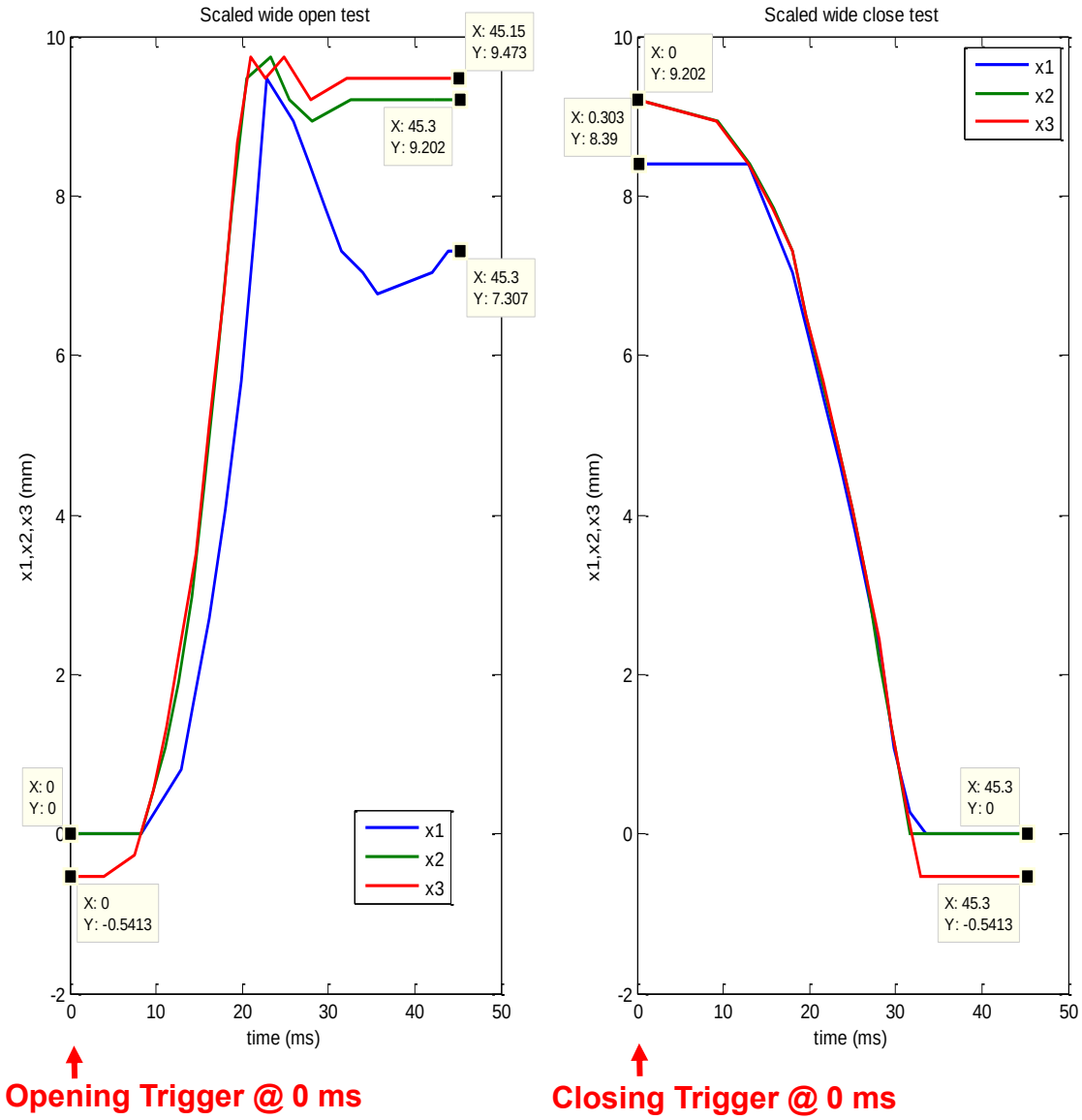

Figure 5.2 Recloser experimental results.

5.3.2 Steady-state comparison

It is observed from Figure 5.2 that at the end of the recording for the opening process, the three masses have not reached the complete steady state, especially for the moving contact m_1; hence the steady-state open positions should be the values measured at the initial condition of the closing process, instead of the end points of the opening process.

Comparing Figure 4.8 and Figure 5.2, it is observed that the simulated steady-state positions for all three masses during the round-trip process match closely with the experimental data, listed in Table 5.1.

Table 5.1 Steady-state recloser comparison results

		Experiment (mm)	Simulation (mm)
m_1	Closed steady state position	0	0
	Open steady state position	8.39	8.39
m_2	Closed steady state position	0	0
	Open steady state position	9.2	9.187
m_3	Closed steady state position	-0.54	-0.54
	Open steady state position	9.2	9.187

In particular, the open steady-state position for the moving contact m_1 is 8.39 mm in the simulation and test cases. The open steady-state positions for the shaft m_2 and plunger m_3 are both 9.187 mm in the simulation, while the test gives a value of 9.2 mm. Both the

simulation and test data indicates that m_2 and m_3 stop in the middle of the *slot 1* with a negligibly small error of 0.013 mm.

Therefore, it is validated by the high-speed video camera data that the developed recloser simulation model can provides accurate steady-state position results with negligibly small error.

5.3.3 Dynamic-response comparison

By observing the transient response of the simulation (in Figure 4.8) and the test results (in Figure 5.2) in more detail, it is furthermore concluded that the general dynamical sequence in both cases match well. That is,

1) Opening process:

STEP 1: The solenoid current is not large enough to balance the PM effect and the plunger m_3 does not move.

STEP 2: the plunger m_3 starts to move alone.

STEP 3: the plunger m_3 collides with the shaft m_2; the opening contact m_1 and shaft m_2 start to move separately as well.

STEP 4: the opening contact m_1 hits the end plate, compresses the end plate and bounces several times, until it rests at the maximum stroke; while the shaft m_2 and plunger m_3 get closer and closer, and eventually move together around the steady-state open position, until the oscillation dampens out over time.

2) Closing process:

STEP 1: the current increases to help the PM to move the shaft m_2 and plunger m_3 together.

STEP 2: As soon as the shaft m_2 collides with the moving contact m_1, m_1 starts to move, and m_2 separates from the plunger m_3. All the masses are moving separately.

STEP 3: All three masses stop at the closed condition after numerous bounces.

Note that unlike the simulation curves in Figure 4.8, the bouncing effect is not clearly shown in the experiment results, since most of the bounces are within 1 pixel error.

The detailed comparison of the trajectory of components m_1, m_2 and m_3 is shown in Figure 5.3, where the opening trigger is applied at 10 ms and the closing trigger signal at 110 ms. The blue dotted curves represents the simulated trajectories, while the red solid curves are always the experimental results.

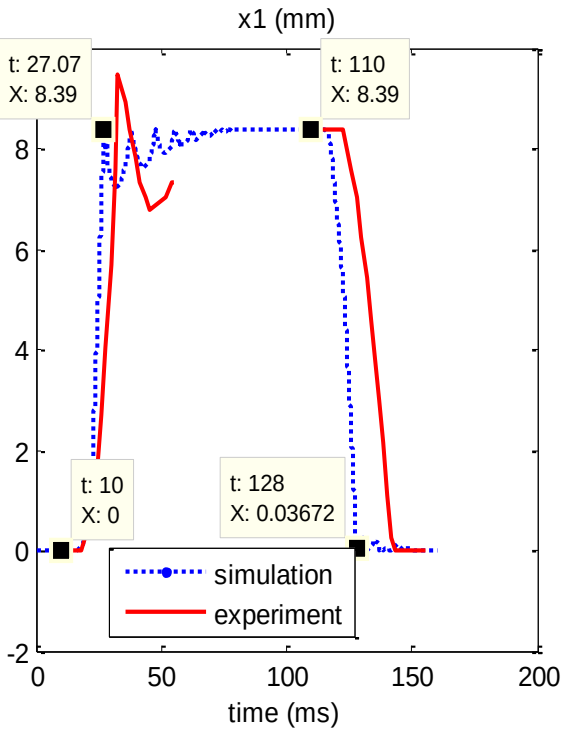

(a) The comparison of the trajectories for the opening contact m_1.

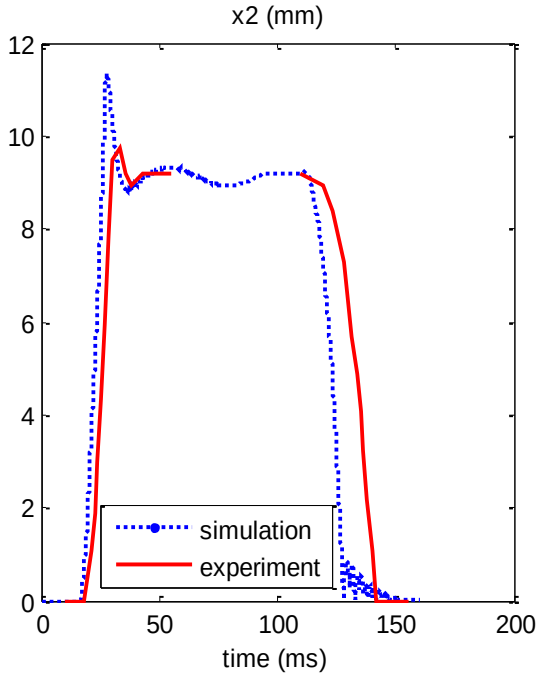

(b) The comparison of the trajectories for the shaft m_2.

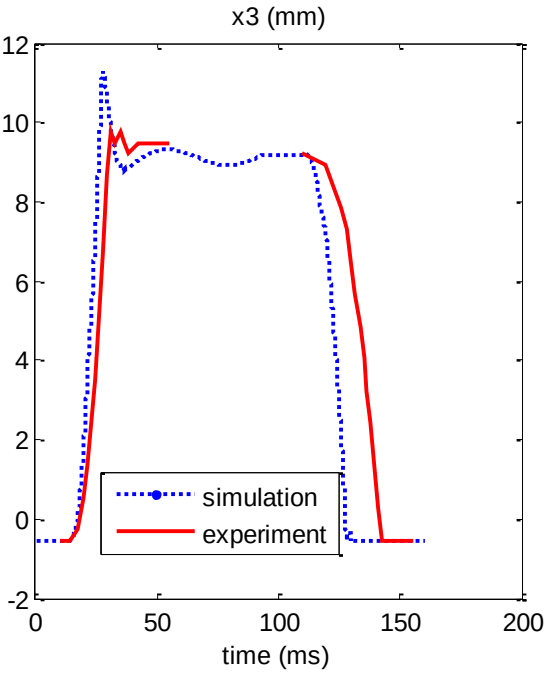

(c) The comparison of the trajectories for the plunger m_3.

Figure 5.3 Comparison of recloser simulation and experiment results

For the opening process, the simulation results closely match the measured data. Figure 5.3(a) shows that it takes 17.07 ms for the moving contact m_1 to reach the final steady state X_{1m} = 8.39 mm, while the actual value from the experiment is 20 ms. Generally speaking, the simulation results always lead the experimental curves and the simulated overshoots are always larger than the actual trajectories, because the mechanical loss, including friction and windage, is neglected in the modeling.

Furthermore, Figure 5.3(a) shows that the maximum position for the opening contact m_1 in the measured data is about 9 mm, which is greater than the steady state result of 8.39 mm. This is because the end plate of the vacuum interrupter is not a non-deformation surface, but consists of some soft material like rubber, so as to reduce the bouncing impact on the end plate; besides, it is directly observed from the video that the vacuum bottle itself deforms when the moving contact hits the end plate. These two deformation effects mentioned above result in the actual maximum stroke of the moving contact exceeding even the range of the specified value in the datasheet, 7+/-1 mm. Practically, it is too difficult to model this deformation effect mathematically; therefore in the simulation, the moving contact is always limited by the fixed maximum steady state stroke of 8.39 mm, and there is no overshoot, compared with the measured data.

On the other hand, the simulated closing-motion results do not match the measured results as well as the opening process. Aside from the neglected mechanical loss, an additional crucial factor contributing to the inconsistency is the saturation effect in the solenoid core material. In the simplified model of the magnetic path around the solenoid in the previous chapter, the permeability of the magnetic steel is assumed to be infinity, which is a valid assumption as long as there is no saturation in the magnetic material. The

physical explanation for this is that when opening, the solenoid opposes the PM effect and reduces the flux; however, during the closing process the solenoid adds to the PM effect and thus increases the flux density. The magnetic path steel is therefore more saturated during the closing process than during the opening process, and the reluctance R_{ex} should become larger than the value specified for opening.

Considering the average saturation effect for the closing process and representing part of the friction loss by additional copper loss in the solenoid coil, the model is modified and the new modified simulation results are compared with the measured results in Figure 5.4.

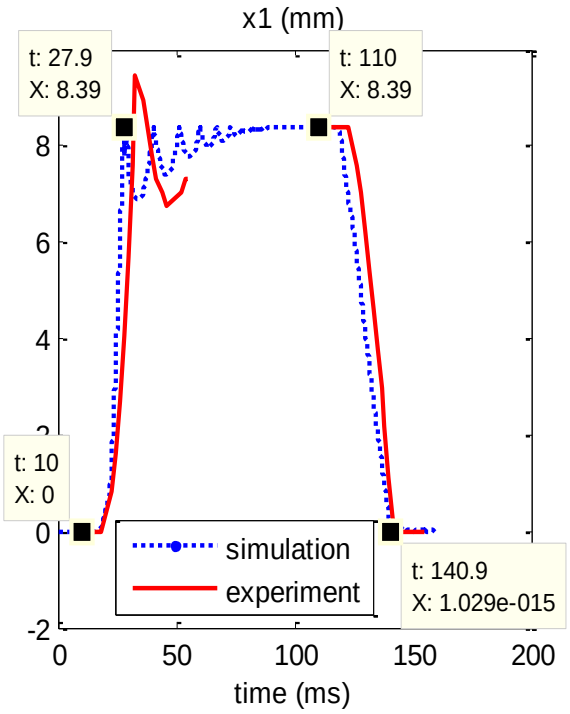

(a) The comparison of the trajectories for the opening contact m_1.

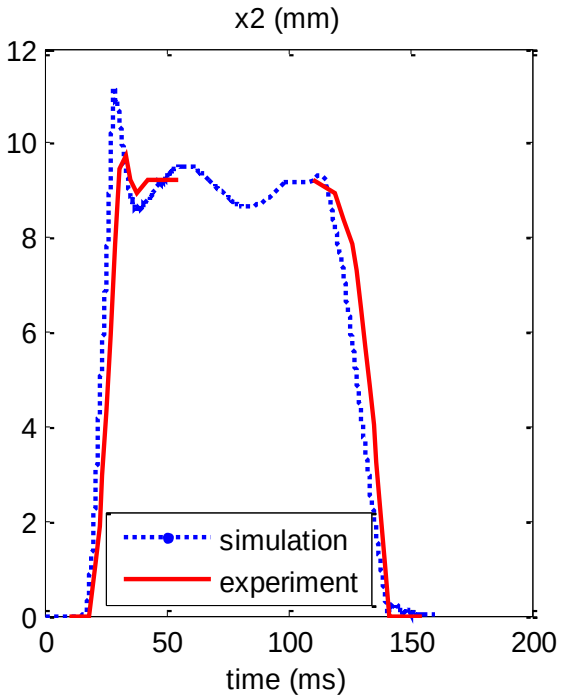

(b) The comparison of the trajectories for the shaft m_2.

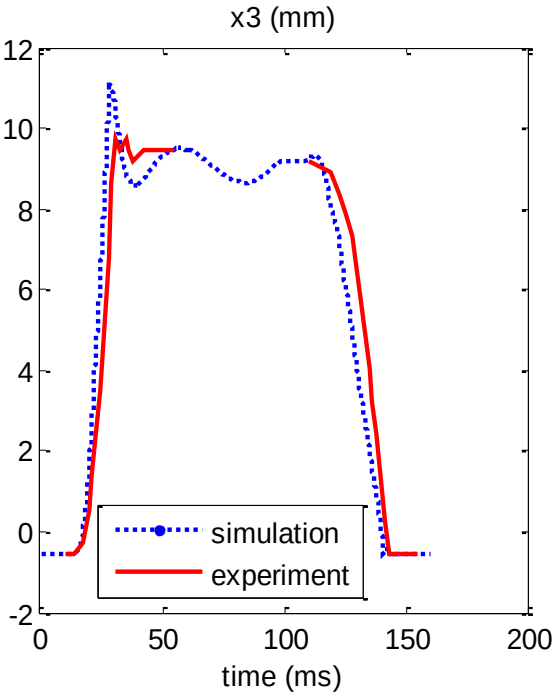

(c) The comparison of the trajectories for the plunger m_3.

Figure 5.4 Comparison of recloser simulation and experiment results, considering saturation effect and mechanical loss.

The two sets of trajectory results now agree more closely than in Figure 5.3. In particular, the simulated opening time for the moving contact m_1 now becomes 17.9 ms, only 2.1 ms less than the measured value, while the new simulated closing time is 30.9 ms, only 1.1 ms less than the measured hardware test data.

Other factors contributing to the difference between the simulated and measured results are the effects of non-linear spring stiffness, varying air-pressure force, and deformation of materials.

Note that, for industry application, the time interval between each pair of opening and closing trigger signals is much larger (more like 2000 ms) than the 100 ms used in these tests and the requirement for the closing response is therefore not as strict as for the opening process. It will be acceptable in practice if the closing difference is to be within a tolerable band of say 1% of the 2000 ms, which is 20 ms and the results of all these tests satisfy this requirement.

5.4 PRELIMINARY DESIGN IMPLEMENTATION

With the mathematical model validated by measurement in section 5.3, the effect of the variation of different parameters can now be explored for future optimized and improved design implementation.

All the input design parameters used for the validation above, like the geometry dimension, mass, capacitor voltage and PM bar remanence, as well as the corresponding simulation results define the *nominal* case in this section.

For example, reducing the PM remanence leads to a reduction in the breaking magnetic force, thus the opening time for the contact m_1 decreases, while the closing time increases. On the other hand, an increase (decrease) of the capacitor voltage for the

opening capacitor assists (hinders) the opening process; and obviously has no effect on the closing process. Similarly, the effect of the closing capacitor voltage is only seen in the closing process.

For purposes of illustration, assume that the original nominal PM material, is replaced by another magnet that is weaker, but much cheaper; then the total manufacturing cost will be reduced. This weaker magnet with a lower remanence B_r will help to open the recloser much faster; but it will take longer time to close, and may not even fully close if the remanence is too low. This side effect during the closing process can be well compensated for by increasing the initial electric energy stored in the closing capacitor, that is, increasing either the voltage or the capacitance for the closing capacitor. The concept is illustrated and validated in Figure 5.5.

In Figure 5.5, the remanence for the PM disk is reduced to 90% of the original value. It is observed that the recloser contact opens much faster, but takes an extra 5 ms to close. In order to regain a faster closing response, V_{close} is increased to 128% of the nominal value while the B_r is kept at the lower 90%. With this compensation in V_{close}, the opening time for m_1 is reduced as anticipated, but the closing time is restored to the same nominal value as before.

The blue dash-dotted curve in Figure 5.5 is the nominal curve; the red dotted curve is when only B_r is reduced but the coil voltages remain at their nominal values, and the green solid curve is the result of a reduced B_r but with the increased closing capacitor voltage. Since the change of the voltage on the closing capacitor V_{close} will not affect the opening mechanism, the red dotted and green solid curves coincide for the entire opening process.

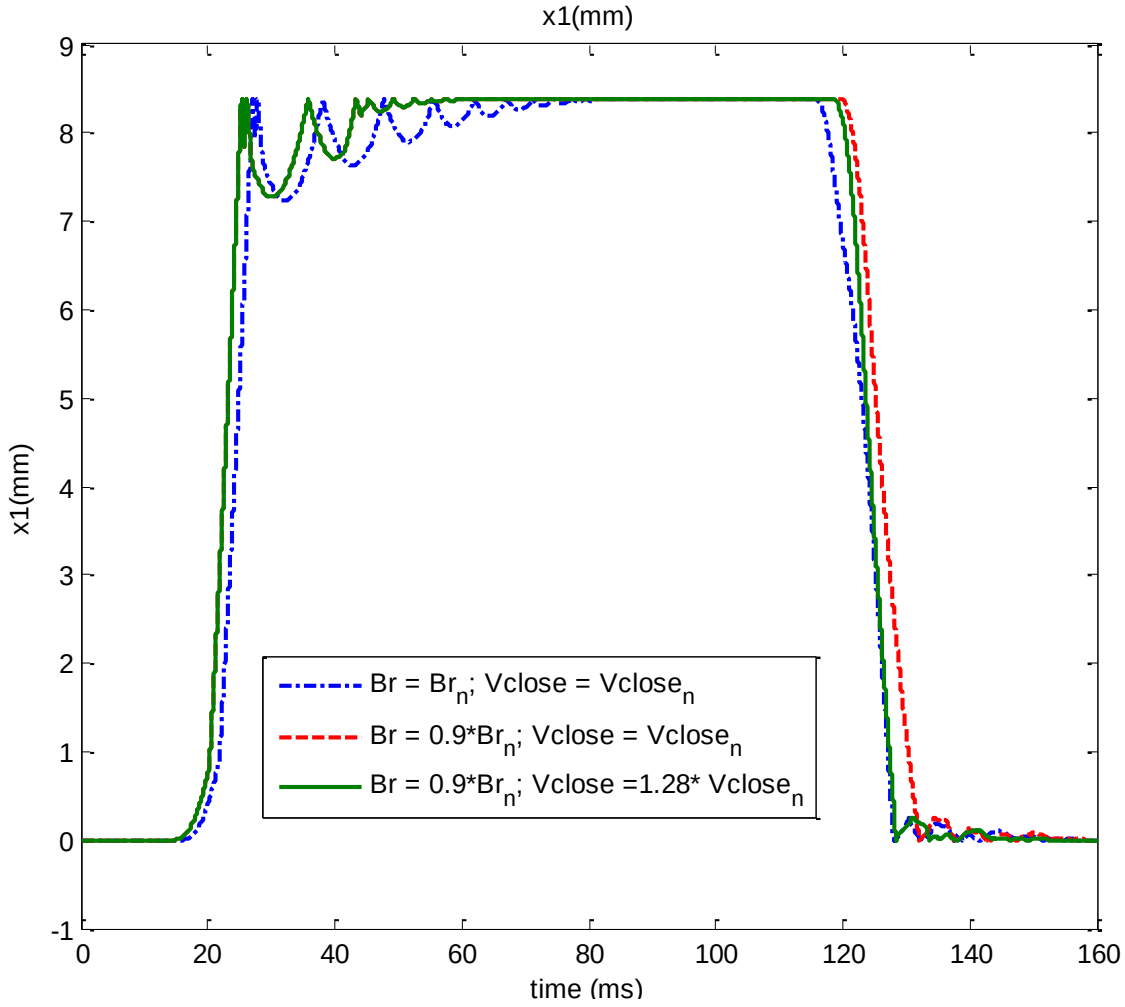

Figure 5.5 One possible recloser new design: combination of B_r and V_{close}

This illustration only considers the key recloser design parameters, capacitor voltages and PM remanence to enhance the opening and closing performance while reduce the system's cost. A more detailed optimal design process will be carried out in future work using various stochastic optimization methods, where more design parameters, like geometric dimension, mass, and spring stiffness, will also be considered with detailed material cost values.

5.5 CHAPTER SUMMARY

This chapter introduces the setup of a full-size recloser test rig in a laboratory setting. The high-speed video camera measurement data is used to validate the transient performance of the developed non-linear discontinuous dynamic model for the vacuum automatic recloser system, a typical linear-motion energy conversion system with active DC excitation.

It is further demonstrated that the developed parameterized recloser model can be implemented to provide an improved design approach, where the system production cost is reduced without degrading the performance.

CHAPTER 6 ANALYSIS OF A DIRECT-TORQUE-CONTROLLED IM WITH ACTIVE DC INJECTION

6.1 INTRODUCTION

The analysis of the two-way motion of an automatic vacuum recloser device (a typical linear-motion energy-conversion system) under active DC excitation is presented in the previous two chapters.

From Chapter 6 onwards, the analysis is moved onto the dynamics of an inverter-fed closed-loop-controlled induction motor (IM) (a typical rotary-motion energy-conversion system) under active DC excitation. The developed DC IM model provides practical means to excite a proper amount of DC current directly or indirectly into IM stator windings via different closed-loop motor-control algorithms. The proposed DC injection models will lead to a remote, simple, low-cost, accurate and non-invasive thermal-monitoring scheme for closed-loop-controlled IMs, so as to protect the motor from overheating, insulation degradation, and improve the over system's control performance [69-71].

In particular, Chapter 6 introduces the analysis of a direct-torque-controlled (DTC) IM under active DC excitation. Section 6.2 presents the DC motor models describing dynamic behavior of a DTC induction machine (IM) under active DC excitation. The analysis is based on the well-known *dq*-axis dynamic IM models, and takes advantages of the characteristics of DTC algorithm.

In section 6.3, the DC motor model is further simplified for practical implementation. Two active injection methods are proposed: flux-linkage-injection method and torque-injection method. The proposed two methods guarantee a proper amount of DC currents

indirectly and effectively excited in the motor stator windings for a DTC drive. In addition, the proposed methods are easy to implement: it requires no knowledge of the motor parameters and operating condition.

Sections 6.4 validate the proposed signal-injection methods for a standard DTC IM drive system, and quantitatively prove that the actual excited DC currents agree well with the theoretical values obtained from the DC IM model in section 6.2. The proposed injection method will finally be used for online thermal monitoring purposes, which will be presented in Chapter 8 .

Section 6.5 summarizes the chapter.

6.2 DC-INJECTION MODELING WORK

6.2.1 General analysis of DC injection for DTC IMs

As introduced in Chapter 3 , DTC algorithm was first proposed by Isao Nakahashi and Toshikiko Noguchi in the middle of 1980's [54]. This approach provides direct, accurate and fast-dynamic control for the motor electromagnetic torque and flux linkages [14].

The control block diagram for a typical DTC IM is shown in Figure 6.1 [54], where DTC scheme is implemented in the stationary *dq* reference frame (superscript *s* indicates the analysis is carried out in the stationary *dq* frame). Conventionally, the stator flux linkages $\left(\psi_{sd}^{s}, \psi_{sq}^{s}\right)^{T}$ is estimated from the stator voltages $\left(u_{sd}^{s}, u_{sq}^{s}\right)^{T}$ and stator currents $\left(i_{sd}^{s}, i_{sq}^{s}\right)^{T}$; while the electromagnetic torque T_{em} is obtained from the already estimated $\left(\psi_{sd}^{s}, \psi_{sq}^{s}\right)^{T}$ and directly-measured currents $\left(i_{sd}^{s}, i_{sq}^{s}\right)^{T}$. With the predetermined electromagnetic-torque reference $T_{em,ref}$ (or obtained from the regulator in the outer

speed loop with a command $\omega_{m,ref}$) and stator-flux-linkage magnitude reference $\Psi_{s,mag,ref}$, a DTC switching table is utilized to generate the duty ratio commands to the three-phase two-level power inverter system, so as to regulate the flux linkages and electromagnetic torque.

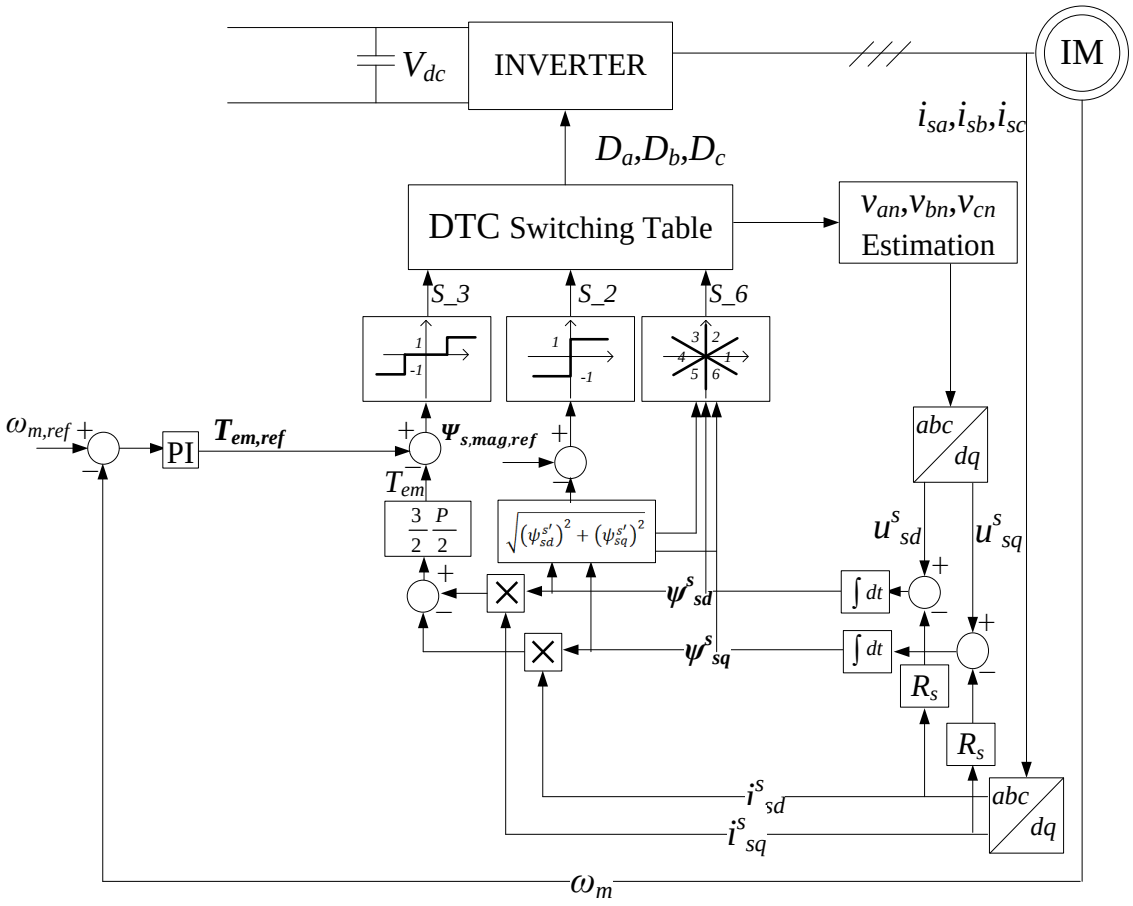

Figure 6.1 Block diagram for DTC scheme.

To excite a proper amount of DC current into an IM at a given operating condition, only the set of controllable variables in a typical DTC algorithm can be modified, namely,

the duty-cycle commands D_a, D_b, and D_c, the torque command $T_{em,ref}$, and the flux-linkage commands.

For IMs with a DTC scheme, modifying the duty-cycle command is not an effective way to excite the DC-current offset. This is because the duty-cycle commands D_a, D_b, and D_c are the outputs of flux-linkage and torque regulators, as shown in Figure 6.1 [54]; therefore, any change made in D_a, D_b, and D_c will be quickly cancelled out by the feedback-control mechanisms of high-bandwidth flux-linkage loop and torque loop.

The above analysis indicates that the stator-current DC components can only be effectively excited by injecting an equivalent flux-linkage-bias command $\left(\Delta\Psi^s_{sd,ref}, \Delta\Psi^s_{sq,ref}\right)^T$ or a torque-change command $\Delta T_{em,ref}$ at the inputs of the two inner control loops, as shown in red in Figure 6.2.

In all, to properly excite some amount of DC currents into a DTC motor drive system, the primary challenge is to carry out a small-signal analysis of the changes of all machine variables during the active DC-injection period, and derive a quantitative relationship between the desired DC-current offset $\left(\Delta i^s_{sd}, \Delta i^s_{sq}\right)^T$, the corresponding flux-linkage biases $\left(\Delta\psi^s_{sd}, \Delta\psi^s_{sq}\right)^T$ and the torque change ΔT_{em}.

The complete analysis is shown as follows.

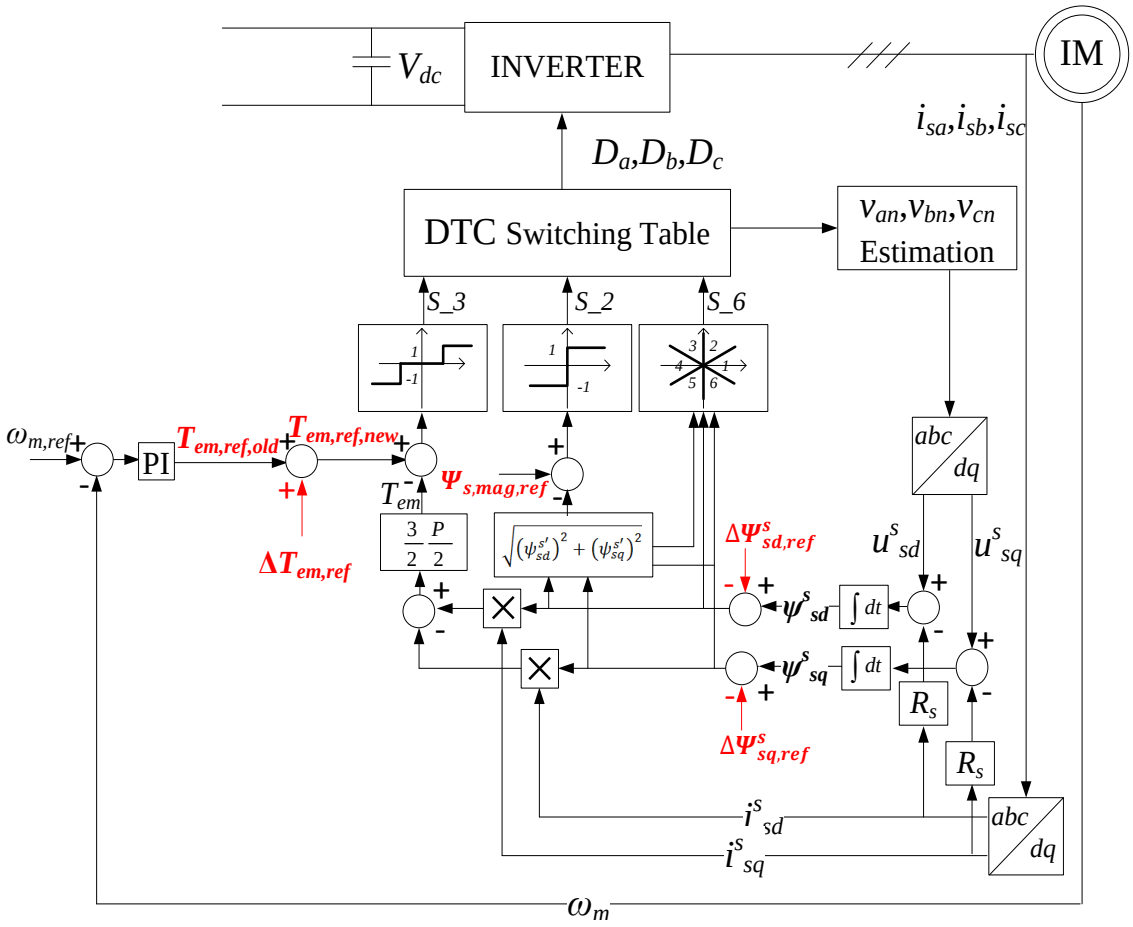

Figure 6.2 Block diagram for DTC scheme, with injection signals.

6.2.2 The modified DTC IM dynamic model

In the stationary *dq* reference frame, the complete mathematical model for a squirrel-cage IM (with a floating neutral point) under normal operation conditions is shown in equations (6.1) – (6.3), where ψ, u, and i represent the flux-linkage, voltage and current quantities; L_s, L_m, and L_r are the stator, mutual, and rotor inductances; R_s and R_r are the stator and rotor resistances; ω_m is the mechanical speed in rad/s; P represents the number

of poles in the motor; T_l is the load torque; B is the frication coefficient; p is the differential operator; subscript s represents the stator quantities; subscript d (or q) indicates the quantities in d (or q)-axis respectively.

$$\begin{cases} u_{sd}^s = R_s i_{sd}^s + p\psi_{sd}^s \\ u_{sq} = R_s i_{sq}^s + p\psi_{sq}^s \\ 0 = R_r i_{rd}^s + p\psi_{rd}^s - (0 - \omega_m)\frac{P}{2}\psi_{rq}^s \\ 0 = R_r i_{rq}^s + p\psi_{rq}^s + (0 - \omega_m)\frac{P}{2}\psi_{rd}^s \end{cases}, \tag{6.1}$$

$$\begin{cases} \psi_{sd}^s = L_s i_{sd}^s + L_m i_{rd}^s \\ \psi_{sq}^s = L_s i_{sq}^s + L_m i_{rq}^s \\ \psi_{rd}^s = L_m i_{sd}^s + L_r i_{rd}^s \\ \psi_{rq}^s = L_m i_{sq}^s + L_r i_{rq}^s \end{cases}, \tag{6.2}$$

$$\begin{cases} T_{em} = \frac{3}{2}\frac{P}{2}\left(\psi_{sd}^s i_{sq}^s - \psi_{sq}^s i_{sd}^s\right) \\ p\omega_m = \frac{T_{em} - T_l - B\omega_m}{J} \end{cases}. \tag{6.3}$$

In a typical DTC scheme, only the stator-side variables $i_{sd}^s, i_{sq}^s, \psi_{sd}^s$ and ψ_{sq}^s are already measured or estimated, while the rotor-side variables are not directly available, as shown in Figure 6.1. Hence the original flux linkage model in equation (6.2) has to be modified, such that the rotor quantities $\psi_{rd}^s, \psi_{rq}^s, i_{rd}^s$ and i_{rq}^s are rewritten in terms of the stator quantities, as indicated in equation (6.4), where σ is the leakage factor and is defined at the end of equation (6.4).

$$\begin{cases} i_{rd}^s = \frac{\psi_{sd}^s - L_s i_{sd}^s}{L_m} \\ i_{rq} = \frac{\psi_{sq}^s - L_s i_{sq}^s}{L_m} \\ \psi_{rd}^s = \frac{L_r}{L_m}(\psi_{sd}^s - \sigma L_s i_{sd}^s) \\ \psi_{rq}^s = \frac{L_r}{L_m}(\psi_{sq}^s - \sigma L_s i_{sq}^s) \end{cases}, \quad \text{where } \sigma = 1 - \frac{{L_m}^2}{L_s L_r}; \tag{6.4}$$

To sum up, equation sets (6.1), (6.4) and (6.3) describe the complete mathematical model for the squirrel-cage induction machine (with a floating neutral point) under normal operating condition, of which the flux-linkage model is particularly modified for DTC implementation.

6.2.3 The DC-injection model for DTC IMs

Assume after $t = t^*$, a DC-injection command is externally implemented as small changes $\left(\Delta\Psi^s_{sd,ref}, \Delta\Psi^s_{sq,ref}\right)^T$ or $\Delta T_{em,ref}$ into the control system; then, a small offsetting term (indicated by prefix Δ) appears in each machine variable. Among all the offsetting terms, the mechanical-speed change ω_m is relatively insignificant, due to the large inertia of the rotor and load. Hence, it is feasible to assume ω_m remains unchanged during the injection period. The corresponding equation sets which model the small changes of all IM electric variables appear as follows:

$$\begin{cases} \Delta u^s_{sd} = R_s \Delta i^s_{sd} + p(\Delta\psi^s_{sd}) \\ \Delta u^s_{sq} = R_s \Delta i^s_{sq} + p(\Delta\psi^s_{sq}) \\ 0 = R_r \Delta i^s_{rd} + p(\Delta\psi^s_{rd}) + \omega_m \frac{P}{2} \Delta\psi^s_{rq}, \\ 0 = R_r \Delta i^s_{rq} + p\left(\Delta\psi^s_{rq}\right) - \omega_m \frac{P}{2} \Delta\psi^s_{rd} \end{cases} \tag{6.5}$$

$$\begin{cases} \Delta i^s_{rd} = \frac{\Delta\psi^s_{sd} - L_s \Delta i^s_{sd}}{L_m} \\ \Delta i^s_{rq} = \frac{\Delta\psi^s_{sq} - L_s \Delta i^s_{sq}}{L_m} \\ \Delta\psi^s_{rd} = \frac{L_r}{L_m}(\Delta\psi^s_{sd} - \sigma L_s \Delta i^s_{sd}) \\ \Delta\psi^s_{rq} = \frac{L_r}{L_m}\left(\Delta\psi^s_{sq} - \sigma L_s \Delta i^s_{sq}\right) \end{cases}, \tag{6.6}$$

$$\Delta T_{em} = \frac{3}{2}\frac{P}{2}\left[\psi^s_{sd}\Delta i^s_{sq} - \psi^s_{sq}\Delta i^s_{sd} + \Delta\psi^s_{sd}\left(i^s_{sq} + \Delta i^s_{sq}\right) - \Delta\psi^s_{sq}\left(i^s_{sd} + \Delta i^s_{sd}\right)\right]. \tag{6.7}$$

The model above describes the dynamic response of the changes of all IM electric variables caused by the DC excitation. Note that the rotor resistance R_r in the injection model analysis is increased from the rated value, due to the skin effect.

However, this model includes all stator-side and rotor-side motor parameters. Therefore, it is unclear how the desired stator-current biases $\left(\Delta i_{sd}^{s}, \Delta i_{sq}^{s}\right)^{T}$ are directly related to the other controllable quantities, $\left(\Delta\psi_{sd}^{s}, \Delta\psi_{sq}^{s}\right)^{T}$ and ΔT_{em}; thus, the model does not help to excite the desired DC-current offset in a typical DTC drive system.

To solve the mentioned problem, a further derivation is carried out.

Substituting equation set (6.6) back into the third and fourth rows in equation set (6.5) eliminates the rotor-side variables in the rotor-voltage equations, and results in the following analytical expression purely among the stator variables, the stator-current offset $\left(\Delta i_{sd}^{s}, \Delta i_{sq}^{s}\right)^{T}$ and the flux-linkage bias $\left(\Delta\psi_{sd}^{s}, \Delta\psi_{sq}^{s}\right)^{T}$, as shown in equation (6.8). It is more clearly expressed in equation (6.9).

$$\begin{cases} 0 = R_r \frac{\Delta\psi_{sd}^{s} - L_s \Delta i_{sd}^{s}}{L_m} + \frac{L_r}{L_m} p\left(\Delta\psi_{sd}^{s} - \sigma L_s \Delta i_{sd}^{s}\right) + \omega_m \frac{P}{2} \frac{L_r}{L_m} \left(\Delta\psi_{sq}^{s} - \sigma L_s \Delta i_{sq}^{s}\right) \\ 0 = R_r \frac{\Delta\psi_{sq}^{s} - L_s \Delta i_{sq}^{s}}{L_m} + \frac{L_r}{L_m} p\left(\Delta\psi_{sq}^{s} - \sigma L_s \Delta i_{sq}^{s}\right) - \omega_m \frac{P}{2} \frac{L_r}{L_m} \left(\Delta\psi_{sd}^{s} - \sigma L_s \Delta i_{sd}^{s}\right) \end{cases}, \tag{6.8}$$

$$-\sigma L_r L_s p \begin{bmatrix} \Delta i_{sd}^{s} \\ \Delta i_{sq}^{s} \end{bmatrix} + L_s \begin{bmatrix} -R_r & -\frac{P}{2}\sigma L_r \omega_m \\ \frac{P}{2}\sigma L_r \omega_m & -R_r \end{bmatrix} \begin{bmatrix} \Delta i_{sd}^{s} \\ \Delta i_{sq}^{s} \end{bmatrix} + \begin{bmatrix} R_r & \frac{P}{2} L_r \omega_m \\ -\frac{P}{2} L_r \omega_m & R_r \end{bmatrix} \begin{bmatrix} \Delta\psi_{sd}^{s} \\ \Delta\psi_{sq}^{s} \end{bmatrix} = 0. \tag{6.9}$$

Assume a DC stator-flux-linkage bias is injected as $\left(\Delta\psi_{sd}^{s}, \Delta\psi_{sq}^{s}\right)^{T} = \left(\Delta\Psi_{sd}^{s}, \Delta\Psi_{sq}^{s}\right)^{T}$, and then equation (6.9) becomes a first-order differential equation with respect to the stator-current change $\left(\Delta i_{sd}^{s}, \Delta i_{sq}^{s}\right)^{T}$. The complete response for the current change comprises of a decaying exponential term and a steady-state DC term. As time goes by,

the exponential term dies out, and only the DC component $\left(\Delta I_{sd}^{s}, \Delta I_{sq}^{s}\right)^{T}$ remains, determined by the following equation:

$$\begin{bmatrix} -R_r & -\frac{P}{2}\sigma L_r \omega_m \\ \frac{P}{2}\sigma L_r \omega_m & -R_r \end{bmatrix} L_s \begin{bmatrix} \Delta I_{sd}^{s} \\ \Delta I_{sq}^{s} \end{bmatrix} = \begin{bmatrix} -R_r & -\frac{P}{2} L_r \omega_m \\ \frac{P}{2} L_r \omega_m & -R_r \end{bmatrix} \begin{bmatrix} \Delta \Psi_{sd}^{s} \\ \Delta \Psi_{sq}^{s} \end{bmatrix}. \quad (6.10)$$

Moreover, with the known values for $\left(\Delta \Psi_{sd}^{s}, \Delta \Psi_{sq}^{s}\right)^{T}$ and $\left(\Delta I_{sd}^{s}, \Delta I_{sq}^{s}\right)^{T}$, the resultant torque ripple ΔT_{em} is calculated as follows:

$$\Delta T_{em} = \frac{3}{2}\frac{P}{2}\left[\psi_{sd}^{s}\Delta I_{sq}^{s} - \psi_{sq}^{s}\Delta I_{sd}^{s} + \Delta \Psi_{sd}^{s}\left(i_{sq}^{s} + \Delta I_{sq}^{s}\right) - \Delta \Psi_{sq}^{s}\left(i_{sd}^{s} + \Delta I_{sd}^{s}\right)\right]. \quad (6.11)$$

In summary, the derived quantitative relationship between the desired DC stator current offset and the corresponding changes in stator flux linkage and torque at steady state is presented in equations (6.10)-(6.11).

It is directly observed that at steady state, DC stator-flux linkages result in DC stator currents and additional torque ripple, of which the dominating component is varying at synchronous speed. Furthermore, combined with the flux-linkage model in equation (6.6), this conclusion can be extended as:

At steady state, DC stator-flux linkages produce not only DC stator current, but also DC rotor currents and DC rotor flux linkages; the resultant electromagnetic torque ripple is dominated by a sine component varying at synchronous speed.

The above DC-injection model analysis indicates the equivalent way to excite a DC current component in a DTC IM system is to inject the corresponding flux-linkage bias and torque ripple simultaneously, governed by the quantitative relationships in equations (6.10) and (6.11).

6.3 PROPOSED DC-INJECTION METHODS

As mentioned in section 6.2, theoretically, the DC-current offset $\left(\Delta I_{sd}^{s}, \Delta I_{sq}^{s}\right)^{T}$ should be excited via the injection of $\left(\Delta \Psi_{sd}^{s}, \Delta \Psi_{sq}^{s}\right)^{T}$ and ΔT_{em} simultaneously. However, the complicated relationships in equations (6.10)-(6.11) require accurate knowledge of motor parameters, including L_r, L_s and R_r, across the entire operating region, which are difficult to obtain in real life, especially for a VFD system.

On the other hand, if either the stator-flux-linkage bias or the torque ripple is injected, the resultant current change will not be a pure DC component, but may contain certain harmonics. However, it should be adequate. This is because the main application of the DC-injection method is to provide thermal monitoring via stator-resistance estimation; the accuracy of the resistance estimation only depends on the accuracy of the stator-current and stator-voltage estimations. As long as some level of DC signal is excited in the machine, the injection should be adequate for resistance estimation. The real challenge is how to implement a real-time signal-processing technique to guarantee the accuracy of DC-voltage and current extraction.

Based on the above reasoning, for practical implementation, it is unnecessary to inject torque ripple and flux-linkage bias simultaneously, and it is reasonable to simplify the DC-signal model. Two injection methods are proposed in this section: one is the flux-linkage-injection method with the command $\left(\Delta \Psi_{sd,ref}^{s}, \Delta \Psi_{sq,ref}^{s}\right)^{T}$, and the other is the torque injection method with the command $\Delta T_{em,ref}$. Both methods are successfully validated by simulation and experimental results.

6.3.1 The flux-linkage-injection method

With this method, the external injection is only applied to the flux-control loop. In the conventional and standard DTC scheme, the circular locus of the stator-flux-linkage vector in the stationary *dq* frame is determined by the following expression [54]:

$$\psi_{sd}^{s\ 2} + \psi_{sq}^{s\ 2} = \Psi_{s,mag,ref}^2. \tag{6.12}$$

To inject the desired flux-linkage biases $\left(\Delta\Psi_{sd,ref}^s, \Delta\Psi_{sq,ref}^s\right)^T$ into the motor three-phase stator winding, the stator-flux-linkage equation should be modified, as shown below:

$$\left(\psi_{sd}^s - \Delta\Psi_{sd,ref}^s\right)^2 + \left(\psi_{sq}^s - \Delta\Psi_{sq,ref}^s\right)^2 = \Psi_{s,mag,ref}^2. \tag{6.13}$$

The locus of the stator-flux-linkage command appears in Figure 6.3, where the stator-flux-linkage vector $\overrightarrow{OA} = \overrightarrow{\psi_s^s} = \psi_{sd}^s + \psi_{sq}^s j$, and the stator-flux-linkage offset $\overrightarrow{OO'} = \overrightarrow{\Delta\Psi_{s,ref}} = \Delta\Psi_{sd,ref}^s + \Delta\Psi_{sq,ref}^s j$. With the desired flux-linkage bias $\overrightarrow{\Delta\Psi_{s,ref}}$, the center of the circular locus of the stator-flux-linkage vector $\overrightarrow{\psi_s^s}$ is shifted from the origin *O* (0, 0) to another point *O'* $(\Delta\Psi_{sd,ref}^s, \Delta\Psi_{sq,ref}^s)$.

To practically excite some level of DC-current offset, the equation above indicates a set of DC flux-linkage offset commands $\left(\Delta\Psi_{sd,ref}^s, \Delta\Psi_{sq,ref}^s\right)^T$ should be included in the inner flux-linkage control loop; no modification to the torque-control loop is required: $\Delta T_{em,ref} = 0$.

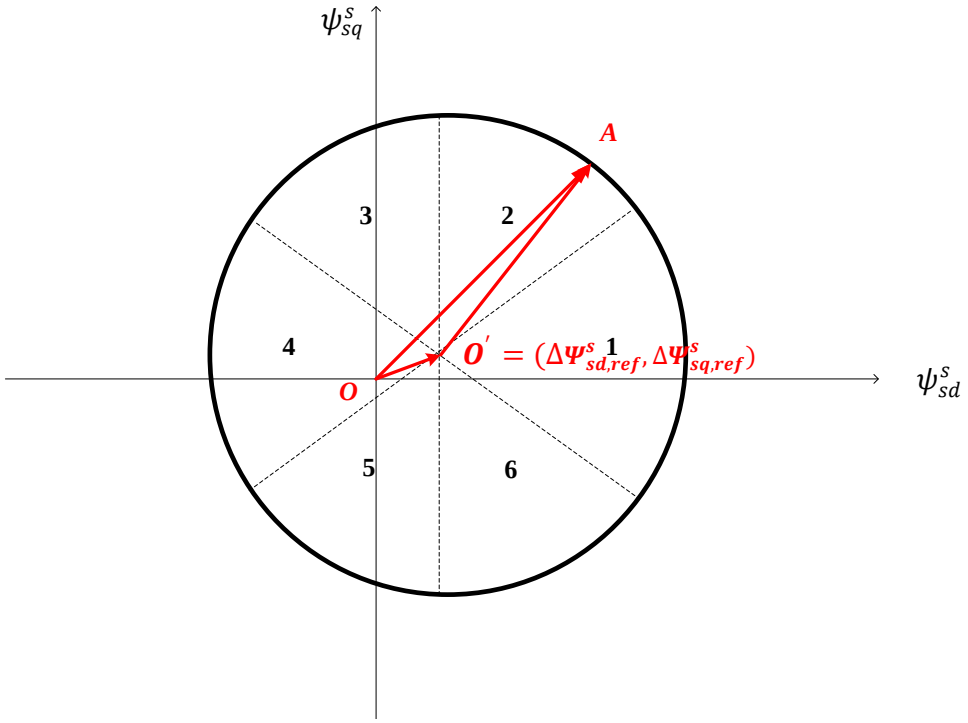

Figure 6.3 Locus of stator-flux-linkage vector, with flux-linkage injection.

6.3.2 The torque-injection method

With this method, the external injection is only applied to the torque-control loop. According to equation (6.11), even if only the torque ripple is externally injected, both the DC stator-flux-linkage offsets $\left(\Delta\Psi_{sd}^{s}, \Delta\Psi_{sq}^{s}\right)^{T}$ and DC stator-current offsets $\left(\Delta I_{sd}^{s}, \Delta I_{sq}^{s}\right)^{T}$ have to be chosen based on the complicated relationship in equation (6.10), so as to determine the amount of torque ripple. This complicated expression requires knowledge of several motor parameters within the entire operating range, including L_r, L_s and R_r.

However, the complexity can be avoided by simplifying the flux-linkage-injection and torque-injection expressions, so that the approximate torque-injection expression

only requires the knowledge of $\left(\Delta I_{sd}^{s}, \Delta I_{sq}^{s}\right)^{T}$, rather than both $\left(\Delta I_{sd}^{s}, \Delta I_{sq}^{s}\right)^{T}$ and $\left(\Delta \Psi_{sd}^{s}, \Delta \Psi_{sq}^{s}\right)^{T}$. Thus, there is no need to utilize the complicated relationship in equation (6.10), and the torque injection method is significantly simplified. The approximate expression is derived as follows.

With further manipulation, equation (6.10) is more clearly expressed as

$$\begin{bmatrix} \frac{\left(\frac{R_r}{X_r}\right)^2+\sigma}{\left(\frac{R_r}{X_r}\right)^2+1} & -\frac{\frac{R_r}{X_r}(1-\sigma)}{\left(\frac{R_r}{X_r}\right)^2+1} \\ \frac{\frac{R_r}{X_r}(1-\sigma)}{\left(\frac{R_r}{X_r}\right)^2+1} & \frac{\left(\frac{R_r}{X_r}\right)^2+\sigma}{\left(\frac{R_r}{X_r}\right)^2+1} \end{bmatrix} L_s \begin{bmatrix} \Delta I_{sd}^{s} \\ \Delta I_{sq}^{s} \end{bmatrix} = \begin{bmatrix} \Delta \Psi_{sd}^{s} \\ \Delta \Psi_{sq}^{s} \end{bmatrix}, \tag{6.14}$$

where $X_r = \frac{P}{2} L_r \omega_m$.

Considering $\left(\frac{R_r}{X_r}\right)^2 \ll 1$ during the normal speed operation, equation (6.14) can be further simplified as

$$\begin{bmatrix} \left(\frac{R_r}{X_r}\right)^2+\sigma & -\frac{R_r}{X_r}(1-\sigma) \\ \frac{R_r}{X_r}(1-\sigma) & \left(\frac{R_r}{X_r}\right)^2+\sigma \end{bmatrix} L_s \begin{bmatrix} \Delta I_{sd}^{s} \\ \Delta I_{sq}^{s} \end{bmatrix} \approx \begin{bmatrix} \Delta \Psi_{sd}^{s} \\ \Delta \Psi_{sq}^{s} \end{bmatrix}. \tag{6.15}$$

Due to the fact that $\sigma \ll 1$, the coefficient matrix on the left of equation (6.15) is extremely small; therefore, $\left(\Delta \Psi_{sd}^{s}, \Delta \Psi_{sq}^{s}\right)^{T}$ is negligible compared to $L_s\left(\Delta I_{sd}^{s}, \Delta I_{sq}^{s}\right)^{T}$.

This mechanism can also be physically explained as follows. As observed from the flux-linkage model in equation (6.2), at steady-state DC injection period, the total amount of the DC stator-flux-linkage offsets are determined by both the DC stator currents and the DC rotor currents. According to *Lenz's law*, most of the DC flux linkage offsets

produced by the DC stator currents will be cancelled out by the induced DC rotor current in the squirrel cage of the induction machine.

This mechanism can be conceptually illustrated by the following equation set, where the mutual flux linkages are affected by both the stator and rotor currents. According to *Lenz's law*, the mutual flux-linkage terms go to zero; therefore, the actual amount of stator-flux-linkage offsets in the stationary *dq* reference frame $\left(\Delta\Psi_{sd}^{s}, \Delta\Psi_{sq}^{s}\right)^{T}$ are approximately equal to the leakage inductance L_{ls} times the small current offsets $\left(\Delta I_{sd}^{s}, \Delta I_{sq}^{s}\right)^{T}$.

$$\left.\begin{aligned}\Delta\Psi_{sd}^{s} &= L_s\Delta I_{sd}^{s} + L_m\Delta I_{rd}^{s} = L_{ls}\Delta i_{sd}^{s} + L_m(\Delta i_{sd}^{s} + \Delta i_{rd}^{s}) \approx L_{ls}\Delta i_{sd}^{s}\\ \Delta\Psi_{sq}^{s} &= L_s\Delta I_{sq}^{s} + L_m\Delta I_{rq}^{s} = L_{ls}\Delta i_{sq}^{s} + L_m\left(\Delta i_{sq}^{s} + \Delta i_{rq}^{s}\right) \approx L_{ls}\Delta i_{sq}^{s}\end{aligned}\right\} \tag{6.16}$$

Hence, the above analysis indicates that the third and fourth terms in equation (6.11) are negligibly small compared to the first two terms, and the torque ripple is approximated as

$$\Delta T_{em} \approx \frac{3}{2}\frac{P}{2}[\psi_{sd}^{s}\Delta I_{sq}^{s} - \psi_{sq}^{s}\Delta I_{sd}^{s}]. \tag{6.17}$$

It is observed from equation (6.17) that this torque-injection expression requires only $\left(\Delta I_{sd}^{s}, \Delta I_{sq}^{s}\right)^{T}$, rather than both stator DC currents $\left(\Delta I_{sd}^{s}, \Delta I_{sq}^{s}\right)^{T}$ and stator flux linkages $\left(\Delta\Psi_{sd}^{s}, \Delta\Psi_{sq}^{s}\right)^{T}$. Therefore, there is no need to consider the exact and complicated relationship in equation (6.10), and the torque injection is significantly simplified as in equation (6.17).

To practically excite some level of DC-current offset, the equation (6.17) indicates a sine-wave torque-ripple command at synchronous speed should be added on the original torque reference $T_{em,ref}$; no modification for the flux-control loop is required.

6.3.3 General control block diagram

The schematic diagram of the proposed two methods implemented in a conventional DTC scheme is shown in Figure 6.2 in section 6.2.1.

When using the flux-linkage-injection method, $\Delta T_{em,ref}$ is set to zero; when using the torque-injection method, the flux-linkage bias vector $\overrightarrow{\Delta\Psi_{s,ref}} = \left(\Delta\Psi^{s}_{sd,ref}, \Delta\Psi^{s}_{sq,ref}\right)^{T}$ is forced to zero. The injection scheme is summarized in the table below.

Table 6.1 The proposed DC-injection scheme for DTC IMs

Flux-linkage injection method	Torque injection method
$\left(\Delta\Psi^{s}_{sd,ref}, \Delta\Psi^{s}_{sq,ref}\right)^{T}$	0
0	$\Delta T_{em,ref}$

For both methods, the commanded injection amount should be comparably small, so as to have negligible impact on the motor normal operating conditions and power dissipation. Furthermore, for hardware implementation, since the temperature varies slowly compared to the motor dynamics, the signal-injection method is superimposed intermittently to the motor drive system, say for a period of 20 seconds every 10 minutes. This also helps to reduce the resultant torque ripple and additional power loss.

It should be pointed out again that, in either of the two proposed methods, the measured small change quantities contain not only the excited DC components in stator currents and voltages as expected, but also some small but noticeable second–order

harmonics components, which indicates that the DC term is somehow distorted and the extracted DC components do not match whatever we specified initially.

This is because the injected command set $\begin{bmatrix} \Delta T_{em,ref} \\ \overrightarrow{\Delta \Psi_{s,ref}} \end{bmatrix}$ in either of the two proposed methods is practically simplified, and the command's relationship does not match the physics in equations (6.10) and (6.11) exactly. In addition, the actual excited signal will be partially compensated by the outer speed feedback-control loop, as shown in Figure 6.2, especially for the torque-injection approach.

6.4 METHOD VALIDATION

The derived quantitative relationship and the proposed DC-injection methods for DTC IMs are firstly validated by Matlab/Simulink simulation. The parameter set for the induction machine appears in Table 6.2.

Table 6.2 Parameter table of the induction machine (simulation)

Rated power	40 hp	Poles	4
Rated voltage	460 V	Rated current	52.41 A
Rated speed	1720 rpm	R_s	0.22Ω
R_r	0.209Ω	L_m	0.04 H
L_{ls}	0.0025 H	L_{lr}	0.003 H

At steady-state normal condition, the stator-flux-linkage magnitude is controlled at the rated value, roughly 0.96 Wb-turns; the torque is controlled to match the commanded

value, which directly obtained from the outer speed loop, with a speed reference around 1300 rpm.

In the simulation condition, the stator resistance R_s is kept constant, and the flux-linkage-injection/torque-injection method is applied to the IM after the motor reaches the steady-state under the DTC scheme. Once the injection transient also reaches the steady state, stable DC offsets for three-phase stator currents can be directly observed, so as to validate the feasibility of the proposed two injection methods.

Meanwhile, the impact of the two proposed signal-injection methods on motor normal operation could be directly observed from the comparison of the stator flux linkages and electromagnetic torque T_{em} before and after the injection. The detailed results for the two proposed signal-injection methods are explained as follows.

6.4.1 The flux-linkage-injection method

To apply the flux-linkage-injection method, a flux linkage bias is injected after t = 4 s with the reference value $\Delta\Psi^s_{sd,ref}$= 0.03 Wb-turns, $\Delta\Psi^s_{sq,ref}$= 0 Wb-turns, roughly 3% of the rated value; no modification to the torque control loop is required. Therefore, as observed in Figure 6.4, the flux-linkage locus is mostly shifted in the horizontal axis.

Moreover, as shown in Figure 6.5 and Figure 6.6, when the injection is implemented after t = 4 s, there is roughly no visible deviation or oscillation for torque and speed. The simulation results indicate the proposed flux-linkage-injection method has negligible impacts on the mechanical characteristics of the DTC induction motor, say the electromagnetic torque and the output speed.

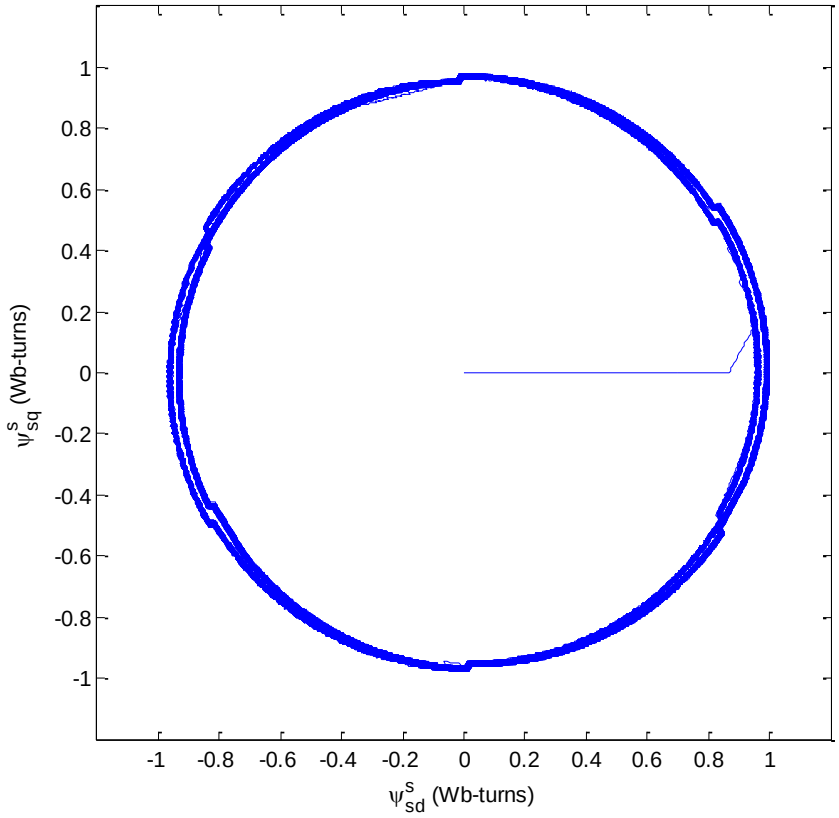

Figure 6.4 $\psi_s^{\,s}$ at constant temperature, with flux-linkage injection $t > 4$ s

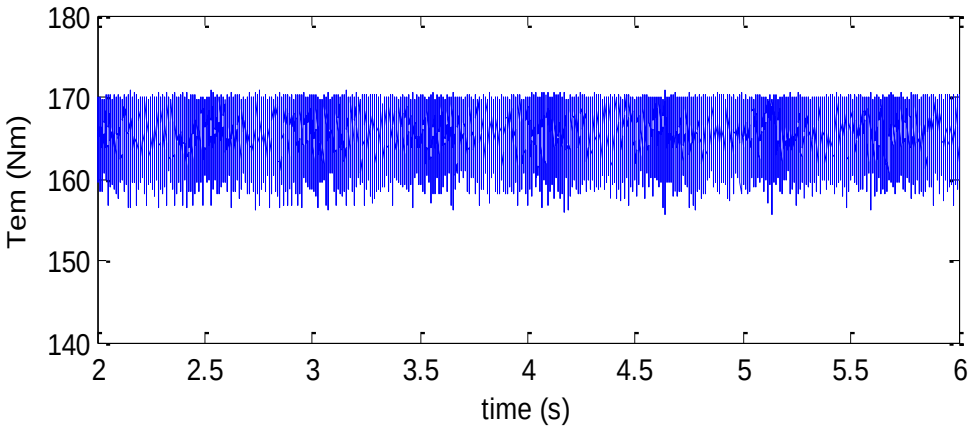

Figure 6.5 T_{em} at constant temperature, with flux-linkage injection $t > 4$ s

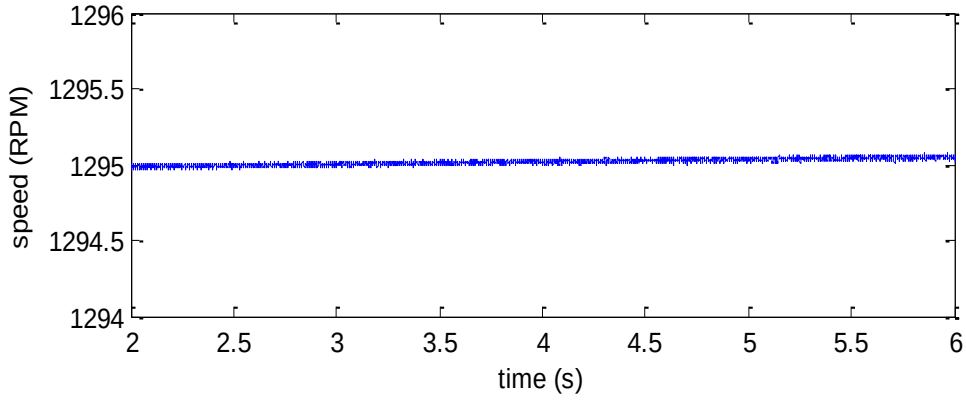

Figure 6.6 ω_m at constant temperature, with flux-linkage injection $t > 4$ s

The extracted DC components for stator flux linkages and currents in the stationary *dq* reference frame appear in Figure 6.7 and Figure 6.8. These results show that the simulated stator-flux-linkage biases are $\left(\Delta\Psi_{sd}^{s}, \Delta\Psi_{sq}^{s}\right)^{T} = (0.0162, -0.0055)^{T}(\text{Wb} - \text{turns})$, and the simulated current offsets are $\left(\Delta I_{sd}^{s}, \Delta I_{sq}^{s}\right)^{T} = (2.865, -1.45\ )^{T}(\text{A})$. On the other hand, the calculated current offsets from equation (6.10) at steady state are $\left(\Delta I_{sd}^{s}, \Delta I_{sq}^{s}\right)^{T} = (2.86, -1.5\ )^{T}(\text{A})$. This close agreement validates the derived relationship between stator-flux-linkage bias and current offset at steady state, as presented in equation (6.10).

In addition, the FFT analysis of the stator flux linkages in Figure 6.9 also illustrates that aside from the DC and fundamental quantities, the second-order harmonic component is also significant and comparable to the DC components. That explains why the actual stator flux linkage offset is different from the specified values $\left(\Delta\Psi_{sd,ref}^{s} = 0.03,\ \Delta\Psi_{sq,ref}^{s} = 0\right)^{T}(\text{wb} - \text{turns})$. Note that in the FFT analysis, the DC values for the

dq-axis flux linkages are always twice as much as the actual values shown in Figure 6.7 respectively.

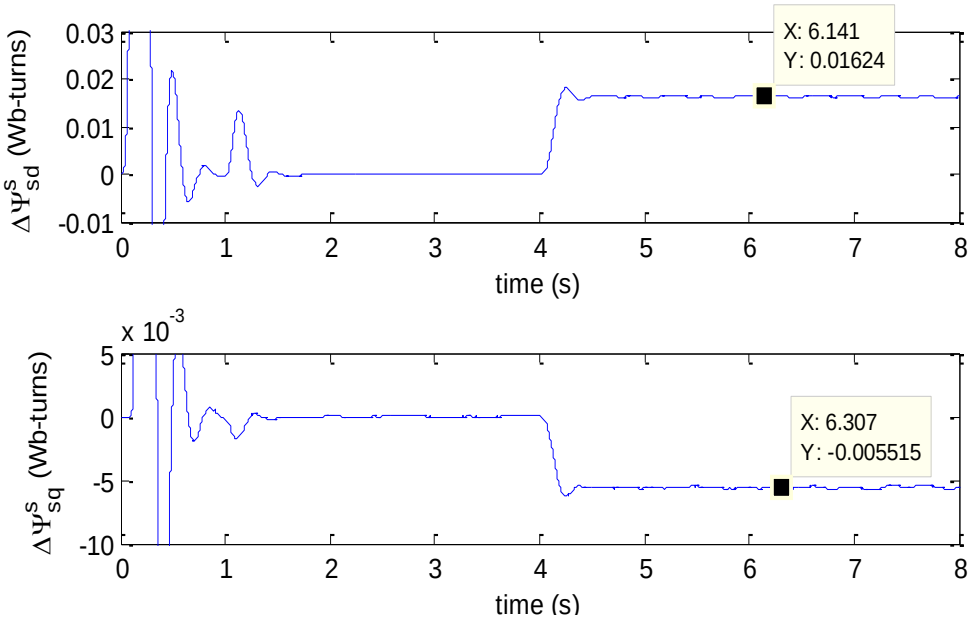

Figure 6.7 $\Delta \Psi_s^s$ at constant temperature, with flux-linkage injection $t > 4$ s

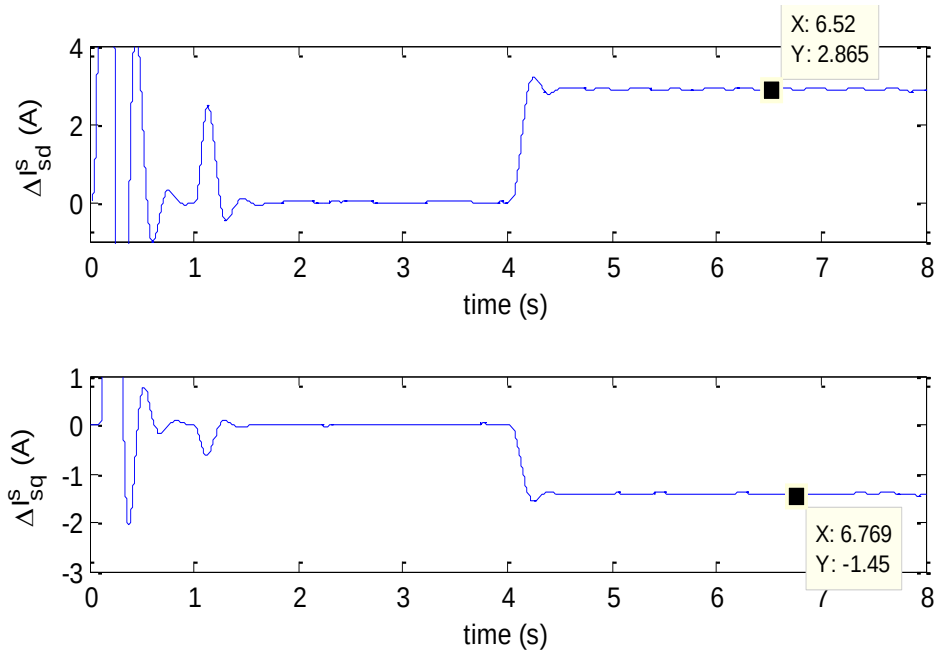

Figure 6.8 ΔI_s^s at constant temperature, with flux-linkage injection $t > 4$ s

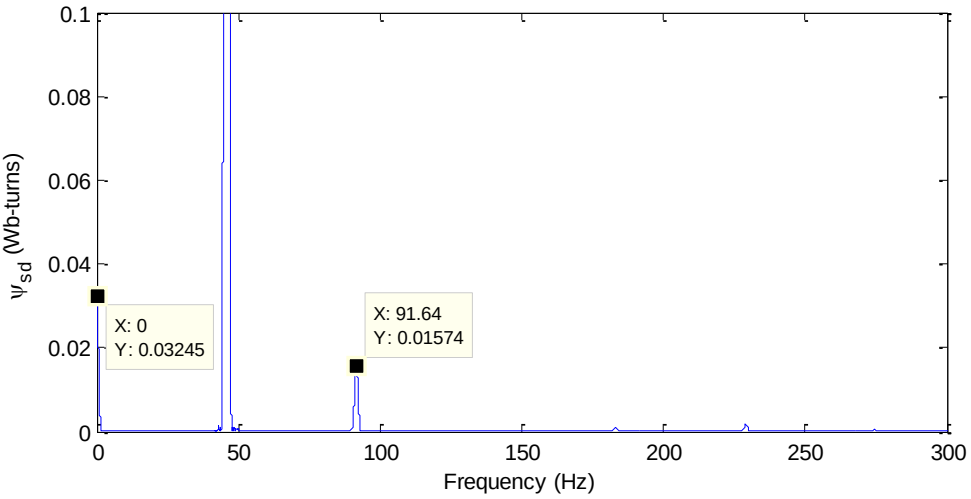

(a) FFT analysis for *d*-axis stator flux linkage

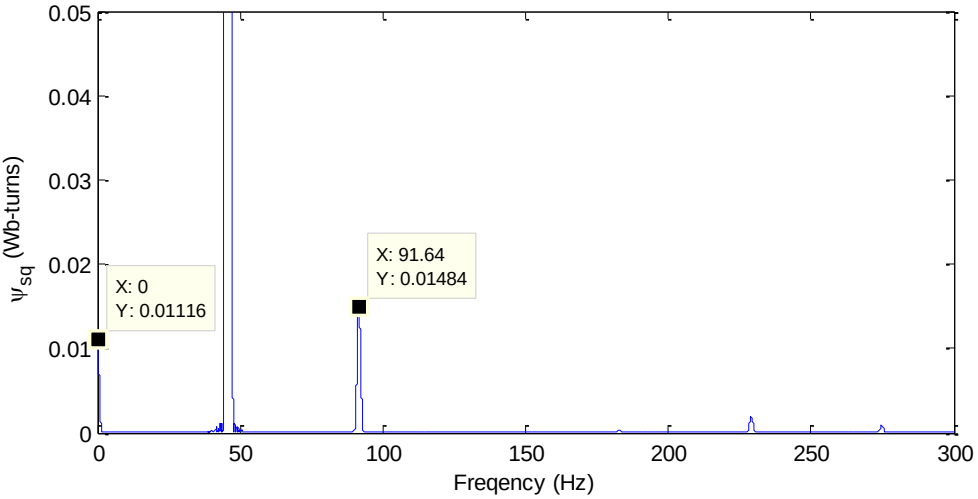

(b) FFT analysis for *q*-axis stator flux linkage

Figure 6.9 ψ_s^s FFT at constant temperature, with flux-linkage injection $t > 4$ s

6.4.2 The torque-injection method

In this simulation, since torque ripple is externally injected to excite the DC current offset, there is some visible torque and speed oscillation, which is shown in Figure 6.10 and Figure 6.11. The actual ripple for the estimated torque T_{em} has a magnitude of only

+/- 4 Nm, or +/- 2.4% of the rated torque, and the duration is very short; similarly, the speed ripple is also negligibly small. Therefore, this torque-injection method has a minimal impact on the machines' normal operation.

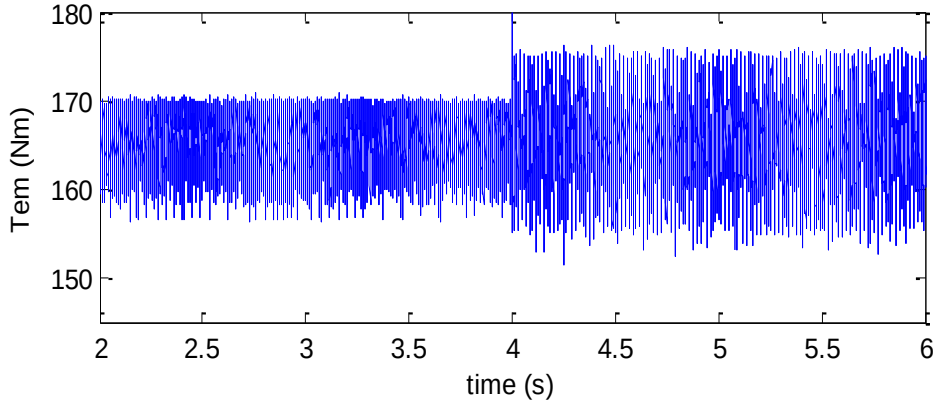

Figure 6.10 T_{em} at constant temperature, with torque injection $t > 4$ s

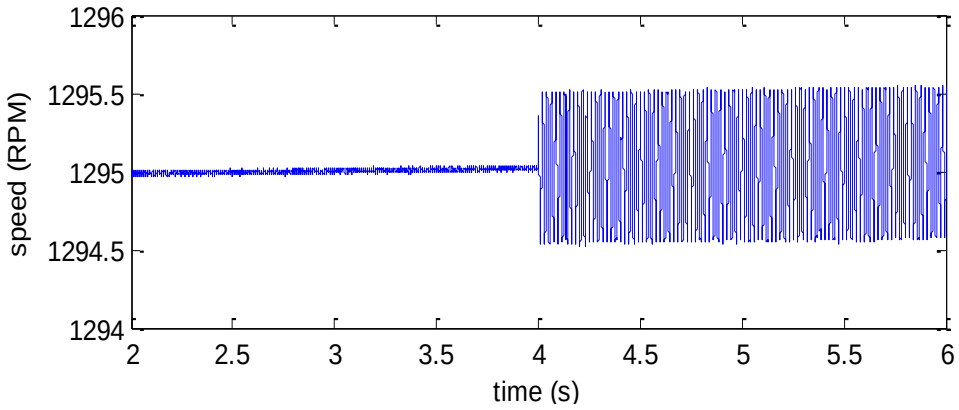

Figure 6.11 ω_m at constant temperature, with torque injection $t > 4$ s

In addition, a zoomed-in view of various related electromagnetic torque quantities are shown in Figure 6.12. In the 4th subplot, while the injection is implemented, the actual

ripple for the estimated torque T_{em} (denoted in black in Figure 6.2) is only +/- 4 Nm, or +/- 2.4% of the rated torque, same as that in Figure 6.10. Meanwhile, the external torque injection command $\Delta T_{em,ref}$ (denoted in red in Figure 6.2) in the 2nd subplot has an amplitude of 14.52 Nm, and the output of the speed PI regulator $T_{em,ref,old}$ (denoted in red in Figure 6.2) in the 1st subplot also has a ripple with the amplitude of 14.5 Nm. However, the ripple of $T_{em,ref,old}$ is almost negative in phase with ripple of the external injection $\Delta T_{em,ref}$ in 2nd subplot. As a result, the actual torque injection command $T_{em,ref,new}$ (denoted in red in Figure 6.2) has an amplitude of only +/- 4 Nm, shown in the 3rd subplot, which is much reduced due to the outer speed loop's compensation, as mentioned in section 6.3.3.

With the torque injection method implemented, the extracted DC flux linkage and current components appear in Figure 6.13 and Figure 6.14 . While the measured current offsets are $\left(\Delta I_{sd}^{s}, \Delta I_{sq}^{s}\right)^{T} = (0.1945, -0.9732\ )^{T}(\mathrm{A})$, the predicted current offsets from equation (6.10) are $\left(\Delta I_{sd}^{s}, \Delta I_{sq}^{s}\right)^{T} = (0.1953, -0.9719)^{T}(\mathrm{A})$, provided that the input flux linkage biases are the labeled value in Figure 6.13 $\left(\Delta \Psi_{sd}^{s}, \Delta \Psi_{sq}^{s}\right)^{T} = (0.001685, -0.004963)^{T}(\mathrm{Wb-turns})$. Hence, this close agreement in the current offsets validates the derived quantitative relationship in the torque-injection method as well.

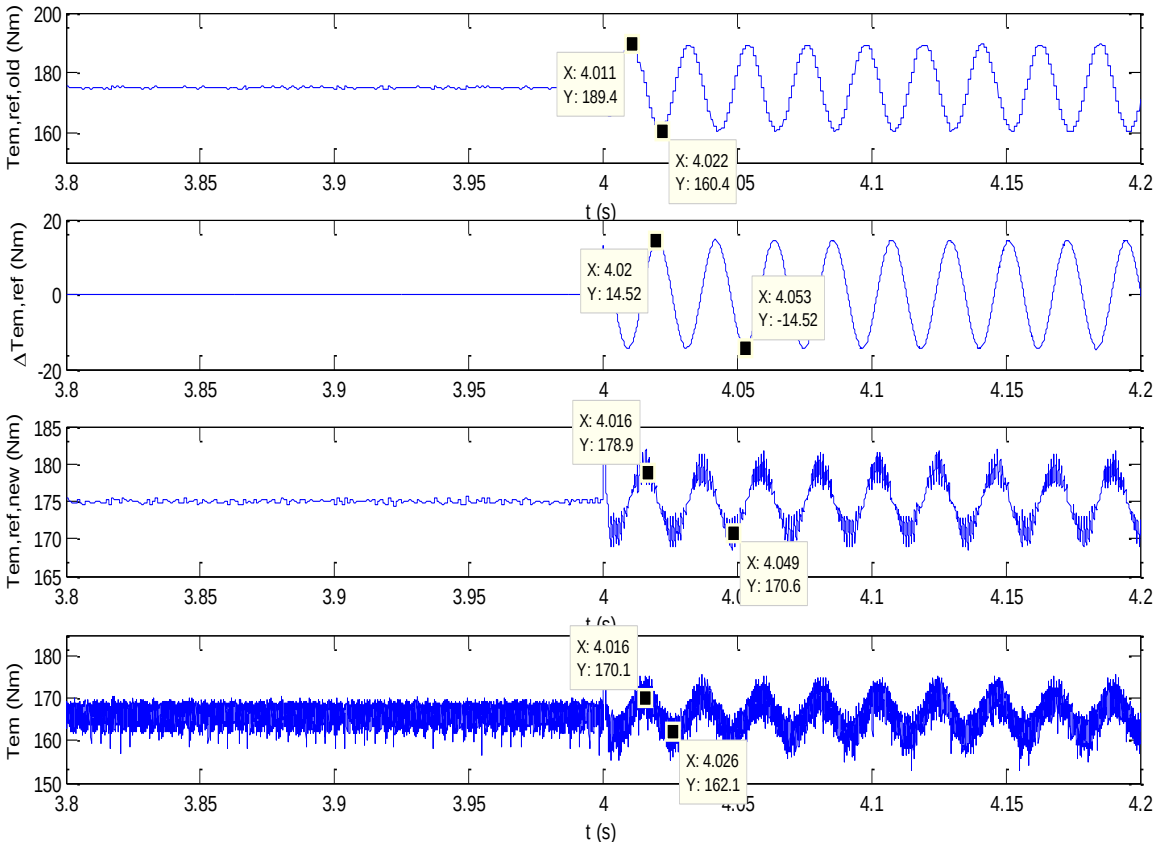

Figure 6.12 Various torque quantities at constant temperature, with torque injection applied after $t > 4$ s

From the validation analysis, it is observed that no matter which injection method is applied to the direct-torque-controlled IM, it will always effectively and indirectly excite a stable DC current in the three-phase stator windings. Furthermore, even with some unwanted second-order harmonics, the quantitative relationship between the stator current and stator flux linkage can always be validated in both the flux-linkage-injection method and torque-injection method.

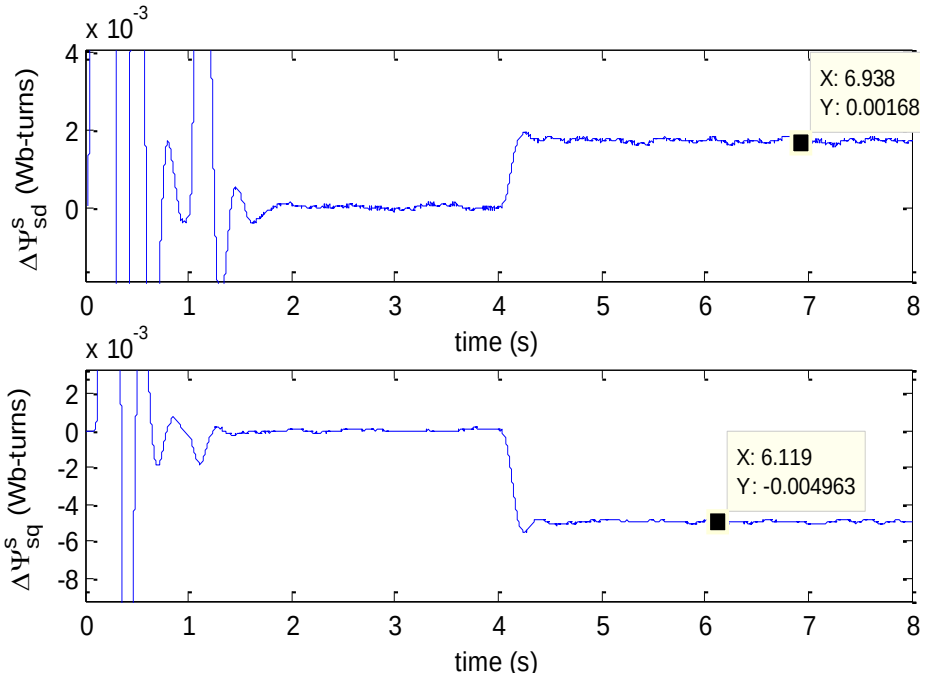

Figure 6.13 $\Delta \Psi_s^s$ at constant temperature, with torque injection t > 4s.

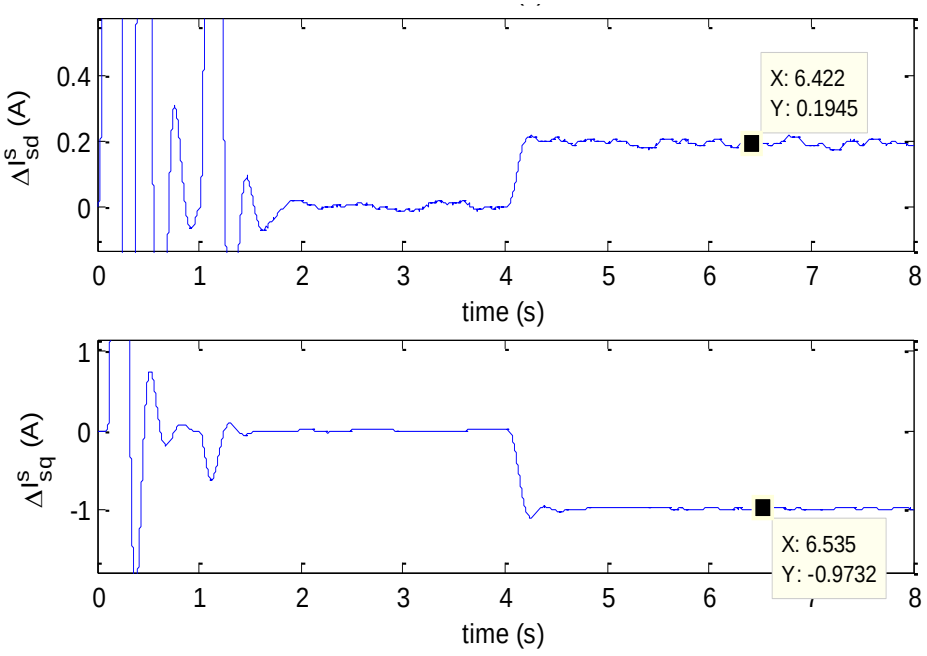

Figure 6.14 ΔI_s^s at constant temperature, with torque injection t >4 s.

6.5 CHAPTER SUMMARY

This chapter presents the modeling effort for a direct-torque-controlled (DTC) induction motor (IM) with additional DC-signal excitation (a typical rotary energy conversion system under DC excitation). Quantitative relationships between the changes of various machine variables during the active DC excitation are provided in the theoretical analysis.

The developed DC-injection model is further simplified for practical implementation and the DC IM modeling work make it possible to excite a desired amount of DC current indirectly in the motor stator winding by superimposing a stator-flux-linkage-bias command in the flux-control loop or a torque-ripple command in the torque-control loop.

The proposed flux-linkage-injection and torque-injection methods are the first novel efforts to implement the DC-signal-injection technique in a DTC motor-drive system. These two methods are proved to be noninvasive because they eliminate the need for additional sensors, require no hardware changes to existing drive systems, and have minimal impacts on the machines' normal operation.

Both injection methods can be implemented to achieve a simple, low-cost, accurate, and non-invasive thermal-monitoring scheme for direct-torque-controlled IMs. The advanced thermal-monitoring technique helps to protect the motor from overheating, insulation degradation, and improve the overall system's control performance, which will be thoroughly discussed in Chapter 8 .

CHAPTER 7 ANALYSIS OF A FIELD-ORIENTED-CONTROLLED IM WITH ACTIVE DC INJECTION

7.1 INTRODUCTION

The previous chapter presents a DC-signal model for a direct-torque-controlled (DTC) IM, based on which two simplified DC-injection methods are proposed, where the DC currents are indirectly and effectively excited in the stator winding via active flux-linkage injection or active torque injection. These are the first effort implementing the DC-injection method in a DTC motor drive system.

This chapter, on the other hand, is focusing on another well-known closed-loop motor control scheme, the field-oriented control (FOC). As explained in the literature review chapter, the DC-injection method has already been implemented in an FOC motor system [48, 49]. However, conventionally, implementation of this DC-injection method causes low-frequency torque ripple, which is undesired especially for high-performance motor applications and becomes a major disadvantage of this type of injection method. This chapter is presenting a complete DC-signal model for an FOC motor system; and then, it takes advantages of the flexibility of the FOC scheme to propose an improved active current-injection method with a form of injection that compensates the fundamental-frequency torque ripple by adding second-order harmonic currents [72].

Section 7.2 presents the DC-injection motor models describing dynamic behavior of an FOC induction machine with a general form of DC excitation. The analysis is based on the well-known *dq*-axis dynamic IM models, where all quantities, especially the torque-ripple component, are carefully studied, which helps to find an improved injection method in the FOC system.

For practical implementation, section 7.3 derives a simple and improved DC-injection method based on the analysis in section 7.2, where the torque ripple is effectively mitigated with additional second-order harmonics.

Section 7.4 presents the comparison results for the proposed DC-injection method and the existing technique [48, 49], and clearly illustrates and verifies that the torque ripple can be significantly mitigated while maintaining the same DC-current injection level.

Section 7.5 summarizes the chapter.

7.2 DC-INJECTION MODELING WORK

As mentioned in Chapter 3 F. Blaschke [40, 41] presented the first paper on field-oriented control (FOC) for induction machines in 1971.

The FOC scheme is carried out in a *dq*-reference frame rotating at the stator frequency. The *d*-axis is aligned with the rotor flux linkage, so that, the rotor flux and torque can be separately controlled by the stator current *dq* components. The rotor flux is a function of the *d*-axis stator current i_{sd}^{e}, while the developed torque is controlled by the *q*-axis current i_{sq}^{e}. [14]. The desired torque profile is either provided by the customer, or directly obtained from the regulator in the outer speed loop with a command $\omega_{m,ref}$

7.2.1 A general form to excite DC signals for an FOC IM

Once an IM reaches steady state at normal operation with a standard indirect-FOC (IFOC) scheme, an DC-signal injection can be externally implemented to the motor, which helps to identify stator winding resistance R_s and, furthermore, the stator-winding average temperature (will be discussed in Chapter 8).

To excite a proper amount of DC signal into an FOC IM at a given operating condition, only the set of controllable variables in a typical FOC algorithm can be modified, namely, the duty-cycle commands D_a, D_b, and D_c, the dq-axis current commands.

For IMs with an FOC scheme, similar to DTC systems, modifying the duty-cycle command is not an effective way to excite the DC offset. This is because the duty-cycle commands D_a, D_b, and D_c are the outputs of dq current regulators, as shown in Figure 7.1; any change made in D_a, D_b, and D_c will be quickly cancelled out by the feedback-control mechanisms of high-bandwidth current loops.

As mentioned in [48, 49], an effective way to excite the DC signal is to modify dq-axis current command directly with an additional current command $\left(\Delta i^e_{sd,ref}, \Delta i^e_{sq,ref}\right)^T$ as shown in Figure 7.1, while, the slip frequency $s\omega_s$ is controlled the same as before: $(s\omega_s)_{ref} = \frac{i^e_{sq,ref}}{i^e_{sd,ref}} \frac{R_r}{L_r}$.

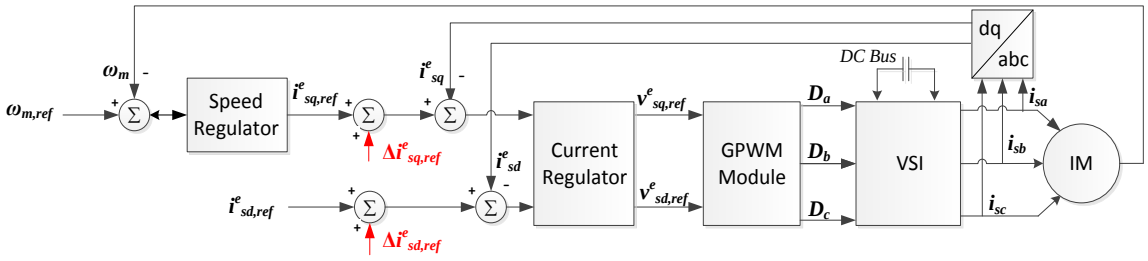

Figure 7.1 DC-current injection in an FOC IM drive.

In order to provide an improved current-injection command, it is necessary to carry out a detailed study of the dynamic performance of an FOC IM before and after injection, and analyze the resultant torque ripple with a general form of injection.

Note that all motor quantities have their usual meanings, as already described in Chapter 6 and superscript *e* indicates the analysis is carried out in the synchronous *dq* reference frame.

Since a DC-current offset in the stationary frame becomes a sinusoidal ripple at the synchronous speed in the synchronous frame, both $\Delta i^e_{sd,ref}$ and $\Delta i^e_{sq,ref}$ need to be sine waves varying at the synchronous speed to excite the desired amount of DC currents into three-phase stator windings. Thus, the actual amount of injection $\left(\Delta i^e_{sd}, \Delta i^e_{sq}\right)^T$ is generally described as in equation (7.1), where $(M, N)^T$ represents a small but noticeable DC quantity, ω_s is the synchronous speed, and $(\theta_1, \theta_2)^T$ are the phase-angle delays.

$$\left(\Delta i^e_{sd}, \Delta i^e_{sq}\right)^T = \left(M\cos(\omega_s t + \theta_1), N\cos(\omega_s t + \theta_2)\right)^T \tag{7.1}$$

The general form of injection in equation (7.1) is not only composed of a DC term $\left(\Delta i^s_{sd0}, \Delta i^s_{sq0}\right)^T$, but also of a second-order harmonic current term $\left(\Delta i^s_{sd2}, \Delta i^s_{sq2}\right)^T$ in the stationary frame as in equation (7.2), where $A, B, P,$ and φ_{a2} are constant values, and expressed as functions of known parameters M, N, θ_1 and θ_2 as shown in equations (7.3) - (7.6).

$$\left(\Delta i^s_{sd}, \Delta i^s_{sq}\right)^T = \left(\Delta i^s_{sd0}, \Delta i^s_{sq0}\right)^T + \left(\Delta i^s_{sd2}, \Delta i^s_{sq2}\right)^T = \begin{bmatrix} A \\ B \end{bmatrix} + P\begin{bmatrix} \cos(2\omega_s t + \varphi_{a2}) \\ \sin(2\omega_s t + \varphi_{a2}) \end{bmatrix}, \tag{7.2}$$

where,

$$A \stackrel{\text{def}}{=} \frac{M}{2}\cos(\theta_1) + \frac{N}{2}\sin(\theta_2), \tag{7.3}$$

$$B \stackrel{\text{def}}{=} -\frac{M}{2}\sin(\theta_1) + \frac{N}{2}\cos(\theta_2), \tag{7.4}$$

$$P \overset{\text{def}}{=} \frac{1}{2}\sqrt{M^2 + N^2 + 2MN\sin(\theta_1 - \theta_2)}, \tag{7.5}$$

$$\varphi_{a2} \overset{\text{def}}{=} \tan^{-1}\left(\frac{M\sin(\theta_1) + N\cos(\theta_2)}{M\cos(\theta_1) - N\sin(\theta_2)}\right). \tag{7.6}$$

In fact, it is the additional second-order current harmonic components $\left(\Delta i_{sd2}^{s}, \Delta i_{sq2}^{s}\right)^{T}$ that contribute to the synchronous-speed torque-ripple mitigation, which is explained and validated in sections 7.3 and 7.4.

7.2.2 The DC-injection model for FOC IMs

During normal operation of an IFOC system, $(s\omega_s)_{ref} = \frac{i_{sq,ref}^{e}}{i_{sd,ref}^{e}}\frac{R_r}{L_r}$; thus, the rotor flux-linkage is aligned with the rotor *d*-axis in the *dq* synchronous frame. Assuming that two current loops respond fast enough and guarantee perfect tracking performance, the stator current components $\left(i_{sd}^{e}, i_{sq}^{e}\right)^{T}$ are equal to their reference components $\left(i_{sd,ref}^{e}, i_{sq,ref}^{e}\right)^{T}$ respectively.

Therefore, the dynamic behavior of a squirrel-cage IM (with a floating stator neutral point) is governed by a differential equation with respect to only three state variables ψ_{rd}^{e}, ψ_{rq}^{e} and ω_m as follows:

$$\begin{bmatrix} 0 = R_r i_{rd}^{e} + p\psi_{rd}^{e} - s\omega_s\psi_{rq}^{e} \\ 0 = R_r i_{rq}^{e} + p\psi_{rq}^{e} + s\omega_s\psi_{rd}^{e} \\ J\frac{d\omega_m}{dt} = T_{em} - T_l - B\omega_m \end{bmatrix}, \tag{7.7}$$

where,

$$\begin{bmatrix} \psi_{rd}^{e} = L_m i_{sd}^{e} + L_r i_{rd}^{e} \\ \psi_{rq}^{e} = L_m i_{sq}^{e} + L_r i_{rq}^{e} \end{bmatrix}, \tag{7.8}$$

$$T_{em} = \frac{3}{2}\frac{p}{2}\frac{L_m}{L_r}\left(\psi_{rd}^{e} i_{sq}^{e} - \psi_{rq}^{e} i_{sd}^{e}\right). \tag{7.9}$$

Note that the rotor resistance R_r in the injection model analysis is increased from the rated value, due to the skin effect. Similar to the previous chapter, once $\left(\Delta i^e_{sd,ref}, \Delta i^e_{sq,ref}\right)^T$ is excited in the stator winding, a change or offsetting term appears in each motor variable. The mechanical speed change $\Delta\omega_m$ is relatively insignificant due to the large inertia of the rotor and load; therefore, ω_m is assumed unchanged after the injection.

The corresponding dynamic state-space system modeling the small changes of the rest of motor variables becomes a differential equation with respect to the state variables $\vec{x} = \left(\Delta\psi^e_{rd}, \Delta\psi^e_{rq}\right)^T$ and input $\vec{u} = \left(\Delta i^e_{sd}, \Delta i^e_{sq}\right)^T$, as shown in equation (7.10):

$$\begin{cases} p\vec{x} = -\begin{bmatrix} \frac{R_r}{L_r} & -s\omega_s \\ s\omega_s & \frac{R_r}{L_r} \end{bmatrix}\vec{x} + \frac{R_r}{L_r}L_m\vec{u} \\ \text{initial condition: } \vec{x}(0) = (0,0)^T \end{cases}. \tag{7.10}$$

Given that $\left(\Delta i^e_{sd}, \Delta i^e_{sq}\right)^T$ is generally expressed as $(M\cos(\omega_s t + \theta_1), N\cos(\omega_s t + \theta_2))^T$ at steady state, the complete solution in the complex domain is derived in equation (7.11), where M_0, M_1, M_2, γ_0 and γ_1 are expressed in equations (7.12)-(7.16).

$$\begin{aligned} \vec{x} &= \frac{L_m\begin{bmatrix} 1+\frac{X_r}{R_r}j & \frac{i^e_{sq,ref}}{i^e_{sd,ref}} \\ -\frac{i^e_{sq,ref}}{i^e_{sd,ref}} & 1+\frac{X_r}{R_r}j \end{bmatrix}}{\left[1+\left(\frac{i^e_{sq,ref}}{i^e_{sd,ref}}\right)^2-\left(\frac{X_r}{R_r}\right)^2\right]+2\frac{X_r}{R_r}j}\vec{u} \\ &= L_m\begin{bmatrix} \frac{M_1}{M_0}Me^{j(\omega_s t+\theta_1+\gamma_1-\gamma_0)} + \frac{M_2}{M_0}Ne^{j(\omega_s t+\theta_2-\gamma_0)} \\ -\frac{M_2}{M_0}Me^{j(\omega_s t+\theta_1-\gamma_0)} + \frac{M_1}{M_0}Ne^{j(\omega_s t+\theta_2+\gamma_1-\gamma_0)} \end{bmatrix}; \end{aligned} \tag{7.11}$$

where,

$$M_0 \stackrel{\text{def}}{=} \sqrt{\left[1+\left(\frac{i^e_{sq,ref}}{i^e_{sd,ref}}\right)^2-\left(\frac{X_r}{R_r}\right)^2\right]^2+\left(2\frac{X_r}{R_r}\right)^2}, \tag{7.12}$$

$$M_1 \stackrel{\text{def}}{=} \sqrt{1+\left(\frac{X_r}{R_r}\right)^2}, \tag{7.13}$$

$$M_2 \stackrel{\text{def}}{=} \frac{i_{sq,ref}}{i_{sd,ref}}, \tag{7.14}$$

$$\gamma_0 \stackrel{\text{def}}{=} \tan^{-1}\left(\frac{2\frac{X_r}{R_r}}{1+\left(\frac{i^e_{sq,ref}}{i^e_{sd,ref}}\right)^2-\left(\frac{X_r}{R_r}\right)^2}\right), \tag{7.15}$$

$$\gamma_1 \stackrel{\text{def}}{=} \tan^{-1}\left(\frac{X_r}{R_r}\right). \tag{7.16}$$

It is observed from equation (7.11) that at steady-state condition, $\vec{x}$ is linearly expressed as a function of the input $\vec{u}$; thus, $\left(\Delta\psi^e_{rd}, \Delta\psi^e_{rq}\right)^T$ are also sine waves varying at synchronous speed in the synchronous frame at steady-state injection.

On the other hand, given $\psi^e_{rq} = 0$ in the FOC system, the induced torque ripple ΔT_{em} is derived in equation (7.17). As mentioned previously, both $\left(\Delta\psi^e_{rd}, \Delta\psi^e_{rq}\right)^T$ and $\left(\Delta i^e_{sd}, \Delta i^e_{sq}\right)^T$ are sine waves at fundamental speed; thus, ΔT_{em} contains not only a dominating fundamental-frequency component, but also DC and second-order harmonic components.

$$\begin{aligned}\Delta T_{em} &= \frac{3}{2}\frac{poles}{2}\frac{L_m}{L_r}\left\{\left[\left(\psi^e_{rd}+\Delta\psi^e_{rd}\right)\left(i^e_{sq}+\Delta i^e_{sq}\right)-\left(\psi^e_{rq}+\Delta\psi^e_{rq}\right)\left(i^e_{sd}+\Delta i^e_{sd}\right)\right]-\right.\\ &\qquad\left.\left[\psi^e_{rd}i^e_{sq}-\psi^e_{rq}i^e_{sd}\right]\right\}\\ &= \frac{3}{2}\frac{poles}{2}\frac{L_m}{L_r}\left[\Delta\psi^e_{rd}\left(i^e_{sq,ref}+\Delta i^e_{sq}\right)+L_m i^e_{sd,ref}\Delta i^e_{sq}-\Delta\psi^e_{rq}\left(i^e_{sd,ref}+\Delta i^e_{sd}\right)\right]\end{aligned} \tag{7.17}$$

To summarize, in the synchronous dq reference frame, equations (7.11) and (7.17) present the steady-state changes of rotor flux linkages and electromagnetic torque with a

general form of current injection in equation (7.1) applied to the FOC IM system. Furthermore, combined with the complete flux-linkage model, the conclusion can be extended as follows:

At the steady-state injection period for an FOC motor drive, sinusoidal stator-current injection at the synchronous speed (in a synchronous *dq* reference frame) produces not only sinusoidal rotor flux linkages, but also sinusoidal rotor currents and stator flux linkages at the same frequency; in addition, the resultant electromagnetic torque ripple is also dominated by a sine component varying at the same speed.

7.3 AN IMPROVED DC-INJECTION METHOD WITH ACTIVE TORQUE MITIGATION

The derivation in section 7.2 presents a complete state-space solution for the DC-injection model, however, further analysis need to be carried out to find an improved injection method for an FOC IM system. The details are introduced as follows.

Considering that during normal speed operation $\left(\frac{X_r}{R_r}\right)^2 \gg 1$, M_0 roughly equals $\left(\frac{X_r}{R_r}\right)^2 \gg 1$, and M_1 is approximated as $\frac{X_r}{R_r}$. Then, $\frac{M_1}{M_0} \approx \frac{R_r}{X_r}$ and $\frac{M_2}{M_0} \approx 0$. Then, an approximate form of the system's state-space solution in equation (7.11) appears as follows, which can be used to effectively mitigate the torque ripple.

$$\vec{x} = \begin{bmatrix} \Delta\psi_{rd}^e \\ \Delta\psi_{rq}^e \end{bmatrix} \approx L_m \frac{R_r}{X_r} e^{j(\gamma_1 - \gamma_0)} \vec{u} \tag{7.18}$$

where,

$$\vec{u} = \left(\Delta i_{sd}^e, \Delta i_{sq}^e\right)^T = \begin{bmatrix} M e^{j(\omega_s t + \theta_1)} \\ N e^{j(\omega_s t + \theta_2)} \end{bmatrix} \tag{7.19}$$

On the other hand, since $\left(\Delta i_{sd}^e, \Delta i_{sq}^e\right)^T$ is negligibly small compared to the load current $\left(i_{sd,ref}^e, i_{sq,ref}^e\right)^T$, ΔT_{em} in equation (7.17) is further approximated as in equation

(7.20), where it is clearly observed that the fundamental terms dominate the induced torque ripple.

$$\Delta T_{em} \approx \frac{3}{2}\frac{poles}{2}\frac{L_m}{L_r}\left[\Delta\psi_{rd}^{e} i_{sq,ref}^{e} - \Delta\psi_{rq}^{e} i_{sd,ref}^{e} + L_m i_{sd,ref}^{e} \Delta i_{sq}^{e}\right] \tag{7.20}$$

Substituting the approximate rotor flux linkage in equation (7.18) into the fundamental torque ripple in equation (7.20) yields a further simplified expression for the electromagnetic torque ripple ΔT_{em} in the complex domain in equation (7.21).

$$T_{em} \approx \frac{3}{2}\frac{poles}{2}\frac{L_m^2}{L_r}\left\{\frac{R_r}{X_r}\left[M e^{j(\theta_1+\gamma_1-\gamma_0)} i_{sq,ref}^{e} - N e^{j(\theta_2+\gamma_1-\gamma_0)} i_{sd,ref}^{e}\right] + N e^{j\theta_2} i_{sd,ref}^{e}\right\} e^{j\omega_s t} \tag{7.21}$$

In order to mitigate the ripple, it is expected to adjust M, N, θ_1 and θ_2, so that $\Delta T_{em} = 0$. However, this relationship is complicated and highly depends on motor parameters as well as the motor working point $\left(i_{sd,ref}^{e}, i_{sq,ref}^{e}\right)^T$, which are all difficult to obtain for the entire operating range in real life. Therefore, it is technically impractical and infeasible to guarantee $\Delta T_{em} = 0$.

On the other hand, during normal speed operation, the small quantity $\left(\frac{R_r}{X_r}\right)$ causes the first two terms in equation (7.21) to be much smaller compared to the last term ($N e^{j\theta_2} i_{sd,ref}^{e}$). Thus, a practically-simplified and improved form of injection is to command $N = 0, \theta_1 = \theta_2 = 0$, while maintaining the desired DC-current level M at a small but noticeable fixed value, as shown in equation (7.22). The resultant low-frequency torque ripple is approximated as in equation (7.23).

$$\left(\Delta i_{sd}^{e}, \Delta i_{sq}^{e}\right)^T = \left(M\cos(\omega_s t), 0\right)^T \tag{7.22}$$

$$\Delta T_{em} \approx \frac{3}{2}\frac{poles}{2}\frac{L_m^2}{L_r}\frac{R_r}{X_r} M i_{sq,ref}^{e} e^{j(\omega_s t+\gamma_1-\gamma_0)} \tag{7.23}$$

In addition, according to equations (7.2)-(7.6), the corresponding injected DC-current and second-harmonic current components are also expressed as in equations (7.24)-(7.25), which turn out to be of equal magnitude, 50% of the injection level *M*. It is suggested in the future to change *M* and *N* and inject different amounts of second harmonics, to study its impact on fundamental-frequency torque ripple.

$$\left(\Delta i_{sd0}^{s}, \Delta i_{sq0}^{s}\right)^{T} = \left(\frac{1}{2}M, 0\right)^{T} \tag{7.24}$$

$$\left(\Delta i_{sd2}^{s}, \Delta i_{sq2}^{s}\right)^{T} = \left(\frac{1}{2}M\cos(2\omega_s t), \frac{1}{2}M\sin(2\omega_s t)\right)^{T} \tag{7.25}$$

7.4 COMPARISON AND VALIDATION

Section 7.3 introduces an improved injection method for FOC IM implementation based on the rigorous analysis. This section presents a comparison study of the torque-ripple value between the improved method and the existing techniques [48, 49] at the normal speed operation.

For comparison purposes, the motor is operated at the same speed and load level in both cases; the injection is implemented after t = 6 s. Before moving towards the detailed comparison results, a theoretical analysis is carried out for the existing injection method [48, 49].

For the existing method [48, 49] the current command is shown in equation (7.26), where *M'* represents the sinusoidal disturbances in i_{sd}^{e} and i_{sq}^{e}; thus, the resultant torque ripple $\Delta T_{em}'$ can also be obtained using the general form of torque ripple in equation (7.21) and approximated as in equation (7.27).

$$\left(\Delta i_{sd}^{\prime e}, \Delta i_{sq}^{\prime e}\right)^{T} = \left(M'\cos(\omega_s t), M'\cos\left(\omega_s t + \frac{\pi}{2}\right)\right)^{T} \tag{7.26}$$

$$\Delta T'_{em} \approx \frac{3}{2}\frac{poles}{2}\frac{L_m^2}{L_r} M' \left\{\frac{R_r}{X_r}\left[e^{j(\gamma_1-\gamma_0)} i^e_{sq,ref} - e^{j\left(\frac{\pi}{2}+\gamma_1-\gamma_0\right)} i^e_{sd,ref}\right] + e^{j\left(\frac{\pi}{2}\right)} i^e_{sd,ref}\right\} e^{j\omega_s t}$$

$$\approx \frac{3}{2}\frac{poles}{2}\frac{L_m^2}{L_r} M' i^e_{sd,ref} e^{j\left(\omega_s t+\frac{\pi}{2}\right)} \tag{7.27}$$

In addition, according to equations (7.2)-(7.6), the actual injected DC current and second-order harmonic current for the existing method [48, 49] are also obtained as shown in equations (7.28)-(7.29). To guarantee the DC current exactly the same for the improved and existing signal-injection methods, it is required that $M' = \frac{1}{2}M$.

$$\left(\Delta i'^s_{sd0}, \Delta i'^s_{sq0}\right)^T = (M', 0)^T, \quad \text{where } M' = \frac{1}{2}M \tag{7.28}$$

$$\left(\Delta i'^s_{sd2}, \Delta i'^s_{sq2}\right)^T = (0,0)^T \tag{7.29}$$

With the two sets of injection command for the improved and existing methods given in equations (7.22) and (7.26) respectively, the comparison results for the motor performance are shown in Figure 7.2, Figure 7.3, and Table 7.1.

It is observed that under the condition $M' = \frac{1}{2}M$, the excited DC current is roughly the same for both methods, while the resultant torque ripple is significantly different: the peak-to-peak torque ripple for the improved method is only 3.4 Nm, while the corresponding value for the existing method [48, 49] is 10.6 Nm.

Table 7.1 Comparison between different FOC current-injection methods

	T_{em} ripple (Nm)	DC component of *d*-axis stator-current (A)	DC component of *q*-axis stator-current (A)
The improved method	3.4	1.824	0.018
The existing method	10.6	1.840	-0.013

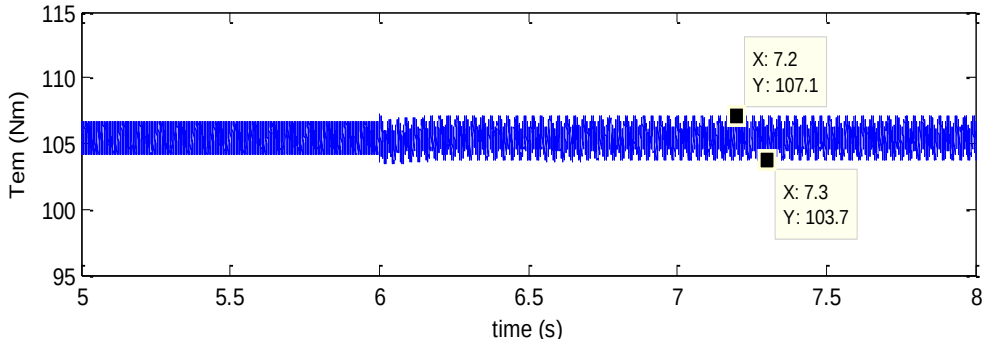

(a) T_{em} with the improved injection method t > 6 s

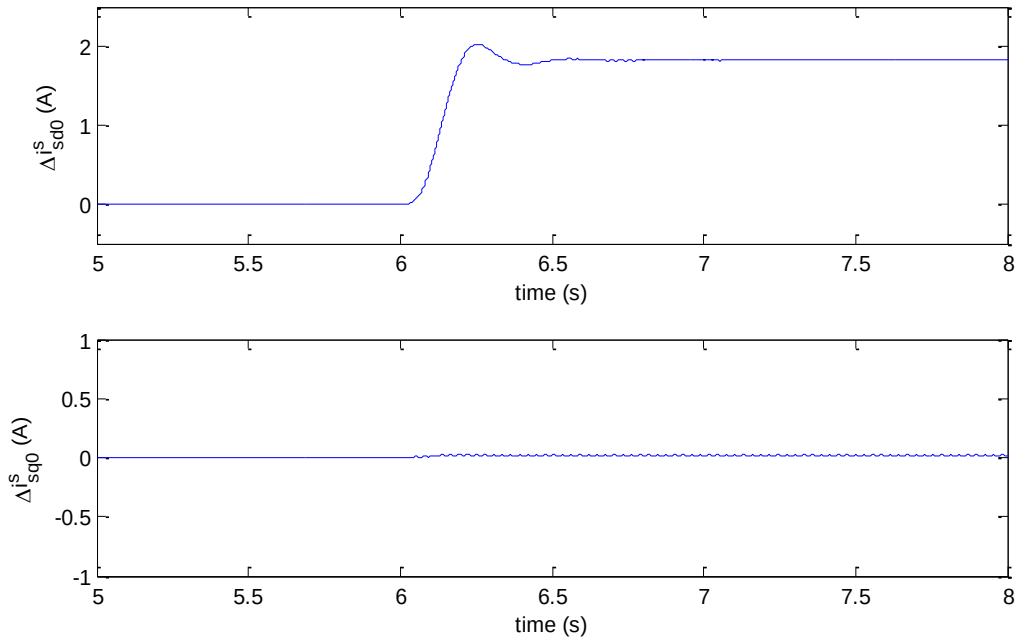

(b) Δi^s_{sd0} and Δi^s_{sq0}, with the improved injection method t > 6 s

Figure 7.2 T_{em}, $\Delta i_{sd0}{}^s$, $\Delta i_{sq0}{}^s$ at constant temperature, with the improved FOC current injection t > 6 s.

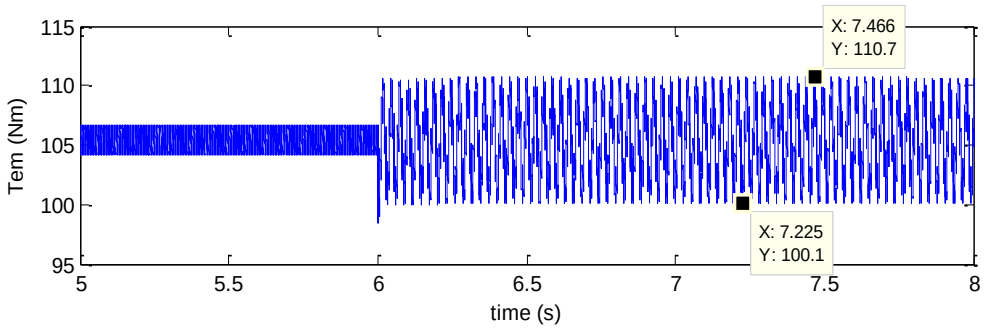

(a) T_{em}, with the existing injection method $t > 6$ s

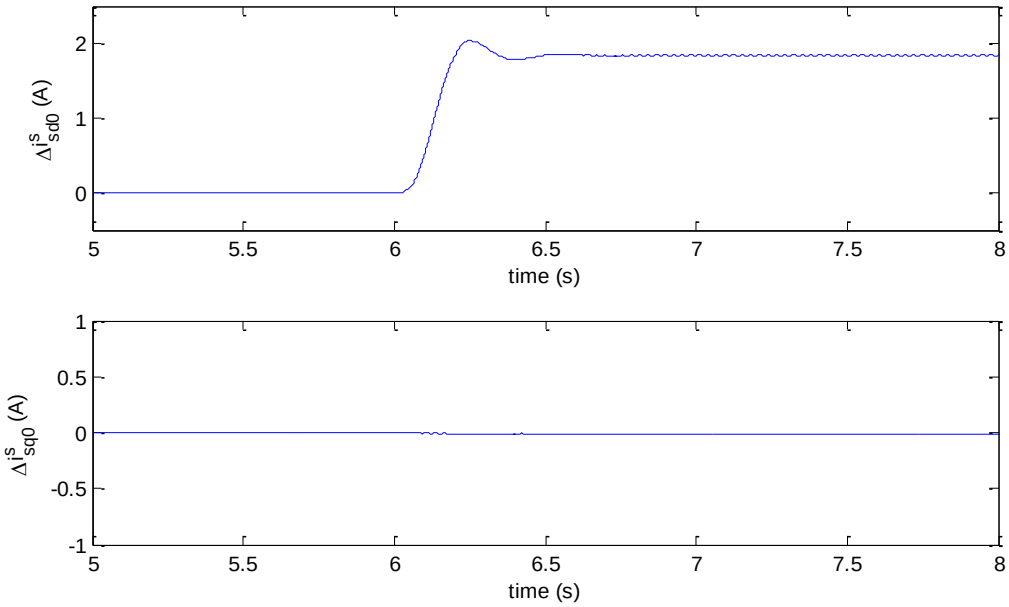

(b) Δi^s_{sd0} and Δi^s_{sq0}, with the existing injection method $t > 6$ s

Figure 7.3 T_{em}, $\Delta i_{sd0}{}^s$, $\Delta i_{sq0}{}^s$ at constant temperature, with the exiting FOC current injection $t > 6$ s [48, 49].

As a conclusion, it is observed from Table 7.1, Figure 7.2, and Figure 7.3 that, with the improved method and the added second-order current harmonics, the low-frequency torque ripple is significantly reduced by roughly 70%. Considering that for practical implementation, the signal is injected intermittently into the motor winding and the

desired DC level *M* is small, this improved method has minimal impacts on the motors' normal operation.

Furthermore, the percentage torque ripple for the above two methods is analytically presented in (7.30).

$$\left|\frac{\Delta T_{em}}{T_{em}}\right| \approx \left(\frac{R_r}{X_r}\right)\frac{M}{i^e_{sd,ref}} \ll \left|\frac{\Delta T'_{em}}{T_{em}}\right| \approx \frac{M'}{i^e_{sq,ref}}, \quad \text{where } M' = \frac{1}{2}M \tag{7.30}$$

It is observed that the torque ripple for the improved method ΔT_{em} is indeed much smaller compared to the torque ripple for the existing method$\Delta T'_{em}$, because the ripple is not only limited by the small value *M*, but also $\left(\frac{R_r}{X_r}\right)$ quantity. Even when the flux-linkage is weakened and $i^e_{sd,ref}$ is reduced for the high-speed application, the increase of X_r can still guarantee a small torque ripple.

In addition, with the proposed injection method, the resultant torque ripple ΔT_{em} is independent of the motor load level $i^e_{sq,ref}$. On the other hand, the torque ripple $\Delta T'_{em}$ for the existing method in [48, 49] is limited by *M'* only, and will be even more significant for a light-load condition with a smaller $i^e_{sq,ref}$.

Another advantage for the improved method is that since the torque (speed) ripple is much reduced, the compensation of the outer speed loop to the *q*-axis current command is less severe and comparably negligible. Thus, the actual excited DC bias is less distorted, and is closer to its command compared to the existing method in [48, 49].

For comparison purposes in this section, the outer speed loop is opened; $i^e_{sq,ref}$ is externally determined from the desired load level for both methods. Therefore, neither of the two commanded injections is affected by the outer motor-speed control loop.

7.5 CHAPTER SUMMARY

This chapter presents a DC-injection motor state-space model describing dynamic behaviors of an FOC induction machine with a general form of DC excitation. The detailed analysis results in an improved current-injection method.

With this improved injection technique, the induced synchronous-speed torque ripple, which is conventionally a major disadvantage for DC-signal-injection methods [51, 52, 73], is effectively mitigated with the added second-order harmonic currents, while the DC-current injection level maintains the same.

This improved current-injection method is also easy and simple to implement, because it eliminates the need for additional sensors, and do not require any hardware adjustments to the standard drive systems.

This advanced current-injection method can further be extended to achieve a remote, simple, low-cost, accurate and non-invasive thermal-monitoring scheme for field-oriented-controlled (FOC) IMs. This thermal-monitoring scheme helps to protect the motor from overheating, insulation degradation, and improve the overall system's control performance, while still guarantee minimal impacts on the motor normal operation, especially for high-performance motor applications, which will be discussed in Chapter 8 .

CHAPTER 8 IMPLEMENTATION OF ACTIVE DC INJECTION FOR THERMAL-MONITORING OF CLOSED-LOOP-CONTROLLED IMS

8.1 INTRODUCTION

The previous two chapters present the analytical investigation in modeling an inverter-fed induction motor (IM) (a typical rotary-motion system) with active DC injection. The IM is closed-loop controlled via two popular motor-control algorithms, namely, the direct-torque-control (DTC) algorithm (in Chapter 6) and field-oriented-control (FOC) algorithm in (Chapter 7). The modeling effort can further be simplified and transformed into various practical approaches to excite a proper amount of DC current directly or indirectly into IM stator windings based on different closed-loop motor-control algorithms.

These proposed DC-injection methods, either in a DTC or an FOC motor drive system, lead to a simple, low-cost, accurate, and non-invasive thermal-monitoring scheme for closed-loop-controlled IMs, where the average stator-winding temperature is indirectly obtained from stator resistance estimation. The thermal-monitoring technique is thoroughly discussed in this chapter [69-72].

Section 8.2 explains the basic principles for the DC-signal-injection-based online thermal-monitoring scheme. The principle of the temperature-estimation approach is validated in simulation under variable temperature condition.

Sections 8.3 and 8.4 illustrate the hardware implementation of the proposed DTC or FOC injection methods in a custom-built programmable motor drive system for thermal monitoring purposes. For each of the two closed-loop control schemes, the inverter non-

idealities are carefully taken into consideration, and the improved real-time signal-processing techniques are thoroughly discussed.

It is eventually proved and validated in section 8.5 that the proposed injection methods can provide reliable thermal-monitoring schemes that guarantee accurate stator-winding average temperature tracking results under various operating conditions and cooling modes.

Section 8.6 summarizes the chapter.

8.2 THERMAL-MONITORING SCHEME PRINCIPLE

8.2.1 Principle

As explained in Chapter 3 accurate thermal monitoring of the motor stator winding is essential to protect an induction machine from overheating, improve the machine utilization, and enhance the overall system's performance. Considering the expense and complexity of the installation of embedded winding-temperature sensors, researchers have moved towards various temperature-estimation techniques for decades, especially for low-cost low-to-medium horse-power induction machines (IMs).

The existing approach is broadly classified into the following two categories: thermal-model-based approaches and parameter-based approaches. Parameter-based approaches estimate temperature from winding resistance and have significant advantages over thermal-model methods. These approaches eliminate the need to update thermal parameters (thermal resistance and capacitance) of the thermal model offline [48-50]; moreover, they can be universally implemented in various types of machines [48, 49]; and, their accuracy is not affected by motor operating conditions and cooling modes,

especially considering the wide-speed range of variable-frequency motor drives and unexpected abnormal cooling situations [15, 48-53].

While many researchers are focusing on the technique to obtain resistance information from the motor AC circuit models [45, 50, 52, 53, 58, 74-83], another widely-known parameter-based approach for stator-winding thermal-monitoring scheme is to estimate the winding temperature from the DC stator resistance R_s based on a DC-signal motor model [15, 32-35, 38, 39, 48, 49, 51, 52, 69-71, 84]. This is especially applied to motors under normal-speed operating conditions, in which $X_r \gg R_r$ and $X_s \gg R_s$.

Although an accurate estimate is only guaranteed at steady state during the injection period [51], the DC-model estimation is independent of all other motor parameters and inherent motor asymmetry, and is proved to a most accurate and reliable [15, 33, 51]. The basic principle of the DC-injection-based thermal monitoring approach is explained as follows.

With some proper amount of DC current excited in the motor stator winding, some DC stator voltage offsets occur as well due to the DC resistance. Therefore, given accurate measurement or estimation of the stator three-phase currents and voltages, it is feasible to obtain an accurate estimation for the stator DC resistance R_s.

Once the winding resistance R_s is obtained from the injected DC voltage and current offsets, stator winding temperature can be estimated using equation (8.1) according to the IEEE standard [64], where R_b is the resistance at known temperature t_b R_t is the resistance during the test, t_t is the estimated test temperature, and k_1 is a constant based on the winding material. As presented in International Annealed Copper Standard (IACS),

k_1 is 234.5 for 100% IACS conductivity copper, or 225 for aluminum, based on a volume conductivity of 62%.

$$t_t = \left(\frac{R_t}{R_b}(t_b + k_1)\right) - k_1 \tag{8.1}$$

8.2.2 IM simulation validation

As mentioned previously, once some proper amount of DC current is excited in the motor winding, the DC stator resistance can be obtained, which acts as a direct indicator for the DC-injection-based thermal-monitoring scheme. This thermal-monitoring principle can be validated using either of the proposed injection methods, namely:

(1) A flux-linkage-injection method for a DTC IM drive,

(2) A torque-injection method for a DTC IM drive,

(3) An improved current-injection method with active torque mitigation for an FOC IM drive.

In this section, only the estimation results for the third method, an improved FOC IM current-injection method with active torque mitigation, is elaborated to validate the basic thermal-monitoring principle. The rest two methods perform in a similar way.

8.2.2.1 Thermal monitoring results at constant temperature

In this simulation case, the IM stator-winding resistance is maintained constant at the room-temperature value. When the improved current-injection method is applied to a standard FOC IM drive after t > 6 s, the stator-resistance estimation is instantaneously updated, and will be stable once the injection reaches the steady-state condition.

The average resistance of three-phase stator windings for the improved injection method, $R_{s,avg}$, is presented in Figure 8.1. It illustrates that, with this injection method applied, an accurate average stator resistance for three phase windings $R_{s,avg}$, can be obtained after t = 6.5 s (0.5 s after the improved current-injection method is applied in the FOC motor); $R_{s,avg}$ soon reaches the actual value of 0.22 Ω with a steady state error +/- 3%. In addition, since the LPF cannot perfectly filter out the fundamental AC components, there always exists small sine-wave variation in the resistance estimation. To summarize, even with the additional second-order harmonics excited by the improved injection method in the IM, the accuracy of $R_{s,avg}$ estimation is still guaranteed, and will be proved to be sufficient for thermal monitoring purposes at a varying temperature condition in section 8.2.2.2 .

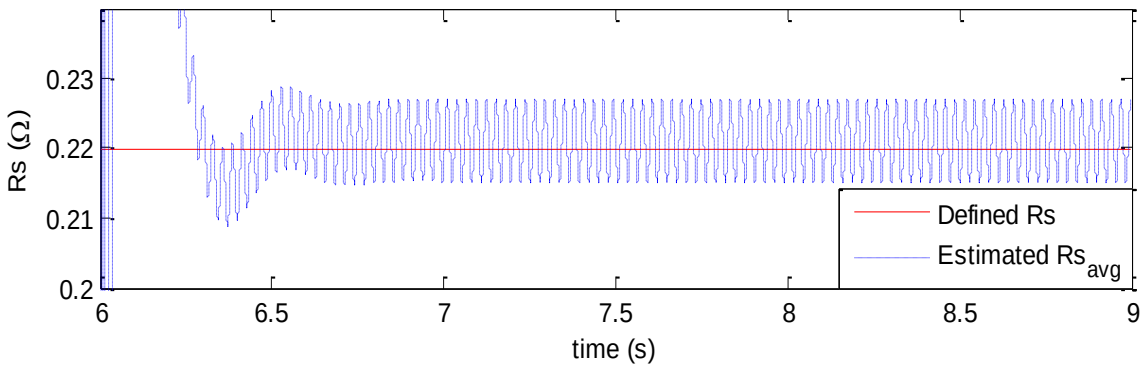

Figure 8.1 Estimated $R_{s,avg}$ at constant temperature, with the improved current-injection method for FOC IMs, with injection t > 6 s

8.2.2.2 Thermal monitoring results at variable temperature

In this case, stator resistance and temperature are kept constant until t = 8 s, and then increased exponentially according to a predefined thermal model. In this model, the thermal time constant is greatly reduced in order to reduce the simulation time. The improved signal-injection-based thermal monitoring method is applied after t = 6 s, and the results are presented in Figure 8.2 and Figure 8.3.

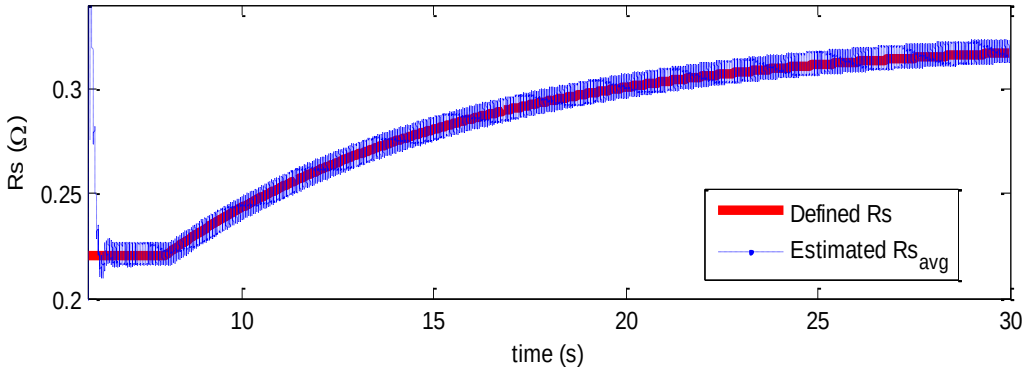

Figure 8.2 Estimated stator winding average resistance $R_{s,avg}$ at variable temperature, with the improved FOC current injection t > 6 s.

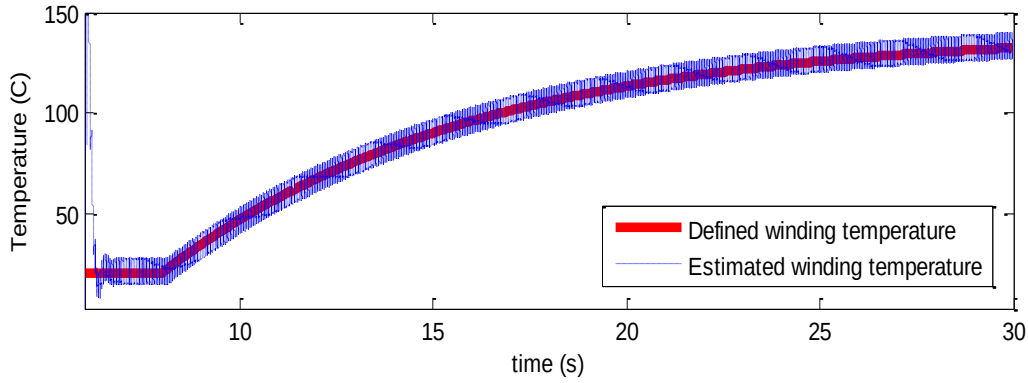

Figure 8.3 Stator winding average temperature estimation at variable temperature, with the improved FOC current injection t > 6 s.

It is observed that while the temperature is fast increasing from the room temperature at 20℃ to 130℃ in 30 seconds (note that the thermal time constant is significantly reduced in the simulation validation), both the estimated resistance and temperature track well with their defined values, This simulation scenario validates the basic principle of this DC-injection-based thermal monitoring scheme for an FOC IM drive under variable temperature condition.

8.3 REAL-TIME SIGNAL-PROCESSING TECHNIQUES

The simulation results in the previous section validate the basic principle of the injection-based thermal-monitoring scheme for closed-loop-controlled IM drive system.

For hardware implementation, once the DC stator-current offset, together with some second harmonics, is successfully excited via either of the proposed methods, the next step is to extract the DC components from the stator current and voltage measurements/estimations respectively. The real-time signal-processing techniques are carried out in a typical DSP-based motor drive system.

However, considering inverter non-idealities, there is a challenge for a typical inverter drive to accurately estimate the DC component of motor terminal voltages. This is explained as follows. For a conventional motor drive system, the only measured electric quantities are stator currents i_{sa}, i_{sb} and the DC bus voltage V_{dc}; thus the phase-*c* current and three-phase terminal voltages are estimated in equations (8.2) and (8.3).

$$i_{sc} = -i_{sa} - i_{sb}, \tag{8.2}$$

$$\left.\begin{aligned} v_{an} &= D_a V_{dc} \\ v_{bn} &= D_b V_{dc} \\ v_{cn} &= D_c V_{dc} \end{aligned}\right\}. \tag{8.3}$$

As pointed out by the authors in [48, 49], the voltage drops across IGBTs and diodes for a typical two-level IGBT converter result in the terminal voltages not the same as the DC bus voltage V_{dc} when turned on, or zero when turned off. Furthermore, the actual duty ratios are slightly different from the commanded duty ratios in the motor controller, because of the dead-time delay and turn-on/ turn-off time delay of the drive system.

Based on this reasoning, the conventional voltage estimation in equation (8.3) is inaccurate, especially when the machine is working in an unbalanced condition due to the excited DC-current offset (during the normal balanced condition, the impacts of the inaccurate terminal voltages and duty ratios on voltage estimation for the first half cycle of load-current are effectively cancelled out by the impact on the second half cycle for each period; thus, the average impact for one complete cycle is negligible) [48, 49]. This results in errors in the extraction of the DC voltage components and significantly affects the accuracy of the DC stator-winding resistance estimation and stator-winding temperature estimation.

This section will provide a complete study of the real-time signal-processing technique for both DTC and FOC algorithms, and are finally implemented in a custom-built programmable motor-drive system. The experimental results in section 8.5 will then demonstrate that the proposed technique gives accurate and robust stator-temperature estimation, regardless of the motor operating conditions and cooling modes.

8.3.1 Improved signal-processing techniques for a DTC drive

The impact of the inverter non-idealities on a standard DTC motor drive is discussed in details. The corresponding compensation technique is introduced thereafter.

8.3.1.1 Duty-ratio estimation compensation

Consider the simplest form of DTC scheme, where the duty ratio command has only two output states: either '0' or '1' for one given control period *T*, determined by the DTC look-up table in Figure 6.1. Let us take phase *a* as an example.

Considering the case where the two consecutive duty ratio commands at $(t^* - T)$ and t^* are unchanged, where T is the control period, like (1, 1) or (0, 0), that indicates there will not be any switching at $t = t^*$ at all; therefore the actual duty ratio $D'_a(t^*)$ at the given time $t = t^*$ matches the commanded value of $D_a(t^*)$ exactly. On the other hand, if the phase a switches from high to low or from low to high level at $t = t^*$, the actual duty ratio, $D'_a(t^*)$, will be different from the commanded $D_a(t^*)$ and affected by the dead-time duty ratio D_{dt} and the turn-on/turn-off time-delay duty ratio D_{ondly}/D_{offdly} for the given inverter system. In general, the slight change of actual duty ratio for each cycle in DTC is related not only to the present duty ratio command $D_a(t^*)$ but also to the previous duty cycle command $D_a(t^* - T)$. The details are demonstrated as follows.

Figure 8.4 - Figure 8.7 show one phase of a three-phase inverter, where phase a current i_{sa} is flowing outwards. If the duty cycle command for phase a transits from low to high at $t = t^*$, the current flow will migrate from the lower path to the upper path only after the upper IGBT is turned on. Considering the fact that the dead time is normally implemented only by delaying the opening edge of the IGBT gate signal, the rising edge of the actual phase a gate signal $D'_a(t)$ will get delayed by the total amount of time $(D_{dt} + D_{ondly})T$, compared to the ideal command $D_a(t)$, as shown in Figure 8.5(a).

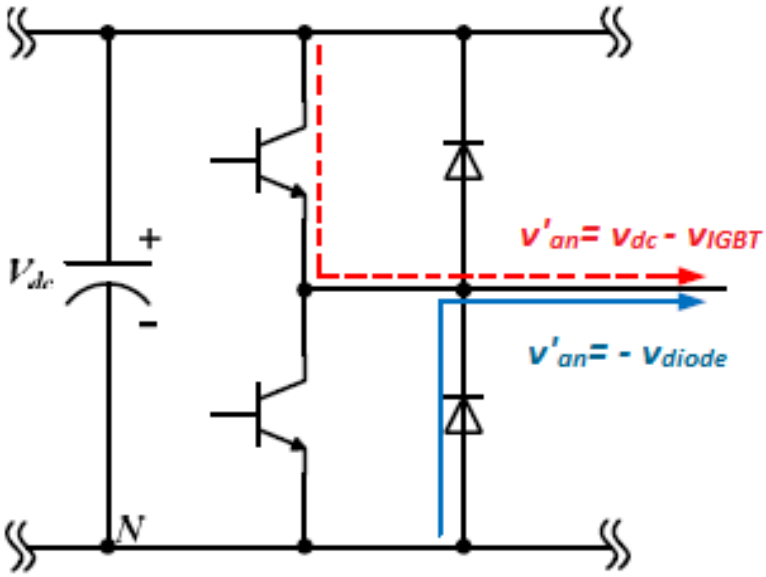

Figure 8.4 Phase a current flows outwards

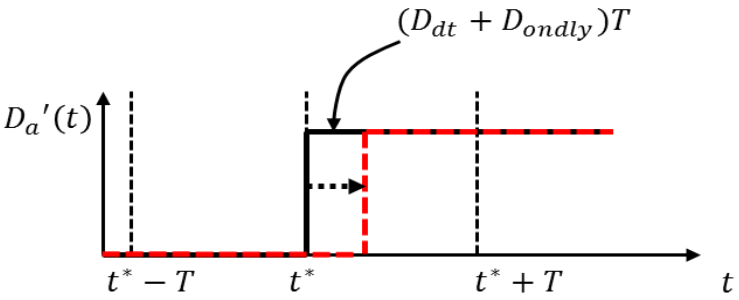

(a) Consecutive command pair (0, 1)

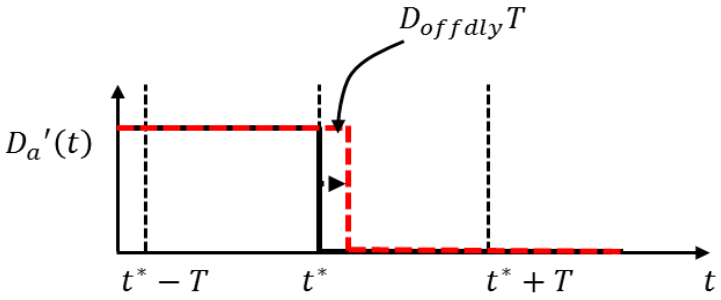

(b) Consecutive command pair (1, 0)

Figure 8.5 Terminal voltage estimation when current flows outward

On the other hand, if the command transits from high to low, the current flow will switch from the upper to the lower path when the upper IGBT is turned off. Since the closing edge of the actual $D'_a(t)$ is not affected by the dead time, only the communication delay $D_{offdly}T$ needs to be considered, as shown in Figure 8.5 (b).

In the case where the phase *a* current i_{sa} is flowing inwards, as shown in Figure 8.6, the current switches from the low-voltage path to the high-voltage path once the lower IGBT is turned off; therefore the rising edge of $D'_a(t)$ is only delayed by $D_{offdly}T$, which is illustrated in Figure 8.7(a).

On the other hand, the phase *a* current flow will switch from the high voltage path to the low voltage path only after the lower IBGT is turned on; that means the falling edge of $D'_a(t)$ gets delayed by the specified dead time $D_{dt}T$, as well as $D_{ondly}T$, as shown in Figure 8.7(b).

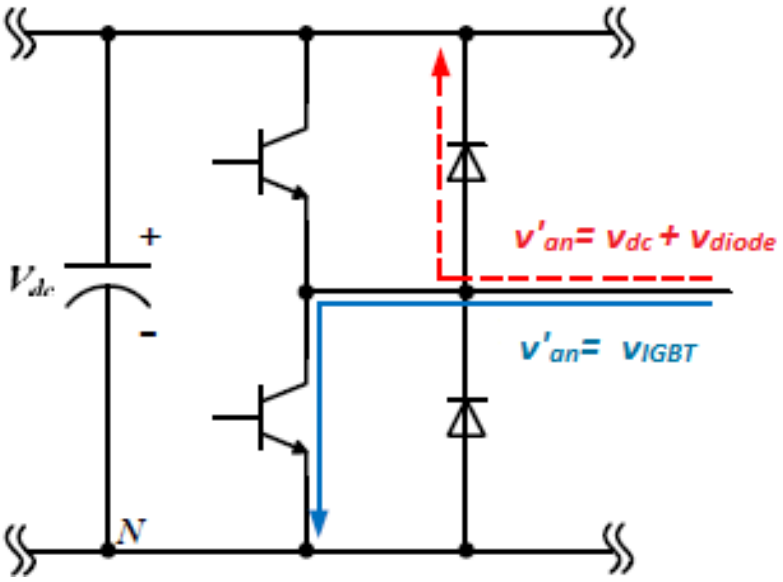

Figure 8.6 Phase *a* current flows inward

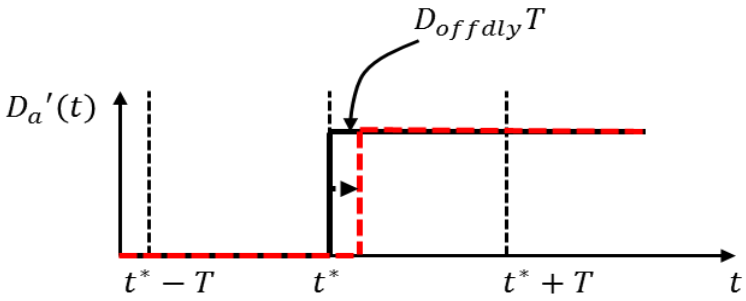

(a) consecutive command pair (0, 1)

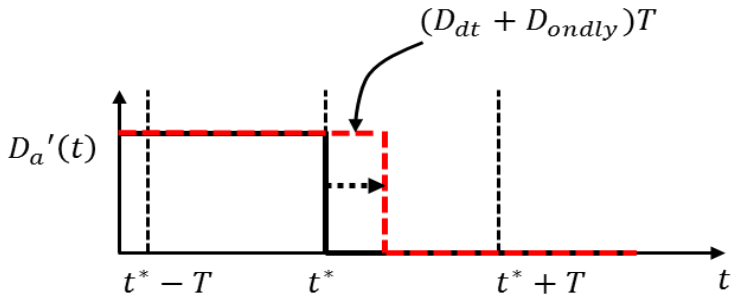

(b) consecutive command pair (1, 0)

Figure 8.7 Terminal voltage estimation when current flows inward

In summary, the impact of dead-time delay and switch turn-on/turn-off delays on the duty ratio for the selected phase *a* is presented as follows:

If $i_{sa} > 0$

$$\left.\begin{aligned} &D_a(t^* - T) = 0, D_a(t^*) = 1 \Rightarrow D_a'(t^*) = D_a(t^*) - D_{dt} - D_{ondly} \\ &D_a(t^* - T) = 1, D_a(t^*) = 0 \Rightarrow D_a'(t^*) = D_a(t^*) + D_{offdly} \end{aligned}\right\} \quad (8.4)$$

If $i_{sa} < 0$

$$\left.\begin{aligned} &D_a(t^* - T) = 0, D_a(t^*) = 1 \Rightarrow D_a'(t^*) = D_a(t^*) - D_{offdly} \\ &D_a(t^* - T) = 1, D_a(t^*) = 0 \Rightarrow D_a'(t^*) = D_a(t^*) + D_{dt} + D_{ondly} \end{aligned}\right\} \quad (8.5)$$

Note that equations (8.4) and (8.5) are true only for the particular DTC scheme and gate-signal generation logic implemented for the particular hardware system setup. For alternative DTC and gate signal implementations, the same inverter non-idealities need to be considered, but equations (8.4) and (8.5) may need to be adjusted slightly.

8.3.1.2 Terminal-voltage estimation compensation

While the current i_{sa} is flowing outwards, as shown in Figure 8.4, the voltage drops across the IGBT and diode reduce the terminal voltage. If the IGBT switch is fully turned on, the terminal voltage is $[V_{dc} - v_{IGBT}(i_{sa})]$ instead of V_{dc}; if the switch is completely turned off, the terminal voltage is $[-v_{diode}(i_{sa})]$ rather than zero. The resultant average terminal voltage for phase *a* within one cycle is derived in equation (8.6).

While the current i_{sa} is flowing in the opposite direction, as illustrated in Figure 8.6, the voltage drop across the upper diode, will increase the terminal voltage from V_{dc} to $[V_{dc} + v_{diode}(i_{sa})]$ when the IGBT switch is fully turned off; and the voltage drop across the lower IGBT will also increase the terminal voltage from zero to $v_{IGBT}(i_{sa})$ when the IGBT switch is fully turned on. The resultant average terminal voltage for phase *a* within any cycle can be expressed in equation (8.7).

If $i_{sa} > 0$

$$v'_{an} = D'_a[V_{dc} - v_{IGBT}(i_{sa})] + (1 - D'_a)[-v_{diode}(i_{sa})] \tag{8.6}$$

If $i_{sa} < 0$

$$v'_{an} = D'_a[V_{dc} + v_{diode}(i_{sa})] + (1 - D'_a)[v_{IGBT}(i_{sa})] \tag{8.7}$$

Strictly speaking, voltage drops across the IGBTs and diodes also depend on the device temperature, aside from the current flowing through them. However, such dependency is low enough so that its effect on terminal voltage estimation can be neglected [48, 49].

The actual duty ratios and terminal voltages for phase *b* and phase *c* respectively have similar forms to equations (8.4) - (8.7) for phase *a*.

8.3.1.3 Additional signal-processing techniques

Once accurate three-phase terminal voltage and current estimation are obtained via the proposed scheme in sections 8.3.1.1 and 8.3.1.2, two second-order cascaded low pass filters (LPFs) are implemented to extract the corresponding DC components respectively.

Each of the estimated quantities goes through a first-level second-order LPF; then these quantities are down-sampled by a given ratio; the down-sampled data then passes through a second-level second-order LPF. The cascaded filtering process significantly eliminates the fundamental frequency components and extracts the DC components.

It is also worth mentioning that although the DC current offset is small, the proposed method is robust to most sources of current sensor inaccuracies. The method is not sensitive to current (or voltage) sensor gain errors because the same sensors are used for calibrating the stator resistance R_b at room temperature t_b. Moreover, the method is not sensitive to current (or voltage) sensor DC offset errors. This is because in the hardware test, a *differential current/voltage measurement scheme* is practically implemented. The injection method in DTC system is taken as an example, and is briefly explained as follows.

In a DTC system, each injection period contains two steps: the injection command for the first step is $\left[+\left[\frac{\Delta T_{em,ref}}{\overrightarrow{\Delta \Psi_{s,ref}}}\right]\right]$, while the injection command for the second step is always the opposite $\left[-\left[\frac{\Delta T_{em,ref}}{\overrightarrow{\Delta \Psi_{s,ref}}}\right]\right]$. It is the current and voltage differences between the two injection steps that are eventually utilized to obtain the injected DC-signal level. Therefore, any DC offset errors associated with the sensor are cancelled out in this process. Its accuracy is clearly illustrated in the comparison of the experimental temperature results between the estimated and direct-measured data in section 8.5.

8.3.2 Improved signal processing techniques for an FOC drive

Considering the inverter non-idealities in an FOC system, such as the dead time, the switching device voltage drop, and the different turn-on/off time delay, the terminal voltage estimation method is modified in a similar way. It is summarized as follows [48, 49]:

If $i_{sa} > 0$

$$v'_{an} = \left(D_a - D_{dt} + D_{offdly} - D_{ondly}\right)[V_{dc} - V_{IBGT}(i_a)]$$

$$-\left(1 - D_a + D_{dt} - D_{offdly} + D_{ondly}\right)v_{diode}(i_{sa}) \tag{8.8}$$

If $i_{sa} < 0$

$$v'_{an} = \left(D_a + D_{dt} - D_{offdly} + D_{ondly}\right)[V_{dc} + V_{diode}(i_a)]$$

$$+\left(1 - D_a - D_{dt} + D_{offdly} - D_{ondly}\right)v_{IGBT}(i_{sa}) \tag{8.9}$$

The actual three-phase voltages for phases *b* and *c* respectively have similar forms to equations (8.8) - (8.9) for phase *a*.

In general, the major difference of the terminal voltage estimation between an FOC and DTC system is that the former estimation method generally does not depends on the previous state of the command, but not the latter one. However, if over-modulation or discontinuous PWM method is applied to an FOC scheme, it is possible for the commanded duty cycle D_a to be clamped to either 0 or 1; therefore, both the present and previous state of the duty ratio commands need to be used to obtain the actual duty ratios, similar to equation sets (8.4) – (8.5) in a typical DTC scheme.

8.4 HARDWARE SYSTEM SETUP

A closed-loop adjustable-speed induction machine drive system in the Intelligent Power Infrastructure Consortium (IPIC) laboratory is used to verify the proposed signal-injection method and the corresponding thermal-monitoring scheme.

As shown in Figure 8.8, the test motor is a commercial 5-hp squirrel-cage induction machine. The parameter set for the test induction machine appears in Table 8.1. A few thermocouples are attached to different parts of the motor stator windings, and the average measured result is used for validation.

The test motor is driving a DC dynamometer, and the generated electric power from the DC machine is consumed by a set of resistor banks.

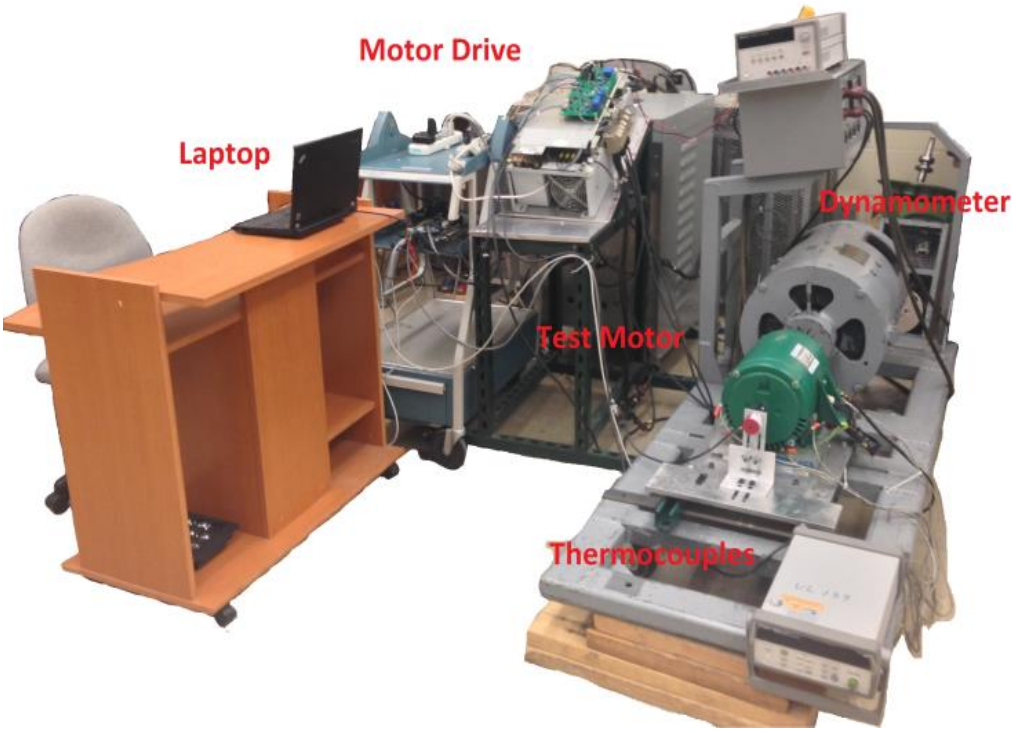

Figure 8.8 Experimental setup

Table 8.1 Parameter table of the test induction machine (experiment)

Rated power	5 hp	*Poles*	4
Rated voltage	230 V	Rated current	13 A
Rated speed	1745 rpm	R_s	0.3584 Ω
R_r	0.4211Ω	L_m	0.06746 H
L_{ls}	0.00255 H	L_{lr}	0.00383 H

The test motor is controlled by a custom-built programmable motor drive, as shown in Figure 8.9. The drive system has a standard setup of the power stage, including a front-end three-phase rectifier, a DC-link capacitor, a choker inductor, and three IGBT bridges. The control architecture contains an ADSP 21369 evaluation board (include a high-performance 32-bit floating-point SHARC processor) for main processing purpose, a Xilinx Spartan-3 FPGA board as the data interface, a 3-channel 12-bit A/D sensor board, as well as a gate-drive board to drive the IGBT bridges. Optic fiber is used for data communication [48, 49].

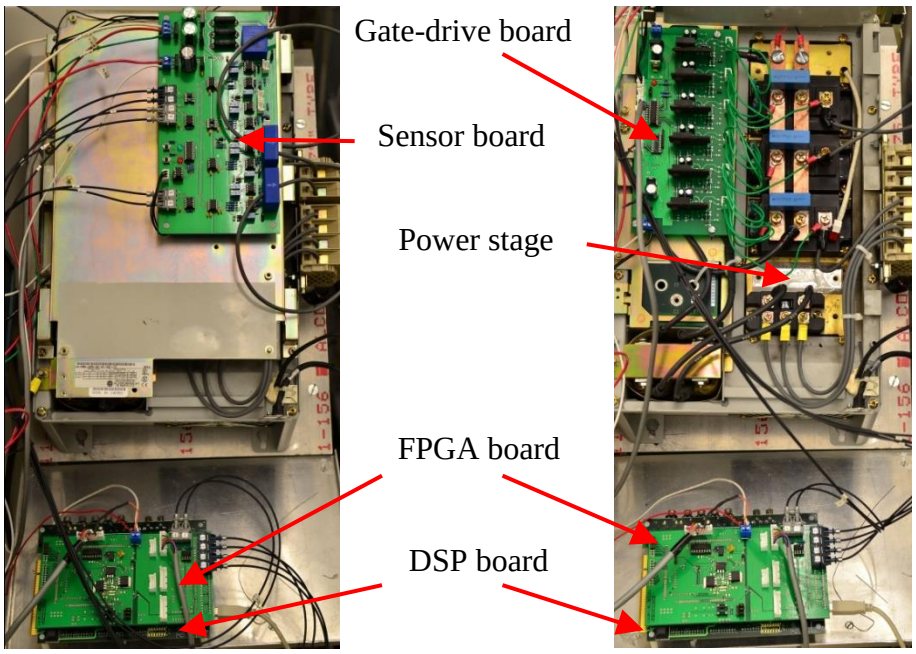

(a) Inverter with top cover (b) Inverter without top cover

Figure 8.9 Self-built programmable motor drive.

8.5 EXPERIMENTAL VALIDATION

The proposed various types of DC-signal injection-based thermal monitoring scheme are integrated in real time in either DTC or FOC algorithm on this custom-built programmable motor test rig.

Since the temperature varies slowly in a typical motor, the signal-injection method is, for practical implementation, intermittently integrated in the conventional DTC/FOC algorithms; say for a period of 20 seconds every 10 minutes, to provide the thermal monitoring data. As a result, the impact of the injection method on motor normal operation is further limited, while it can still guarantee accurate temperature monitoring results.

8.5.1 DTC experimental results

8.5.1.1 Flux-linkage-injection method

The three-phase stator-current waveforms using the flux-linkage-injection method are shown in Figure 8.10, with injection at t = 10 s. It can be directly observed that the stator current obtain an offset as soon as the flux linkage is injected at t = 10 s; the current bias for each phase increases exponentially as anticipated, and reaches the steady state constant value after approximately 0.4 s. Thus, the proposed flux-linkage-injection method is able to excite a proper amount of DC currents, and can be further used for stator-winding resistance and stator-winding temperature estimation.

In addition, the DC component of phase a voltage $V_{a'dc}$ and current bias I_{sadc} are also plotted in Figure 8.11. The injected DC current for phase a is only about 0.7 A, or 3.763%

of the rated current amplitude. Therefore, the cascaded LPF technique is proved to be able to extract the required DC components for both the stator current and voltage.

The estimated torque T_{em} is plotted in Figure 8.12. It is observed that there is no noticeable torque ripple after the injection is implemented at t >10 s. Considering the fact that the bias is only enforced for a few seconds every 10 minutes, the above results prove that this technique has a minimal impact on the machine's normal operation.

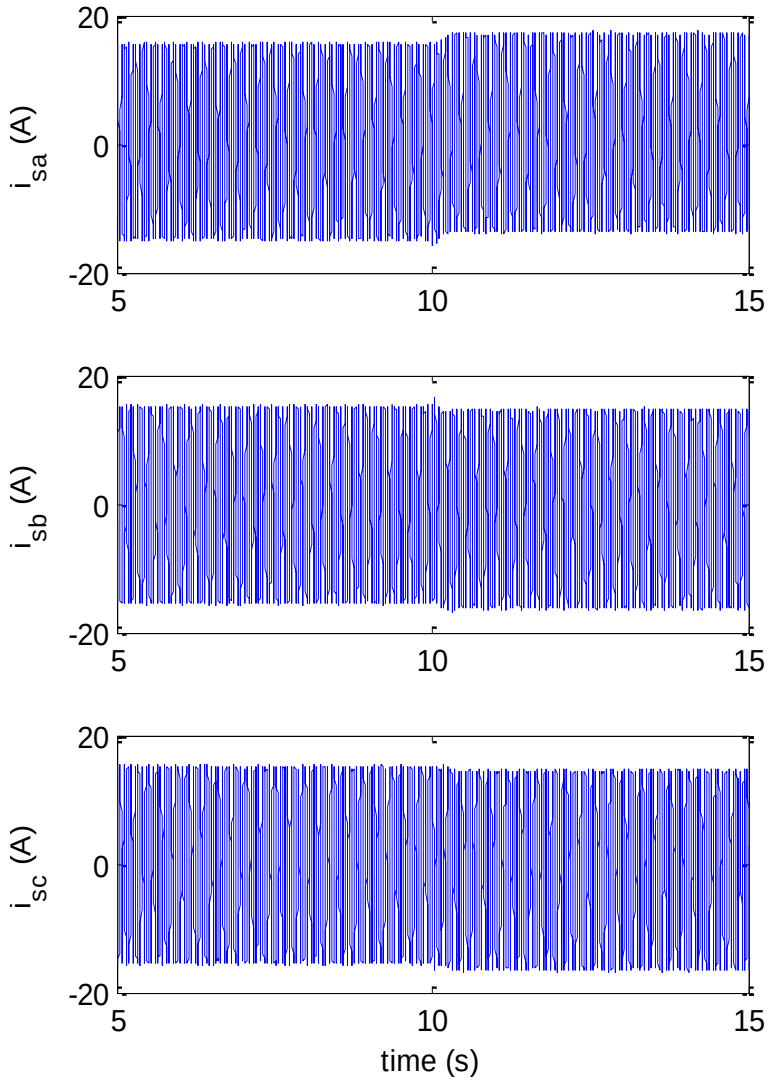

Figure 8.10 Stator current waveforms, with flux-linkage injection t > 10 s

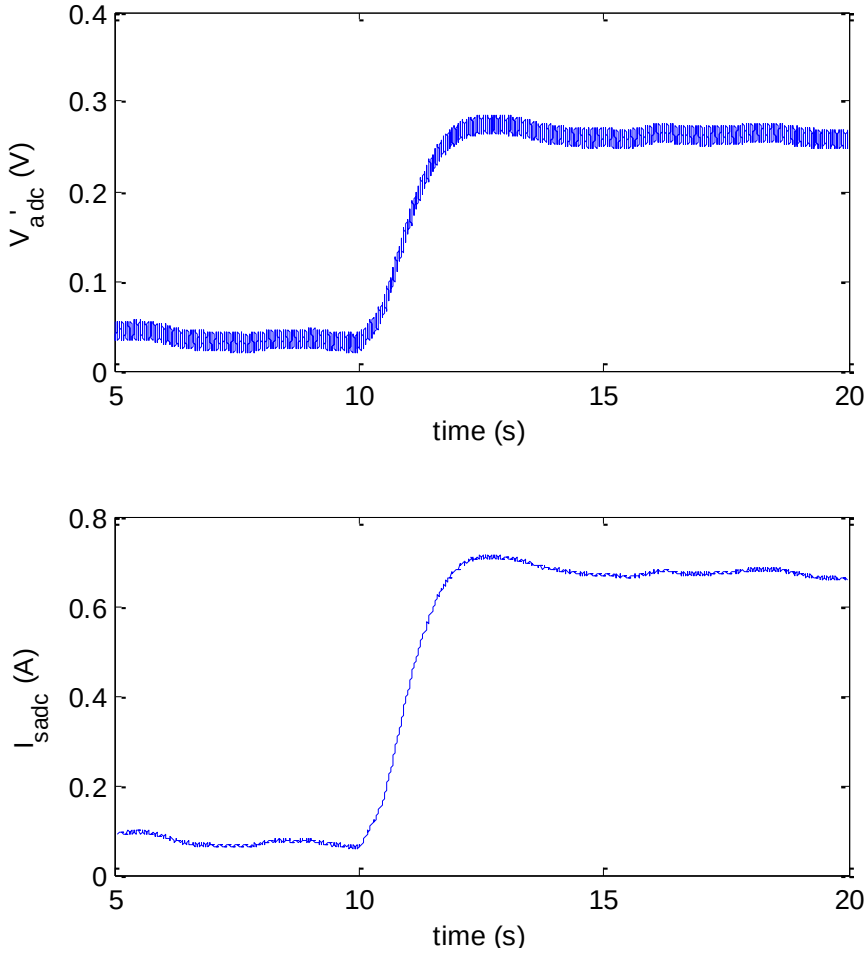

Figure 8.11 Phase-*a* DC voltage and current, with flux-linkage injection $t > 10$ s

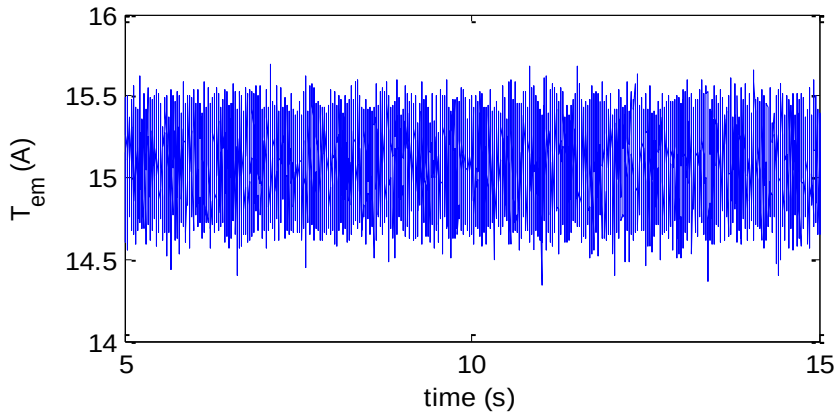

Figure 8.12 Estimated torque, with flux-linkage injection $t > 10$ s

Three cases in Figure 8.13 (a) – (c) illustrate the temperature tracking results at different running conditions or cooling modes using the flux linkage injection method. In Figure 8.13 (a), the motor is running at 80% rated load and roughly 480 rpm. The temperature is estimated right from startup for 100 minutes. In Figure 8.13 (b), the machine is still running at 80% rated condition and roughly 480 rpm; however, an insulation jacket is wrapped around the machine. Therefore, the cooling condition is different from the previous case and the temperature increases much faster than before. In Figure 8.13 (c), the motor is originally running at 60% of the rated torque and roughly 360 rpm; at 80 minutes, there is a sudden torque increase to 80% of the rated torque load and roughly 480 rpm. There is no insulation jacket wrapped around the machine.

It is observed from the three different cases in Figure 8.13 that, the temperature tracking results under different operating conditions agree well with the measured results from thermocouples, with the maximum difference around 2~3% at most.

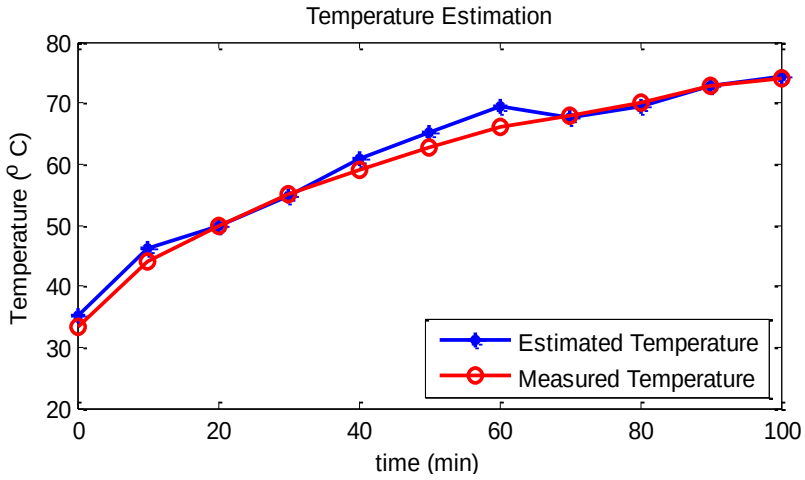

(a) IM running at 80% rated load

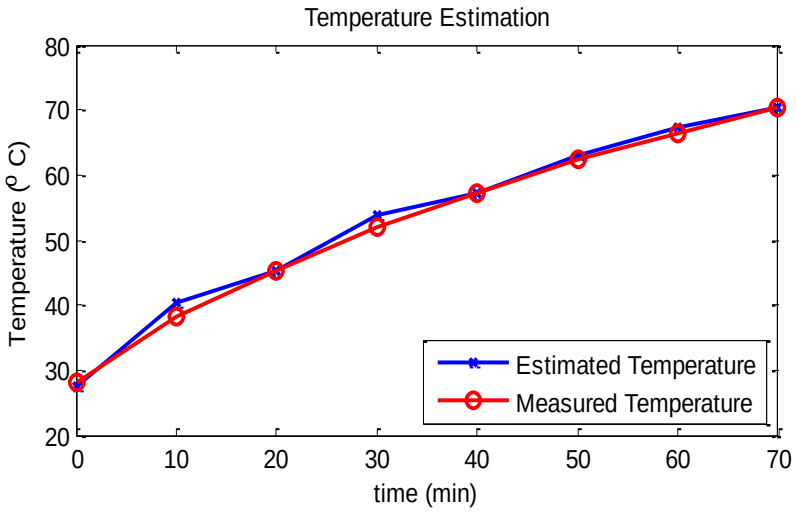

(b) IM running at 80% rated load (with insulation jacket)

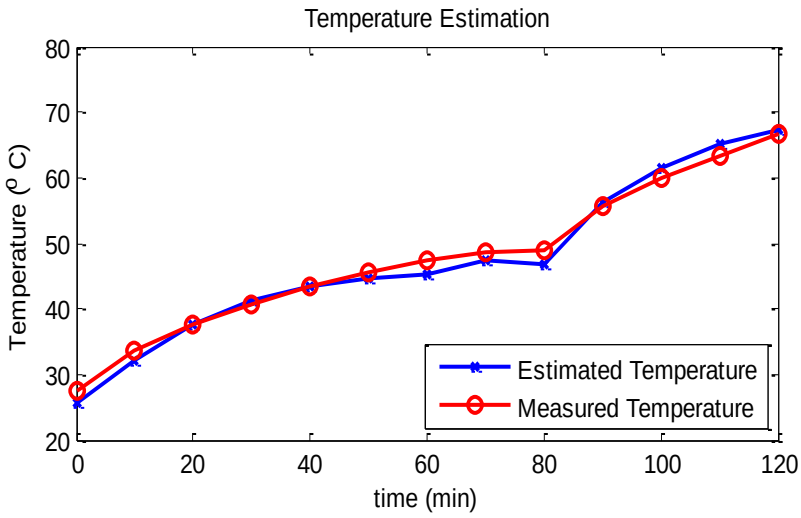

(c) IM with a sudden torque change from 60% to 80% rated load at 80 minutes (no insulation jacket)

Figure 8.13 Temperature tracking results (flux-linkage injection for DTC IMs)

8.5.1.2 Torque-injection method

The phase *a* current and voltage waveforms at the beginning of one injection period via the torque-injection method are shown in Figure 8.14, while the corresponding extracted DC quantities are displayed in Figure 8.15.

From Figure 8.14, screen capture of the oscilloscope, it can be directly observed that the stator current is effectively offset under the torque-injection method but not the phase voltage, because the terminal voltage is generated by PWM gate signals, and contain rich switching harmonics.

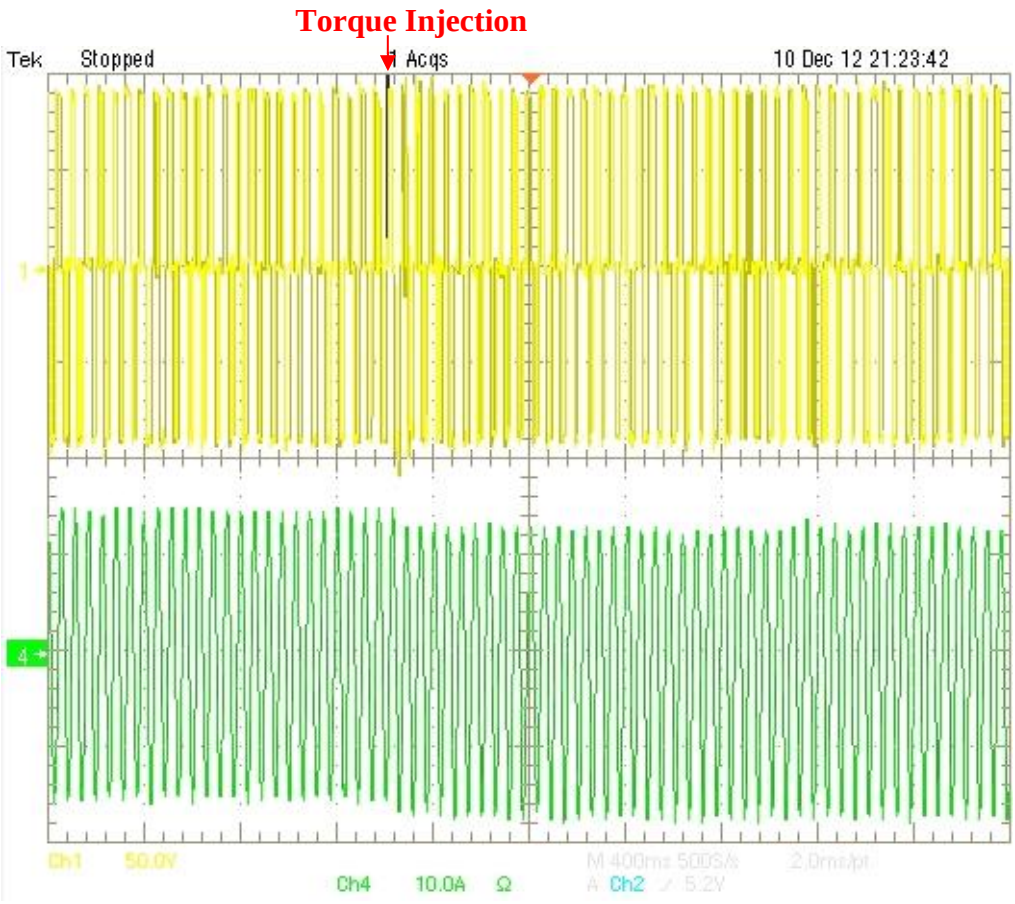

Figure 8.14 Phase *a* stator voltage (upper waveform) and current (lower waveform), with torque injection $t > 10$ s

Similarly to the results for the flux-linkage-injection method, it is shown in Figure 8.15 that the injected DC current for phase *a* is obtained from the cascaded LPFs and has a steady-state value of about 0.8 A, 4.3% of the rated current amplitude. Considering the fact that the bias is only enforced for a few seconds every 10 minutes, this technique also has little impact on the machine's normal operation.

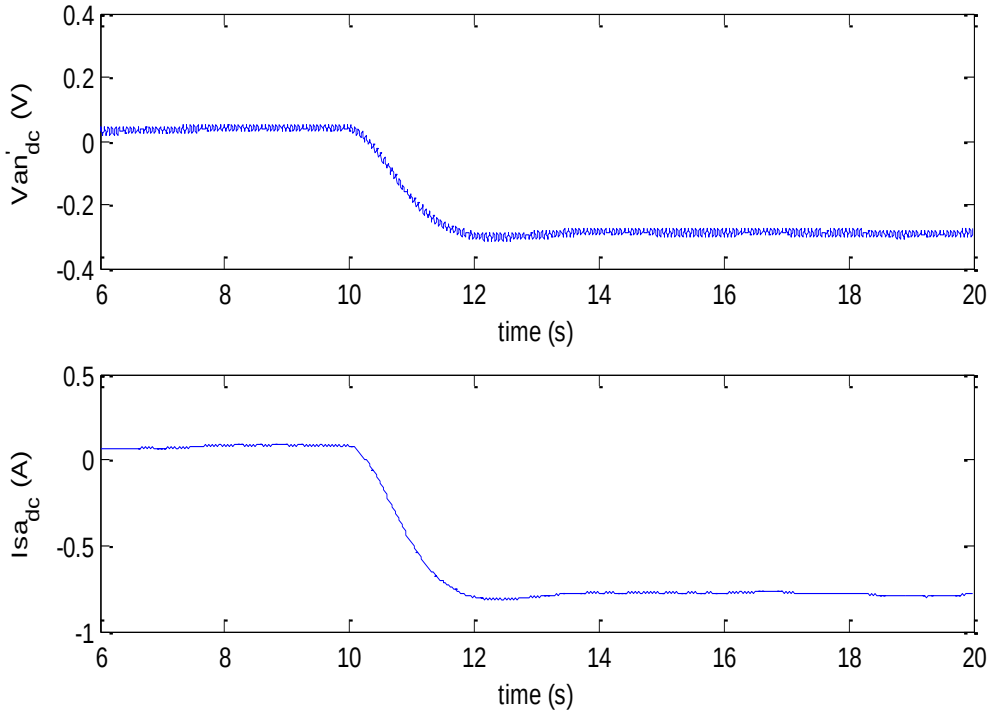

Figure 8.15 Phase *a* DC voltage and current, with torque injection $t > 10$ s

The three cases in Figure 8.16 (a) - (c) are the tracking results using the torque-ripple injection method at different operating conditions and cooling modes [71]. The load level and cooling modes for Figure 8.16 (a) and Figure 8.16 (b) are the same as those for Figure 8.13 (a) and (b) respectively. The running condition in Figure 8.16 (c) is different

from that in Figure 8.13(c): there is a sudden load torque change at 100 minutes, while the insulation jacket remains wrapped around all the time.

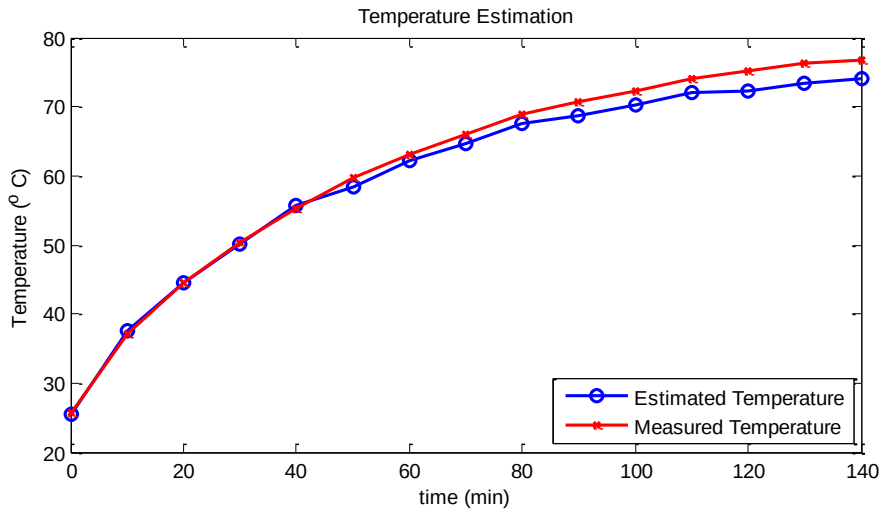

(a) IM running at 80% rated load

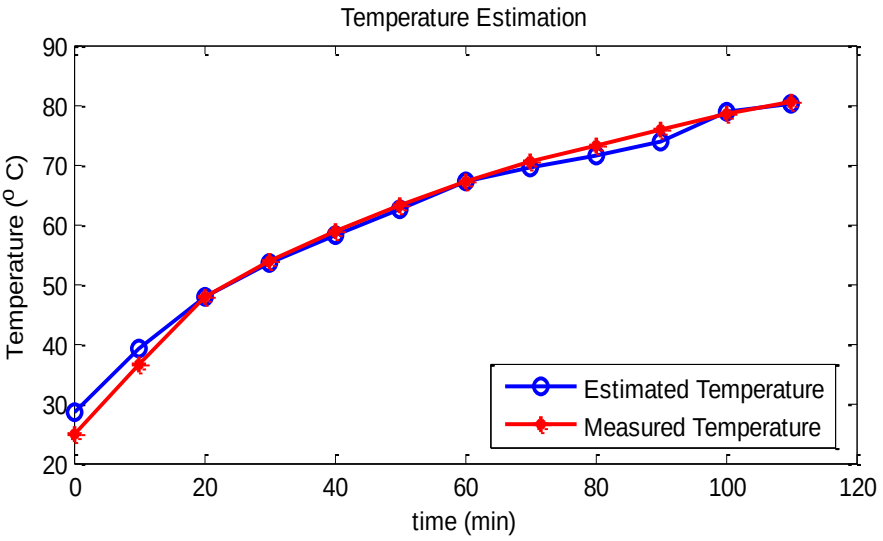

(b) IM running at 80% rated load (with insulation jacket)

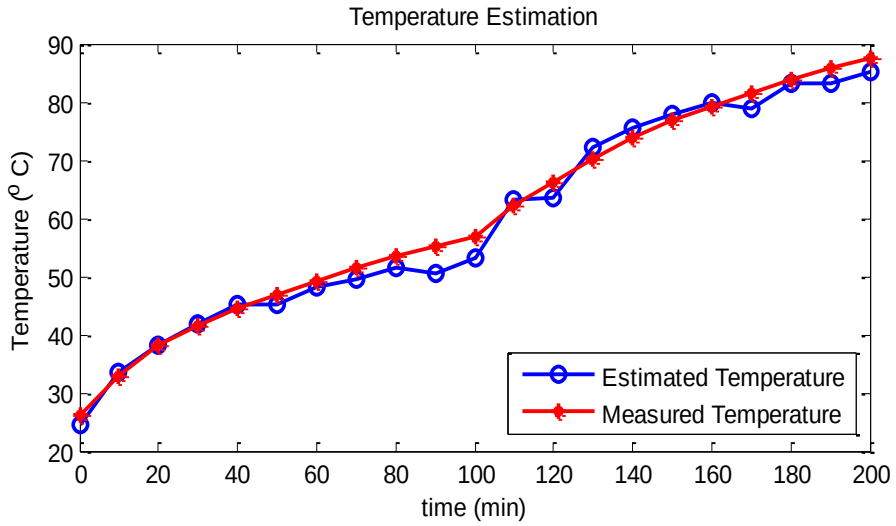

(c) IM with a sudden torque change from 60% to 80% rated load at 80 minutes (with insulation jacket)

Figure 8.16 Temperature tracking results (torque injection for DTC IMs)

8.5.2 FOC experimental Results

Figure 8.17 presents the stator current waveforms before and after the proposed injection method is commanded. The *d*-axis current waveform contains visible fundamental-frequency ripple after injection, while *q*-axis has unnoticeable low-frequency oscillation after injections. Considering the improved FOC injection method has a form of current command as $\left(\Delta i^e_{sd,ref}, \Delta i^e_{sq,ref}\right)^T = (M\cos(\omega_s t), 0)^T$, the results in Figure 8.17 agree well with the anticipated.

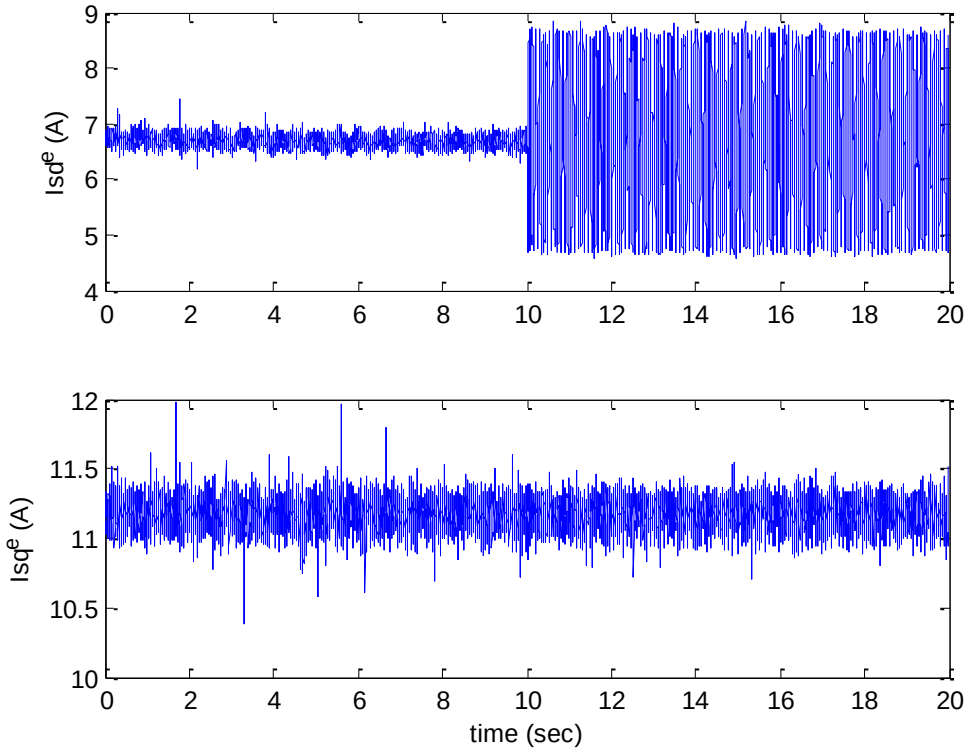

Figure 8.17 *dq* current, with the improved FOC injection method $t > 10$ s.

The temperature tracking results at two different loading conditions is shown in Figure 8.18. At the beginning, the motor is running at 30% of the rated load; after 80 minutes, there is a sudden load torque increase to 70% of the rated torque. The temperature tracking results under the two different operating conditions agree well with the measured results from thermocouples, with the maximum difference less than 3.5 ℃.

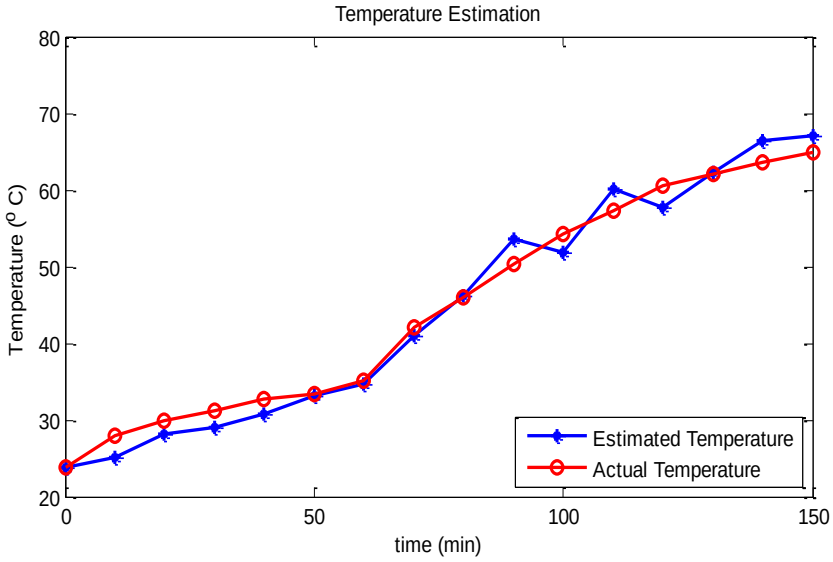

Figure 8.18 Temperature Tracking for the improved FOC current injection.

8.6 CHAPTER SUMMARY

This chapter presents an injection-based thermal monitoring scheme for inverter-fed induction machine, where the stator winding resistance is used as a direct indicator of the winding temperature. This monitoring scheme is based on the various types of advanced injection method proposed for direct-torque-control (DTC) scheme in Chapter 6 (active flux injection method and active torque injection) and field-oriented-control (FOC) scheme in Chapter 7 (an improved active current injection method with torque ripple mitigation).

This thermal monitoring technique is easy to implement and of very low cost, because it eliminates the need for thermocouples and require no hardware adjustment to the existing standard and commercial drive systems. This is especially beneficial to low-to-medium horse-power electric machines.

It is also validated by hardware tests that the proposed thermal-monitoring method provides accurate temperature estimation results under various motor operating conditions and cooling modes.

In addition, these injection techniques are proved to be noninvasive since they have minimal impacts on the machines' normal operating conditions.

To summarize, the proposed various types of advanced injection-based thermal-monitoring technique are proved to be simple, low cost, accurate, and non-invasive. These methods can be widely used to protect the machine from overheating, insulation degradation, and improve the overall system's control performance.

CHAPTER 9 CONCLUSIONS AND CONTRIBUTIONS

9.1 INTRODUCTION

This chapter concludes this dissertation by first reviewing the objective of this research and proposed solution framework, summarizing the technical development and major contributions of Chapter 4 - Chapter 8 , and finally presenting the list of outcomes such as journal papers, and conference papers directly related to this dissertation.

In addition, section 9.5 presents several future research directions that can extend the scope of the dissertation.

9.2 CONCLUSIONS OF THIS DISSERTATION

The objective of the dissertation is to develop simplified analytical models for typical linear-motion and rotary-motion energy-conversion systems under active DC excitation without tedious numerical-simulation effort, and provide practical implementation of the models in optimal-design and thermal-protection aspects.

In Chapter 4 and Chapter 5 the model of a vacuum automatic circuit recloser (a typical linear-motion system under DC excitation) is first developed in the form of a non-linear discontinuous eighth-order dynamic system. The model is then used to simulate the transient mechanical and electromagnetic performance during the opening and closing movements of the recloser.

Although the model is based on certain simplifying assumptions, the result is validated by high-speed-camera measurements. In addition, the impact of key design variables is explored, based on which an improved recloser design is proposed, and helps to optimize capital and production costs without degrading performance.

In Chapter 6 and Chapter 7 further analytical investigations are carried out by modeling an inverter-fed induction motor (IM) (a typical rotary-motion system) with active DC injection. The IM is closed-loop controlled via two popular motor-control algorithms, namely, the direct-torque-control (DTC) algorithm and field-oriented-control (FOC) algorithm. Quantitative relationships between the changes of various machine variables during the active DC excitation are provided in the theoretical analysis.

The developed DC-injection model is further simplified for practical implementation. The developed IM model under DC injection results in practical ways to excite a proper amount of DC current directly or indirectly into IM stator windings via different closed-loop motor-control algorithms. In a DTC motor-drive system, the modeling work makes it possible to excite the DC current indirectly inside the motor by superimposing a stator-flux-linkage-bias command in the flux-control loop or a torque-ripple command in the torque-control loop. In addition, the analysis carried out in a standard FOC drive system brings about an improved DC-current-injection approach: the torque ripple in this method is significantly mitigated compared to all existing DC-injection methods in FOC systems.

In Chapter 8 the proposed DC-injection methods, either in a DTC or an FOC system, lead to a simple, low-cost, accurate, and non-invasive thermal-monitoring scheme for closed-loop-controlled IMs, where the stator temperature is indirectly estimated from stator resistance.

9.3 CONTRIBUTION OF THIS DISSERTATION

The main contributions of this dissertation are summarized as follows:

(1) The multi-physics model of a vacuum automatic recloser is developed in the form of a non-linear discontinuous eighth-order dynamic system. The model is used to describe the

mechanical and electromagnetic transient responses of the linear-motion relcoser system during the roundtrip motion. Such a model is not found in literature.

(2) Based on the DC-signal injection modelling work carried out for a DTC motor drive system, two active injection methods are proposed so as to indirectly excite the desired DC current in the motor winding by superimposing a stator-flux-linkage-bias command in the flux-control loop or a torque-ripple command in the torque-control loop. The proposed flux-linkage-injection and torque-injection methods are the first novel efforts to implement the DC-signal-injection method in a DTC motor-drive system.

(3) An improved current-injection method with active torque mitigation is proposed for an FOC system. With this improved injection technique, the induced synchronous-speed torque ripple, which is conventionally a major disadvantage for DC-signal-injection methods [51, 52, 73], is effectively mitigated with the added second-order harmonic currents, while the DC-current injection level maintains the same.

(4) The proposed enhanced injection method in DTC and FOC system leads to an injection-based thermal monitoring scheme, which is proved to be simple, low cost, accurate, and non-invasive.

Simple and low cost: This thermal monitoring technique is easy to implement and of very low cost, because it eliminates the need for thermocouples and require no hardware adjustment to the existing standard and commercial drive systems. This is especially beneficial to low-to-medium horse-power electric machines.

Accurate: the proposed thermal-monitoring method provides accurate temperature estimation results under various motor operating conditions and cooling modes.

Non-invasive: the injection technique is proved to be noninvasive since they eliminate the need for additional sensors, require no hardware changes to existing drive systems, and have minimal impacts on the machines' normal operating conditions.

(5) Considering inverter non-idealities, there is a challenge for a typical inverter drive to accurately estimate the DC component of motor terminal voltages. The existing methods are extended to provide a complete study of the real-time signal-processing technique for both DTC and FOC algorithms, and are finally implemented in a custom-built programmable motor-drive system.

9.4 OUTCOMES OF THIS DISSERTATION

The literature review and research work presented in Chapter 2 - Chapter 8 of this dissertation have resulted in a number of publications, listed as follows:

9.4.1 Journal papers

[1] **Lijun He**, J. Rhett Mayor, Ronald G. Harley, Howard Liles, Guangcong Zhang, Yi Deng, "Multi-physics modeling of the dynamic response of a circuit breaker recloser system," IEEE Transactions on Industry Applications, vol.50, no.6, pp.3697-3707, Nov.-Dec. 2014

[2] **Lijun He**, Siwei Cheng, Yi Du, Ronald G. Harley, and Thomas G. Habetler, "Stator Temperature Estimation of Direct-Torque-Controlled Induction Machines via Active Flux or Torque Injection," IEEE Transactions on Power Electronics, vol.30, no.2, pp.888-899, Feb. 2015

[3] **Lijun He**, Jose Restrepo, Siwei Cheng, Ronald G. Harley, and Thomas G. Habetler, "An Improved DC-Signal-Injection Method with Active Torque-Ripple

Mitigation for Thermal Monitoring of Field-Oriented-Controlled Induction Motors", IEEE Transactions on Industry Applications (in preparation)

9.4.2 Conference papers

[1] **Lijun He**, Siwei Cheng, Ronald G. Harley, and Thomas G. Habetler, "A torque-injection-based approach for thermal monitoring of induction machines with direct torque control," in Electric Machines & Drives Conference (IEMDC), 2013 IEEE International, 2013, pp. 93-99, 12-15 May 2013

[2] **Lijun He**, J. Rhett Mayor, Ronald G. Harley, Howard Liles, Guangcong Zhang, Yi Deng, "Multi-physics modeling of the dynamic response of a circuit breaker recloser system," in Electric Machines & Drives Conference (IEMDC), 2013 IEEE International, 2013, pp. 1001-1008, 12-15 May 2013

[3] **Lijun He**, Siwei Cheng, Yi Du, Ronald G. Harley, and Thomas G. Habetler, "A DC-flux-injection approach for thermal monitoring of induction machines with direct torque control," in Energy Conversion Congress and Exposition (ECCE), 2013 IEEE, 2013, pp. 2115-2122, 15-19 Sept. 2013

[4] **Lijun He**, Jose Restrepo, Siwei Cheng, Ronald G. Harley, and Thomas G. Habetler, "An Improved DC-Signal-Injection Method with Active Torque-Ripple Mitigation for Thermal Monitoring of Field-Oriented-Controlled Induction Motors", in Energy Conversion Congress and Exposition (ECCE), 2015 IEEE

9.4.3 Other contributions

The following journal and conference papers, as outcomes of class projects have also been published.

[1] **Lijun He**, Yongdong Li, and Ronald G. Harley, "Novel Adaptive Power Control of a Direct-drive PM Wind Generation System in a Micro Grid," in Power Electronics and Machines in Wind Applications (PEMWA), 2012 IEEE, pp. 1-8, 16-18 July 2012

[2] Liang Du, **Lijun He**, and Ronald G. Harley, "A survey of methods for placing shunt capacitor banks in power network with harmonic distortion," in IECON 2012 - 38th Annual Conference on IEEE Industrial Electronics Society, 2012, pp. 1198-1203, pp. 25-28, Oct. 2012.

[3] **Lijun He**, Yongdong Li, and Ronald G. Harley, "Adaptive Multi-Mode Power Control of a Direct-Drive PM Wind Generation System in a Microgrid," IEEE Journal of Emerging and Selected Topics in Power Electronics, vol.1, no.4, pp.217-225, Dec. 2013

9.5 FUTURE WORK

9.5.1 Multi-objective recloser design

The preliminary design work in section 5.4 only considered the key parameters of capacitor voltages and PM remanence, to reduce the system's cost and enhance the opening and closing performance. A more detailed optimal design process could be carried out in future using various stochastic optimization methods, where more design

parameters, like geometric dimension, mass and spring stiffness, could also be considered with detailed material cost values.

9.5.2 Integrate recloser model with power-system simulation tool

This detailed dynamic recloser model could be integrated with other power-system simulation tools to examine and limit any deleterious interaction effects of recloser operation on the rest of the power system. The modeling work could assist the coordination of the recloser with other protection devices.

9.5.3 Extend the improved signal-processing technique to other DTC/FOC schemes

The improved signal-processing techniques discussed in section 8.3 can only be applied to the particular DTC scheme and gate signal generation logic implemented for the particular hardware system setup. It could be extended to alternative DTC and gate signal implementations; the same inverter non-idealities need to be considered, but equations (8.4) and (8.5) may need to be adjusted slightly.

In addition, if over-modulation or discontinuous PWM method were applied to an FOC scheme, the commanded duty cycle D_a could be clamped to either 0 or 1; therefore, both the present and previous state of the duty ratio commands should be used to obtain the actual duty ratios, similar to the technique described for a typical DTC scheme in section 8.3.

9.5.4 Explore the impacts of second harmonics on torque-ripple mitigation caused by DC injection

As observed in Chapter 7 , the magnitudes of the injected DC and second-harmonic currents in this improved method are exactly the same. It is recommended in the future to

carry out a sensitivity study and explore the impacts of various amounts of injected second harmonic currents on mitigating the fundamental-frequency torque ripple caused by DC injection.

BIBLIOGRAPHY

[1] "IEEE guide for automatic reclosing of circuit breakers for AC distribution and transmission lines," *IEEE Std C37.104-2012 (Revision of IEEE Std C37.104-2002)*, pp. 1-72, 2012.

[2] H. K. Karegar and S. Saberi, "Investigating of wind turbines affects on recloser operation in distribution networks," in *Power and Energy (PECon), 2010 IEEE International Conference on*, 2010, pp. 523-526.

[3] G. G. Auer, R. A. Branflick, L. J. Woodward, and W. C. McKinley, "Field tests of oil circuit recloser substantiate analytical co-ordination method," *Trans. Amer. Inst. Elect. Eng.*, vol. 68, pp. 801-810, 1949.

[4] G. G. Auer, R. A. Branflick, L. J. Woodward, and W. C. McKinley, "Recloser-fuse co-ordination," *Elect. Eng.*, vol. 68, pp. 864-864, 1949.

[5] S. D. Hu, Z. M. Zhao, H. Bai, and L. Q. Yuan, "An Enhanced DC Preexcitation With Effective Flux-Linkage Control for the High-Power Induction Motor Drive System," *IEEE Trans. Power Electron.* , vol. 26, pp. 2375-2380, Sep 2011.

[6] L. He, Y. Li, and R. Harley, "Novel adaptive power control of a Direct-drive PM wind generation system in a micro grid," in *Power Electronics and Machines in Wind Applications (PEMWA), 2012 IEEE*, 2012, pp. 1-8.

[7] L. He, Y. Li, and R. G. Harley, "Adaptive Multi-Mode Power Control of a Direct-Drive PM Wind Generation System in a Microgrid," *IEEE Journal of Emerging and Selected Topics in Power Electronics*, vol. 1, pp. 217-225, 2013.

[8] J. Liang, W. Qiao, and R. G. Harley, "Feed-Forward Transient Current Control for Low-Voltage Ride-Through Enhancement of DFIG Wind Turbines," *IEEE Trans. Energy Convers.*, vol. 25, pp. 836-843, 2010.

[9] C. Patel, R. P. P. A. Day, A. Dey, R. Ramchand, K. Gopakumar, and M. P. Kazmierkowski, "Fast Direct Torque Control of an Open-End Induction Motor Drive Using 12-Sided Polygonal Voltage Space Vectors," *IEEE Trans. Power Electron.* , vol. 27, pp. 400-410, 2012.

[10] A. Taheri, A. Rahmati, and S. Kaboli, "Efficiency Improvement in DTC of Six-Phase Induction Machine by Adaptive Gradient Descent of Flux," *IEEE Trans. Power Electron.* , vol. 27, pp. 1552-1562, 2012.

[11] A. B. Jidin, N. R. B. N. Idris, A. H. B. M. Yatim, M. E. Elbuluk, and T. Sutikno, "A Wide-Speed High Torque Capability Utilizing Overmodulation Strategy in DTC of Induction Machines With Constant Switching Frequency Controller," *IEEE Trans. Power Electron.* , vol. 27, pp. 2566-2575, 2012.

[12] D. Casadei, G. Serra, A. Tani, and L. Zarri, "Direct Torque Control for induction machines: A technology status review," in *Electrical Machines Design Control and Diagnosis (WEMDCD), 2013 IEEE Workshop on*, 2013, pp. 117-129.

[13] S. Ziaeinejad, Y. Sangsefidi, H. P. Nabi, and A. Shoulaie, "Direct Torque Control of Two-Phase Induction and Synchronous Motors," *IEEE Trans. Power Electron.* , vol. 28, pp. 4041-4050, 2013.

[14] L.-H. Hoang, "Comparison of field-oriented control and direct torque control for induction motor drives," in *Industry Applications Conference, 1999. Thirty-Fourth IAS Annual Meeting. Conference Record of the 1999 IEEE*, 1999, pp. 1245-1252 vol.2.

[15] P. Zhang, B. Lu, and T. G. Habetler, "A remote and sensorless stator-winding-resistance-estimation method for thermal protection of soft-starter-connected induction machines," *IEEE Trans. Ind. Electron.,* vol. 55, pp. 3611-3618, Oct. 2008.

[16] F. M. Tesche and P. R. Barnes, "Transient response of a distribution circuit recloser and control unit to a high-altitude electromagnetic pulse (HEMP) and lightning," *IEEE Trans. Electromagn. Compat.,* vol. 32, pp. 113-124, 1990.

[17] J. F. Witte, S. R. Mendis, M. T. Bishop, and J. A. Kischefsky, "Computer-aided recloser applications for distribution systems," *Computer Applications in Power, IEEE,* vol. 5, pp. 27-32, 1992.

[18] S. Santoso and T. A. Short, "Identification of fuse and recloser operations in a radial distribution system," *IEEE Trans. Power Del.,* vol. 22, pp. 2370-2377, Oct. 2007.

[19] V. Arthi Sahaya Rones and K. P. Vittal, "Modeling of recloser and sectionalizer and their coordination using PSCAD," in *Circuits, Power and Computing Technologies (ICCPCT), 2013 International Conference on*, 2013, pp. 679-684.

[20] M. H. Kim, S. H. Lim, J. F. Moon, and J. C. Kim, "Method of Recloser-Fuse Coordination in a Power Distribution System With Superconducting Fault Current Limiter," *IEEE Trans. Appl. Supercond.,* vol. 20, pp. 1164-1167, 2010.

[21] M.-H. Kim, S.-H. Lim, and J.-C. Kim, "Improvement of Recloser-Fuse Operations and Coordination in a Power Distribution System With SFCL," *IEEE Trans. Appl. Supercond.,* vol. 21, pp. 2209-2212, 2011.

[22] E. B. Agamloh, S. Peele, and J. Grappe, "Induction-motor single-phasing performance under distribution-feeder recloser operations," *IEEE Trans. Ind. Appl.,* vol. 50, pp. 1568-1576, Mar.-Apr. 2014.

[23] A. F. Naiem, Y. Hegazy, A. Y. Abdelaziz, and M. A. Elsharkawy, "A classification technique for recloser-fuse coordination in distribution systems with distributed generation," *IEEE Trans. Power Del.,* vol. 27, pp. 176-185, Jan. 2012.

[24] A. Pregelj, M. Begovic, and A. Rohatgi, "Recloser allocation for improved reliability of DG-enhanced distribution networks," *IEEE Trans. Power Syst.,* vol. 21, pp. 1442-1449, Aug. 2006.

[25] A. V. Ryan, "A new heavy-duty three-phase oil circuit recloser," *Elect. Eng.,* vol. 72, pp. 307-307, Apr. 1953.

[26] E. J. Field and D. L. Leatherberry, "A Power Class Recloser for Higher Speed Clearing of Distribution Circuits [includes discussion]," *Trans. Amer. Inst. Elect. Eng. Power App. Syst., Part III,* vol. 74, 1955.

[27] J. M. Wallace, "An Improved Automatic Circuit Recloser," *Trans. Amer. Inst. Elect. Eng.,* vol. 66, pp. 255-263, 1947.

[28] E. J. Field and D. L. Leatherberry, "Power-class recloser for high-speed circuit clearing," *Elect. Eng.,* vol. 74, pp. 895-895, Oct. 1955.

[29] E. J. Field, "A 46-Kv Automatic Circuit Recloser," *Trans. Amer. Inst. Elect. Eng. Power App. Syst., Part III,* vol. 77, pp. 298-302, 1958.

[30] A. L. Streater, R. H. Miller, and J. C. Sofianek, "Heavy-duty vacuum recloser I," *Trans. Amer. Inst. Elect. Eng. Power App. Syst., Part III,* vol. 81, pp. 356-360, Oct. 1962.

[31] J. S. Stewart and A. C. Westrom, "Designing reliability into an SF6 recloser system for distribution automation," *IEEE Trans. Power Del.,* vol. 2, pp. 785-790, July 1987.

[32] D. A. Paice, "Motor thermal protection by continuous monitoring of winding resistance," *IEEE Trans. Ind. Electron. Control. Instrum.,* vol. IECI-27, pp. 137-141, Aug. 1980.

[33] S.-B. Lee and T. G. Habetler, "A remote and sensorless thermal-protection scheme for small line-connected AC machines," *IEEE Trans. Ind. Appl.,* vol. 39, pp. 1323-1332, Sept.-Oct. 2003.

[34] P. Zhang, Y. Du, B. Lu, and T. G. Habetler, "A DC Signal Injection-Based Thermal Protection Scheme for Soft-Starter-Connected Induction Motors," *IEEE Trans. Ind. Appl.,* vol. 45, pp. 1351-1358, Jul-Aug 2009.

[35] P. Zhang, Y. Du, J. Dai, T. G. Habetler, and B. Lu, "Impaired-Cooling-Condition Detection Using DC-Signal Injection for Soft-Starter-Connected Induction Motors," *IEEE Trans. Ind. Electron.,* vol. 56, pp. 4642-4650, 2009.

[36] C. A. Martins and A. S. Carvalho, "Technological trends in induction motor electrical drives," in *Power Tech Proceedings, 2001 IEEE Porto*, 2001, p. 7 pp. vol.2.

[37] J. A. Santisteban and R. M. Stephan, "Vector control methods for induction machines: an overview," *IEEE Trans. Educ.*, vol. 44, pp. 170-175, 2001.

[38] P. Zhang, B. Lu, and T. G. Habetler, "An active stator-temperature-estimation technique for thermal protection of inverter-fed induction motors with considerations of impaired cooling detection," *IEEE Trans. Ind. Appl.*, vol. 46, pp. 1873-1881, Sept.-Oct. 2010.

[39] J. Plotkin, M. Stiebler, and D. Schuster, "A novel method for online stator-resistance estimation of inverter-fed AC-machines without temperature sensors," in *Proc. 11th Int. Conf. Optim. Elect. Electron. Equipment*, 2008, pp. 155-161.

[40] F. Blaschke, "A new method for the structural decouplig of A.C. induction machines," in *Conf. Rec. IFAC*, Duesseldorf, Germany, 1971, pp. 1-15.

[41] F. Blaschke, "The principle of field orinetation as applied to the new transvector closed loop control for rotating machines," in *Siemens Review*, 1972, pp. 217-220.

[42] D. Casadei, F. Profumo, G. Serra, and A. Tani, "FOC and DTC: two viable schemes for induction motors torque control," *IEEE Trans. Power Electron.* , vol. 17, pp. 779-787, 2002.

[43] M. P. Kazmierkowski, "Control philosophies of PWM inverter-fed induction motors," in *Industrial Electronics, Control and Instrumentation, 1997. IECON 97. 23rd International Conference on*, 1997, pp. P16-P26 vol.1.

[44] M. P. Kazmierkowski, "Control strategies for PWM rectifier/inverter-fed induction motors," in *Industrial Electronics, 2000. ISIE 2000. Proceedings of the 2000 IEEE International Symposium on*, 2000, pp. TU15-TU23 vol.1.

[45] J. K. Seok, S. I. Moon, and S. K. Sul, "Induction-machine-parameter identification using PWM inverter at standstill," *IEEE Trans. Energy Convers.*, vol. 12, pp. 127-132, June 1997.

[46] L. A. de Souza Ribeiro, C. B. Jacobina, A. M. N. Lima, and A. C. Oliveira, "Parameter sensitivity of MRAC models employed in IFO-controlled AC motor drives," *IEEE Trans. Ind. Electron.*, vol. 44, pp. 536-545, Aug. 1997.

[47] L. A. D. Ribeiro, C. B. Jacobina, and A. M. N. Lima, "Linear parameter estimation for induction machines considering the operating conditions," *IEEE Trans. Power Electron.* , vol. 14, pp. 62-73, Jan 1999.

[48] S. Cheng, Y. Du, J. A. Restrepo, P. Zhang, and T. G. Habetler, "A non-intrusive thermal-monitoring method for induction motors fed by closed-loop inverter drives," *IEEE Trans. Power Electron.,* vol. 27, pp. 4122-4131, Sept. 2012.

[49] S. Cheng, Y. Du, J. A. Restrepo, P. Zhang, and T. G. Habetler, "A nonintrusive thermal monitoring method for closed-loop drive-fed induction machines," in *Energy Conversion Congress and Exposition (ECCE), 2011 IEEE*, 2011, pp. 714-721.

[50] Z. Gao, T. G. Habetler, and R. G. Harley, "A Complex Space Vector Approach to Rotor Temperature Estimation for Line-Connected Induction Machines With Impaired Cooling," *IEEE Trans. Ind. Electron.,* vol. 56, pp. 239-247, 2009.

[51] S.-B. Lee and T. G. Habetler, "An online stator winding resistance estimation technique for temperature monitoring of line-connected induction machines," *IEEE Trans. Ind. Appl.,* vol. 39, pp. 685-694, 2003.

[52] S.-B. Lee, T. G. Habetler, R. G. Harley, and D. J. Gritter, "An evaluation of model-based stator resistance estimation for induction motor stator winding temperature monitoring," *IEEE Trans. Energy Convers.,* vol. 17, pp. 7-15, 2002.

[53] S.-B. Lee, T. G. Habetler, R. G. Harley, and D. J. Gritter, "A stator and rotor resistance estimation technique for conductor temperature monitoring," *IAS 2000 - Conference Record of the 2000 IEEE Industry Applications Conference, Vols 1-5*, pp. 381-387, 2000.

[54] I. Takahashi and T. Noguchi, "A new quick-response and high-efficiency control strategy of an induction motor," *IEEE Trans. Ind. Appl.,* vol. IA-22, pp. 820-827, Sept. 1986.

[55] A. H. Bonnett and G. C. Soukup, "Cause and analysis of stator and rotor failures in three-phase squirrel-cage induction motors," *IEEE Trans. Ind. Appl.,* vol. 28, pp. 921-937, 1992.

[56] "Report of Large Motor Reliability Survey of Industrial and Commercial Installations, Part I," *IEEE Trans. Ind. Appl.,* vol. IA-21, pp. 853-864, 1985.

[57] S. F. Farag and M. K. Jhaveri, "Intelligent microprocessor-based devices provide advanced motor protection, flexible control, and communication in paper mills," *IEEE Trans. Ind. Appl.,* vol. 33, pp. 840-847, 1997.

[58] F. Briz, M. W. Degner, J. M. Guerrero, and A. B. Diez, "Temperature Estimation in Inverter-Fed Machines Using High-Frequency Carrier Signal Injection," *IEEE Trans. Ind. Appl.,* vol. 44, pp. 799-808, 2008.

[59] P. H. Mellor, D. Roberts, and D. R. Turner, "Lumped Parameter Thermal-Model for Electrical Machines of Tefc Design," *IEE Proc.—B Electr. Power Appl.,* vol. 138, pp. 205-218, Sep. 1991.

[60] A. Bousbaine, M. Mccormick, and W. F. Low, "In-Situ Determination of Thermal Coefficients for Electrical Machines," *IEEE Trans. Energy Convers.*, vol. 10, pp. 385-391, Sep 1995.

[61] J. F. Moreno, F. P. Hidalgo, and M. D. Martinez, "Realisation of tests to determine the parameters of the thermal model of an induction machine," *IEE Proc.—Electr. Power Appl.*, vol. 148, pp. 393-397, Sep. 2001.

[62] A. Boglietti, A. Cavagnino, M. Lazzari, and M. Pastorelli, "A simplified thermal model for variable speed self cooled industrial induction motor," *in Proc. Conf. Rec. IEEE Ind. Appl. Conf.*, vol. 1-4, pp. 723-730, 2002.

[63] C. Kral, A. Haumer, and S. B. Lee, "A Practical Thermal Model for the Estimation of Permanent Magnet and Stator Winding Temperatures," *IEEE Trans. Power Electron.* , vol. 29, pp. 455-464, 2014.

[64] "IEEE Standard Test Procedure for Polyphase Induction Motors and Generators," *IEEE Std 112-2004 (Revision of IEEE Std 112-1996)*, pp. 0_1-79, 2004.

[65] L. He, J. R. Mayor, R. G. Harley, H. Liles, G. Zhang, and Y. Deng, "Multi-physics modeling of the dynamic response of a circuit breaker recloser system," in *Electric Machines & Drives Conference (IEMDC), 2013 IEEE International*, 2013, pp. 1001-1008.

[66] L. He, J. R. Mayor, R. G. Harley, H. Liles, G. Zhang, and Y. Deng, "Multiphysics Modeling of the Dynamic Response of a Vacuum Automatic Circuit Recloser System," *IEEE Trans. Ind. Appl.*, vol. 50, pp. 3697-3707, 2014.

[67] D. C. Hanselman, *Brushless Permanent-Magnet Motor Design*, 2nd ed. Lebanon, OH, USA: Magna Physics, 2006.

[68] D. J. McGill and M. W. King, *An Introduction to Dynamics*, 4th ed. Bloomington, IN, USA: Tichenor, 2003.

[69] L. He, S. Cheng, R. G. Harley, and T. G. Habetler, "A torque-injection-based approach for thermal monitoring of induction machines with direct torque control," in *Electric Machines & Drives Conference (IEMDC), 2013 IEEE International*, 2013, pp. 93-99.

[70] L. He, S. Cheng, Y. Du, R. G. Harley, and T. G. Habetler, "A DC-flux-injection approach for thermal monitoring of induction machines with direct torque control," in *Energy Conversion Congress and Exposition (ECCE), 2013 IEEE*, 2013, pp. 2115-2122.

[71] L. He, S. Cheng, Y. Du, R. G. Harley, and T. G. Habetler, "Stator Temperature Estimation of Direct-Torque-Controlled Induction Machines via Active Flux or Torque Injection," *IEEE Trans. Power Electron.*, vol. 30, pp. 888-899, 2015.

[72] L. He, J. Restrepo, S. Cheng, R. G. Harley, and T. G. Habetler, "An Improved DC-Signal-Injection Method with Active Torque-Ripple Mitigation for Thermal Monitoring of Field-Oriented-Controlled Induction Motors," in *Energy Conversion Congress and Exposition (ECCE), 2015 IEEE*, 2015.

[73] P. Zhang, Y. Du, T. G. Habetler, and B. Lu, "Magnetic Effects of DC Signal Injection on Induction Motors for Thermal Evaluation of Stator Windings," *IEEE Trans. Ind. Electron.*, vol. 58, pp. 1479-1489, 2011.

[74] K. Kubota and K. Matsuse, "Speed sensorless field-oriented control of induction motor with rotor resistance adaptation," *IEEE Trans. Ind. Appl.*, vol. 30, pp. 1219-1224, 1994.

[75] S. Wade, M. W. Dunnigan, and B. W. Williams, "Improving the accuracy of the rotor resistance estimate for vector-controlled induction machines," *Electric Power Applications, IEE Proceedings* -, vol. 144, pp. 285-294, 1997.

[76] Y. Wu and H. Gao, "Induction-motor stator and rotor winding temperature estimation using signal injection method," *IEEE Trans. Ind. Appl.*, vol. 42, pp. 1038-1044, 2006.

[77] K.-R. Cho and J.-K. Seok, "Induction Motor Rotor Temperature Estimation Based on a High-Frequency Model of a Rotor Bar," *IEEE Trans. Ind. Appl.*, vol. 45, pp. 1267-1275, 2009.

[78] Y.-S. Kwon, J.-H. Lee, S.-H. Moon, B.-K. Kwon, C.-H. Choi, and J.-K. Seok, "Standstill Parameter Identification of Vector-Controlled Induction Motors Using the Frequency Characteristics of Rotor Bars," *IEEE Trans. Ind. Appl.*, vol. 45, pp. 1610-1618, 2009.

[79] M. O. Sonnaillon, G. Bisheimer, C. De Angelo, and G. O. Garcia, "Online Sensorless Induction Motor Temperature Monitoring," *IEEE Trans. Energy Convers.* , vol. 25, pp. 273-280, 2010.

[80] K. Wang, B. Chen, G. Shen, W. Yao, K. Lee, and Z. Lu, "Online Updating of Rotor Time Constant Based on Combined Voltage and Current Mode Flux Observer for Speed-Sensorless AC Drives," *IEEE Trans. Ind. Electron.*, vol. 61, pp. 4583-4593, 2014.

[81] K. Akatsu and A. Kawamura, "Online rotor resistance estimation using the transient state under the speed sensorless control of induction motor," *IEEE Trans. Power Electron.* , vol. 15, pp. 553-560, May 2000.

[82] G. Zhi, T. G. Habetler, R. G. Harley, and R. S. Colby, "A Sensorless Adaptive Stator Winding Temperature Estimator for Mains-Fed Induction Machines With Continuous-Operation Periodic Duty Cycles," *IEEE Trans. Ind. Appl.*, vol. 44, pp. 1533-1542, 2008.

[83] Z. Gao, T. G. Habetler, R. G. Harley, and R. S. Colby, "A Sensorless Rotor Temperature Estimator for Induction Machines Based on a Current Harmonic Spectral Estimation Scheme," *IEEE Trans. Ind. Electron.*, vol. 55, pp. 407-416, 2008.

[84] C. B. Jacobina, J. E. C. Filho, and A. N. Lima, "On-line estimation of the stator resistance of induction machines based on zero-sequence model," *IEEE Trans. Power Electron.* , vol. 15, pp. 346-353, 2000.

VITA

Lijun He was born in the city of Xi'an, China, in 1989, a most glorious and prosperous place which represents the highest level of ancient Chinese civilization.

In the year of 2007, she joined Tsinghua University, and spent four years studying electrical engineering. In her colleague years, she became attached to electric machine and power electronics. She worked with Prof. Yongdong Li on wind generator system control, and graduated from Tsinghua University in the summer of 2011.

Lijun enrolled in ECE power group, Georgia Institute of Technology in the fall of 2011, and started to pursue a PhD degree under the supervision of Prof. Ronald G. Harley and Prof. Thomas G. Habetler. At Georgia Tech, Lijun worked on a good number of different projects on control and condition monitoring of electric machines, as well as the physical modeling for electric protection apparatuses.

During her years studying at Georgia Tech, Lijun worked as a research intern at Research Innovation Center of Ford Motor Company, Generator Design Group of Siemens Energy, Corporate Research Technology of Eaton Corporation, and also the Global Research Center of General Electric, respectively, in the area of electric machine design, monitoring and diagnostics, as well as enhanced fault detection and protection in power distribution system.

Lijun He is an IEEE student member since 2012. She is also a student member of the IEEE Industry Applications, Power Electronics, and Power and Energy Societies. She is actively involved in IEEE actives, and served as the chair of PES Student branch chapter at Georgia Tech in the year of 2013 to 2014.